ABSTRACT

COUSINS, WILLIAM BRYAN. Boundary Conditions and Uncertainty Quantification for Hemodynamics. (Under the direction of Pierre Gremaud.)

We address outflow boundary conditions for blood flow modeling. In particular, we consider a variety of fundamental issues in the structured tree boundary condition. We provide a theoretical analysis of the numerical implementation of the structured tree, showing that it is sensible but must be performed with great care. We also perform analytical and numerical studies on the sensitivity of model output on the structured tree's defining geometrical parameters. The most important component of this dissertation is the derivation of the new, generalized structured tree boundary condition. Unlike the original structured tree condition, the generalized structured tree does not contain a temporal periodicity assumption and is thus applicable to a much broader class of blood flow simulations. We describe a numerical implementation of this new boundary condition and show that the original structured tree is in fact a rough approximation of the new, generalized condition.

We also investigate parameter selection for outflow boundary conditions, and attempt to determine a set of structured tree parameters that gives reasonable simulation results without requiring any calibration. We are successful in doing so for a simulation of the systemic arterial tree, but the same parameter set yields physiologically unreasonable results in simulations of the Circle of Willis. Finally, we investigate the extension of recently introduced PDF methods to smooth solutions of systems of hyperbolic balance laws subject to uncertain inputs. These methods, currently available only for scalar equations, would provide a powerful tool for quantifying uncertainty in predictions of blood flow and other phenomena governed by first order hyperbolic systems.

Boundary Conditions and Uncertainty Quantification for Hemodynamics

by
William Bryan Cousins

A dissertation submitted to the Graduate Faculty of
North Carolina State University
in partial fulfillment of the
requirements for the Degree of
Doctor of Philosophy

Applied Mathematics

Raleigh, North Carolina

2013

APPROVED BY:

Tim Kelley	Mette Olufsen
Ralph Smith	Brooke Steele

Pierre Gremaud
Chair of Advisory Committee

DEDICATION

To my parents. I would have accomplished nothing without their undying love and support.

BIOGRAPHY

William Bryan Cousins was born in Columbia, South Carolina. After graduating from Irmo High School in 2005, he attended Pepperdine University in Malibu, California. While at Pepperdine, he was appointed Secretary of Defense of the University's math club and received international recognition for discovering various new ways to injure oneself while riding scooters down large hills. William graduated from Pepperdine with a Bachelor of Science degree in Mathematics in May 2009.

After graduating from Pepperdine, William began graduate study in Applied Mathematics at North Carolina State University. In December of 2011, he earned a Master of Science degree in Applied Mathematics. He will receive a Doctorate of Philosophy degree in Applied Mathematics from North Carolina State University in 2013.

ACKNOWLEDGEMENTS

This dissertation would not have been completed without Pierre Gremaud's spectacular service as my advisor. He has been and continues to be a spectacular source of advice, encouragement, and good ideas.

I owe a debt to Daniel Tartakovsky. If he had not told Pierre and I to take a Laplace transform, the generalized structured tree condition would likely not exist.

I am thankful to Mette Olufsen and Vera Novak for collecting and sharing data that I use extensively in the numerical simulations in this work.

I would also like to thank my committee members Tim Kelley, Ralph Smith, and Brooke Steele, whose insights improved the quality of this work.

Finally, I am grateful to the Math Department at North Carolina State and the National Science Foundation for financial support.

TABLE OF CONTENTS

LIST OF TABLES . . . . **vii**

LIST OF FIGURES . . . . **ix**

Chapter 1 Introduction **1**
  1.1 The Human Cardiovascular System 2
  1.2 Modeling the Cardiovascular System 3
    1.2.1 1D Models 5

Chapter 2 Boundary Conditions for Hemodynamics **10**

Chapter 3 Implementation of The Original Structured Tree **16**
  3.1 Derivation of Original Structured Tree 17
    3.1.1 Geometry of the Structured Tree 17
    3.1.2 Hemodynamics in the Tree 18
    3.1.3 Alternative Formulation 20
  3.2 Structured Tree Implementation 23
    3.2.1 Enforcement of Structured Tree Condition 25
    3.2.2 Convergence of Solution to Periodic Regime 32
  3.3 Sensitivity to Minimum Radius 35

Chapter 4 The Generalized Structured Tree Boundary Condition **40**
  4.1 Derivation 41
    4.1.1 Single vessel equations 41
    4.1.2 Extension to structured vascular trees 42
    4.1.3 Algorithm to compute the impedance 42
  4.2 Numerical Implementation 43
    4.2.1 Convolution quadrature 44
    4.2.2 Impedance Implementation Algorithm 46
  4.3 Singularities of the Laplace Transform of Impedance 47
  4.4 Connection to Periodic Version of Structured Tree 54
    4.4.1 Comparison for Periodic Flows 54
    4.4.2 Comparison for Non-Periodic Flows 55
  4.5 The Periodic Condition is an Approximation of the General Condition 59
    4.5.1 Numerical Issues with the Periodic Condition 63
  4.6 Conclusions 65

Chapter 5 Parameter Selection for the Structured Tree **67**
  5.1 A Closer Look at Structured Tree Parameters 68
    5.1.1 Branching Parameters 68
    5.1.2 Vessel Length-to-Radius Ratio 70
    5.1.3 Radius Dependent Viscosity 71
    5.1.4 Terminal Impedance 73

5.1.5 Minimum Radius . . . 74
5.2 Simulation Results . . . 75
5.3 Systematic Boundary Condition Comparison . . . 78
5.4 Conclusion . . . 85

Chapter 6 Uncertainty Quantification . . . 90
6.1 PDF Equations . . . 91
6.1.1 Scalar Balance Laws . . . 92
6.1.2 Systems of Hyperbolic Balance Laws . . . 94
6.1.3 Hyperbolic Conservation Laws . . . 103
6.2 Conclusions . . . 108

Chapter 7 Conclusions . . . 109

REFERENCES . . . 111

Appendix . . . 119
Appendix A Simulation Details . . . 120
A.0.1 Spatial Discretization . . . 120
A.0.2 Time Discretization . . . 122
A.0.3 Numerical Implementation of Boundary Conditions . . . 123
A.0.4 Network Descriptions . . . 127
A.0.5 Parameter Values . . . 129
A.0.6 Convergence Study . . . 129

LIST OF TABLES

Table 3.1 Parameters used to generate Figure 3.2. 23
Table 3.2 Spectral radii of $R^{-1}S$ in (3.28) for the right and left Posterior Cerebral Arteries (PCA), Middle Cerebral Arteries (MCA), and Anterior Cerebral Arteries (ACA). 35
Table 3.3 Published values for the scaling parameter ξ. 38

Table 4.1 Spectral radii of $R^{-1}S$ in (4.22) for the periodic and general structured tree conditions. See Section (3.2.2) for a detailed description of the contents of R and S. 65

Table 5.1 Tiered branching parameter structure used by Steele et. al. in [81] 69
Table 5.2 Measured and theoretical values of the branching parameter ξ. A “sample” refers to a triplet of values of r_{pa}, r_{d_1}, r_{d_2} measured at a single junction. 69
Table 5.3 Asymmetry ratio data from VanBavel and Spaan [92]. A “sample” refers to a pair of values of (r_{d_1}, r_{d_2}) from a single junction. 70
Table 5.4 Tiered λ structure proposed here combined with the tiered branching parameter structure used in [81]. 71
Table 5.5 Data from Nordsletten et. al. [61]. We have computed and appended the leftmost column of λ values by dividing the length and radius values originally published in [61]. Computed values of λ are rounded to the nearest integer. 72
Table 5.6 Minimum radius values used in a variety of implementations of the structured tree condition. A * by a minimum radius value indicates that this study used a tiered branching structure, rather than a single set of branching parameters. 75
Table 5.7 Ranges for randomly generated structured tree parameter sets 80
Table 5.8 Numerical values of difference between numerical simulations of the Circle of Willis using the structured tree and Windkessel boundary conditions. The largest, median, and smallest difference rows correspond to the top, middle, and bottom plots in Figure 5.4. 81
Table 5.9 Numerical values of difference between numerical simulations of the Circle of Willis using the structured tree and pure resistor boundary conditions. The largest, median, and smallest difference rows correspond to the top, middle, and bottom plots in Figure 5.5. 83

Table A.1 Names and measured length/radii data (in cm) for the Circle of Willis (Figure A.1). Data are from [26]. BA–Basilar Artery, PCA–Posterior Cerebral Artery, PCoA–Posterior Communicating Artery, ICA–Internal Carotid Artery, MCA–Middle Cerebral Artery, ACA–Anterior Cerebral Artery, AcoA–Anterior Communicating Artery. An * accompanying a data value indicates that this value was estimated rather than directly measured. 128

Table A.2 Names and length/radii data for the systemic arterial tree network used in the simulations in Chapter 5. Data are from Olufsen [62, 64]. 131
Table A.3 Parameter values used for simulations in this dissertation 132
Table A.4 Convergence of numerical solutions to the Circle of Willis with respect to the number of spatial points per vessel. 132
Table A.5 Convergence of numerical solutions to the Circle of Willis with respect to time step size using the Windkessel boundary condition. 133
Table A.6 Convergence of numerical solutions to the Circle of Willis with respect to time step size using the structured tree boundary condition. 134

LIST OF FIGURES

Figure 1.1 Schematic of the Circle of Willis. The symbols at various vessel ends represent different boundary conditions imposed at those points (see Chapter 2) 4
Figure 1.2 Diagram showing the meaning of the x and r coordinates 6

Figure 2.1 Inflow velocity data used as a boundary condition in simulations of the Circle of Willis. The blue curve corresponds to raw, measured velocity data, and the red, dashed curve is the smoothed data. 12

Figure 3.1 Visualization of Olufsen's algorithm for computing the impedance at the root of the structured tree. 21
Figure 3.2 Modulus and phase of the root impedance generated by the structured tree algorithm using impedance relations (3.6) (blue, solid curve) and (3.16) (red, dashed curve). All parameter values (see Table 3.1) are from [64]. 23
Figure 3.3 Left: Pressure curves obtained from a numerical simulation of the Circle of Willis using a composite right hand rule (blue) and composite Simpson's rule (red) to discretize the convolution integral in (3.21). Right: Results of a grid refinement study, indicating convergence of both methods as $\Delta t \to 0$. u^* indicates the limiting solution as $\Delta t \to 0$. 31
Figure 3.4 Convergence of $\Delta_k \vec{u}$ to 0, indicating convergence of the numerical solution to a periodic regime. 33
Figure 3.5 Pressure and flowrate curves using $r_{min} = 20, 40, 60, 80$, and $100\mu m$. The red (top) curves correspond to $r_{min} = 20\mu m$ and the blue (bottom) curves correspond to $r_{min} = 100\mu m$. 39

Figure 4.1 Comparison of the impedance weights generated by the periodic (blue, solid curve) and general (red, dashed curve) structured tree boundary conditions. 56
Figure 4.2 Inflow velocity curves for the left internal carotid for each of the three numerical experiments. 56
Figure 4.3 Top row: Left: solutions for a simulation using raw inflow velocity data with the periodic (blue, solid curve) and general (red, dashed curve) structured tree boundary conditions (experiment 1). The solution is displayed at the worst point in the network, see text. Right: logarithm of the absolute value of the difference between the two methods at that point. Middle row: idem for periodic inflow velocity data (experiment 2). Bottom row: idem for periodic inflow velocity data that experiences a rapid decrease at $t = 2$ with the periodic (experiment 3). 58
Figure 4.4 Values of Δ_k for the periodic (blue, solid line) and general (red, dashed line) structured tree conditions, showing that the general condition yields a solution converging to periodicity at a much faster rate than the original, periodic condition. 64

Figure 5.1 Computed (blue, solid curve) and measured (black, dot-dashed curve) flowrate values in various locations in the systemic arterial tree. The computed values were obtained using the structured tree boundary condition with parameters from Section 5.1. 76
Figure 5.2 Computed pressure values at various locations in the systemic arterial tree using the structured tree condition with parameters from Section 5.1. 77
Figure 5.3 Computed pressure and flowrate values in the Circle of Willis using the structured tree boundary condition with parameters from Section 5.1. . 79
Figure 5.4 Comparison between the structured tree (blue, solid curve) and Windkessel (red, dashed curve) for simulations of the Circle of Willis with randomly generated tree parameters. The top plot displays the largest difference between the two, the middle plot displays the median difference, and the bottom plot is the smallest difference. 82
Figure 5.5 Comparison between the structured tree (blue, solid curve) and pure resistor (red, dashed curve) for simulations of the Circle of Willis with randomly generated tree parameters. The top plot displays the largest difference between the two, the middle plot displays the median difference, and the bottom plot is the smallest difference. 84
Figure 5.6 Fits of the Windkessel parameters to the structured tree using the tiered structure described in Section 5.1. The blue, solid curve represents the computed Windkessel parameters that match the structured tree impedance most closely, and the red, dashed curve is a power law fit to these fitted values. 86
Figure 5.7 Computed structured tree (blue, solid curve), Windkessel with fitted parameters (red, dashed curve), and measured (black, dot-dashed curve) flowrate values in various locations in the systemic arterial tree. The computed values were obtained using the structured tree boundary condition with parameters from Section 5.1. 87
Figure 5.8 Computed pressure values at various locations in the systemic arterial tree using the structured tree condition using the structured tree (blue, solid curve) and the associated Windkessel fit (red-dashed curve). 88
Figure 5.9 Computed pressure and flowrate values in the Circle of Willis using the structured tree (blue, solid curve) with parameters from Section 5.1 and the associated Windkessel fits (red, dashed curve). 89

Figure 6.1 The numerical solution of (6.6) and the true PDF for (6.9) with additive initial noise at $x = 2$ for times $t = 0, 0.5$, and 1. 97
Figure 6.2 The L_2 (red, dashed line) and L_∞ (blue, solid line) norms (in V and W) of the error in the approximation of the PDF for the wave equation first order system with additive initial noise at $x = 2$ for various times. . . . 98
Figure 6.3 The numerical solution of (6.6) and the true PDF for (6.9) with multiplicative initial noise at $x = 2$ for $t = 0, 0.5, 1$. 100
Figure 6.4 The L_2 (red, dashed line) and L_∞ (blue, solid line) norms (in V and W) of the error in the approximation of the PDF for the wave equation first order system with multiplicative initial noise at $x = 2$ for various times. 101

Figure 6.5 Time evolution of the CDF of the solution (6.20), (6.21) at $t = 0, 0.2, 0.4, 0.6$, and 0.8 as computed from (6.18), left, and Monte Carlo simulation with 1000 realizations of ξ, right. Solutions for Monte Carlo are obtained by solving (6.22) 105
Figure 6.6 Time evolution of the CDF, right, and the solution to (6.18), left, for Burgers' equation with a random shock at $t = 0, 0.2, ..., 1.6$ 106

Figure A.1 Schematic of the Circle of Willis. 129
Figure A.2 Schematic of the systemic arterial tree network used in Chapter 5. The trees attached to each outlet vessel symbolizes the use of the structured tree to model the downstream domain. 130
Figure A.3 Convergence of numerical simulations of the Circle of Willis with respect to the number of spatial points per vessel for a fixed time step size of $\Delta t = 0.001$. The blue curve was generated for the Windkessel boundary condition, and the red curve uses the periodic structured tree. In the vertical axis label, u^* denotes a numerical solution computed with 33 spatial points per vessel ($N = 32$). 133
Figure A.4 Convergence of numerical simulations of the Circle of Willis with respect to Δt for a fixed number of spatial points per vessel ($N = 8$). The blue curve was generated using the Windkessel boundary condition, and the red curve uses the periodic structured tree. In the vertical axis label, u^* denotes a numerical solution computed with a value of Δt five times smaller than the smallest value of Δt listed in Table A.5. 134

Chapter 1

Introduction

The massive size and complexity of the cardiovascular system prevent the direct application of high fidelity mathematical models to the whole system. A common approach is to choose a small subset of arteries to model in detail, while accounting for the remainder of the vasculature through boundary conditions. In this dissertation, I consider solely arterial hemodynamics, which means that the inflow vessels, i.e., vessels on the boundary of the computational domain where blood flows into the network, tend to be few in number and of significant size. However, the outflow vessels, i.e., vessels on the boundary of the computational domain where blood flows out of the network, are substantially more numerous. Thus, while it may be reasonable to impose measured data for the inflow vessels, it is typically impractical to obtain measured data at the many outflow vessels. For this reason, outflow vessels require a boundary condition that incorporates the effects of the downstream vasculature, rather than impose specific values on the solutions themselves.

One such boundary condition is the structured tree, developed by Olufsen in [62, 63, 64], which treats the downstream vasculature as a self-similar branching tree and solves a linearized blood flow model in this tree to provide a boundary condition. In Chapter 3, I review the derivation of the structured tree and investigate a variety of issues related to its implementation. For instance, its use of the convolution theorem raises a number of theoretical and practical questions. I show that, if implemented with great care, the original numerical implementation proposed by Olufsen in [62] is valid. In this chapter I also perform analytical and numerical studies of the structured tree's dependence on its defining geometrical parameters. I show that model output depends critically on the chosen minimum vessel radius in the tree.

A substantial drawback of the structured tree condition is that it requires an assumption of temporal periodicity. This assumption limits the applicability of the structured tree, as a number of phenomena such as cardiac arrhythmia and exercise involve flows that are highly non-periodic. In Chapter 4, I derive a new structured tree condition that does not contain this periodicity assumption and is thus applicable to *all* flows. I derive this condition by replacing the Fourier series approach used by Olufsen with a Laplace transform-based approach. I then describe a numerical implementation of this condition that does not involve a perilous numerical inverse Laplace transform. Furthermore, I show how the original, periodic structured tree is a rough approximation of the newly derived generalized structured tree condition.

Parameter selection for the structured tree and other outflow boundary conditions is challenging. The structured tree provides a potential method for overcoming this issue since its defining parameters are physiological quantities that may be measured. Despite this fact, I discuss in Chapter 5 how a number of authors have needed to calibrate the structured tree parameters to obtain acceptable simulation results, often obtaining physiologically unreasonable parameter values in the process. I then investigate the physiologically correct values of various parameters in the tree with the goal of obtaining reasonable simulation results *without* performing any calibration. I obtain reasonable agreement with data for a simulation of the systemic arterial tree (with no calibration), but I obtain physiologically unreasonable results in a simulation of the Circle of Willis. It may be possible to fix this issue by considering organ specific properties of arterial trees–I provide some discussion of this idea in Chapter 7.

Blood flow model predictions require one to specify parameters and boundary conditions that are not known with exact certainty. A relatively new technique for quantifying the associated uncertainty in simulation results is to derive a closed partial differential equation for the evolution of the probability density function of the uncertain model solution. This approach is currently limited to scalar first order equations; in Chapter 6 I investigate a possible extension to hyperbolic systems of first order equations. This extension would provide a powerful new uncertainty quantification tool for blood flow and other phenomena modeled by first order hyperbolic systems.

To begin, I briefly overview the human cardiovascular system. I then discuss common blood flow modeling methodology as well as common techniques to develop 1D models of arteries. These models, which can provide accurate predictions of flow and pressure in the human body [73, 64, 9], are the fundamental tool used to model blood flow in this work.

1.1 The Human Cardiovascular System

The human cardiovascular system consists of 4 primary components:

1. Blood, consisting primarily of a suspension of red blood cells in plasma
2. The heart, which consists of four chambers: the right atrium, the right ventricle, the left atrium, and the left ventricle.
3. The systemic circulation, consisting of the systemic arteries, capillaries, and veins
4. The pulmonary circulation, consisting of the pulmonary arteries, capillaries, and veins

The left ventricle of the heart contracts periodically roughly once per second. When this occurs, oxygenated blood is pumped into the systemic arteries. These arteries form a branching network whose vessels get perpetually smaller as distance from the heart increases. These arteries lead to capillaries, which are small vessels with radii comparable to the diameter of a single red blood cell (roughly 8μm). At this level, oxygen and other nutrients diffuse through the capillary wall to provide essential nutrients to tissues.

After passing through the capillaries, blood is returned to the right atrium of the heart through the veins. Blood is then moved to the right ventricle of the heart, which pumps the blood through the pulmonary circulation. The pulmonary circulation is similar to the systemic circulation in that it also contains arteries, capillaries, and veins, but the purpose of these two circulations is quite different. As blood flows through the pulmonary circulation oxygen is transferred *into* the blood, after which blood returns to the heart, is pumped out of the left ventricle, and delivers this oxygen to tissues, thus completing the cycle.

1.2 Modeling the Cardiovascular System

There are a variety of ways that the cardiovascular system can fail to accomplish its important functions, and mathematical modeling of this system provides a pathway to better understand or prevent these failures. For example, Marsden et. al. [52] modeled blood flow in patients with a type of congenital heart defect who have undergone the Fontan surgical procedure, which diverts blood flow from the veins around the right atrium and directly to the pulmonary circulation. This procedure is often required to prevent death, but longer term survival rates of patients who undergo this procedure are only 60% after 10 years [52] with significant risks of irregular heartbeat and diminished exercise capacity. Since it is difficult to obtain in vivo measurements of these patients while exercising, Marsden et. al. use mathematical modeling to analyze the efficiency of multiple variations of the Fontan procedure during exercise.

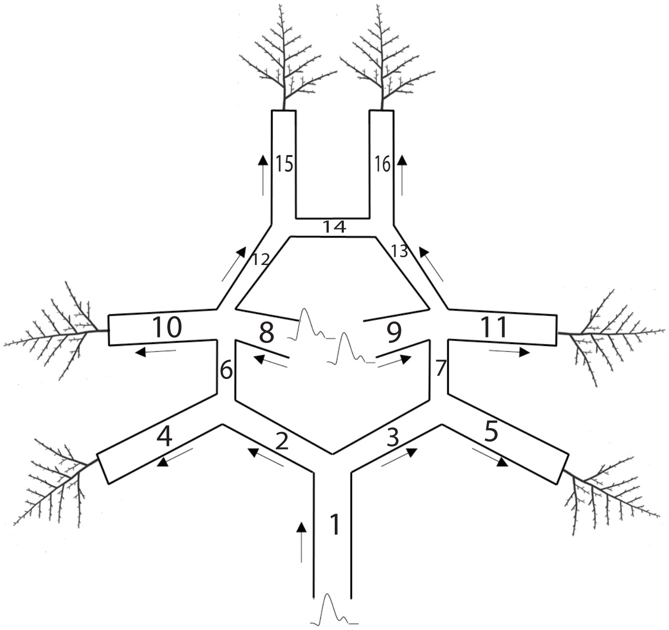

Figure 1.1: Schematic of the Circle of Willis. The symbols at various vessel ends represent different boundary conditions imposed at those points (see Chapter 2)

Stroke, a situation where blood is not adequately delivered to brain tissues, is a leading cause of death and disability [15]. Blood is delivered to the brain primarily through the Circle of Willis, which is a ring-like structure of arteries located at the base of the brain (see Figure 1.1). This network contains redundancies, so unsurprisingly individual Circle of Willis structures vary considerably throughout the population, with 50% of healthy brains containing at least one underdeveloped or missing artery [6]. Using models of blood flow, Alastruey et. al. [3] and DeVault [27] quantified to what degree these anatomical variations left one vulnerable to a sudden vessel occlusion. This idea could be used to estimate an individual's stroke risk. Understanding the effects of these anatomical variations in different settings is also relevant for vascular surgical planning [40].

In the larger arteries, the diameter of red blood cells (roughly 8μm) is small enough compared to the radius of the vessel to adequately treat blood as a fluid whose motion is determined by the Navier-Stokes equations [18]. A number of authors have successfully used such 3D models to simulate blood flow [52, 56, 35, 65, 95, 55]. However, in this work our focus is on simpler 1D models, which can provide accurate predictions of blood flow at a fraction of the cost of 3D models.

1.2.1 1D Models

Although the problem of blood flow in arteries is technically a three-dimensional phenomena, the cylindrical shape of many vessels suggest that a simpler 1D model may be sufficient. The authors of [65, 56, 35] performed 3D simulations, averaged the resulting solutions over vessel cross sections, and compared the results to 1D model simulations. They found that predictions generated by the 1D models were similar to the 3D models, suggesting that 1D models may be adequate for situations where one is only interested in one dimensional quantities, such as the blood pressure or flow at a particular spatial point averaged over the cross sectional area of a vessel.

In order to derive 1D equations, one must make approximations in order to close nonlinear terms that are not amenable to averaging over cross sections. There are a variety of choices as to how to go about doing so, with different choices leading to different 1D models. We now provide an example of such an approach by deriving the 1D model used in this dissertation. The following derivation is similar to approaches taken by other authors [63, 64, 81, 73], and corresponds exactly to the 1D system obtained in [26].

We use a cylindrical polar coordinate system to describe the interior of a blood vessel, with each point inside the vessel identified by a coordinate (x, r, θ), where $0 \leq x \leq L, 0 \leq r \leq R(x, \theta, t)$, and $0 \leq \theta < 2\pi$. The x coordinate determines the position along the axis of the vessel, with L being the length of the vessel. r is the radial coordinate and denotes a particular point's distance from the axis of the vessel, and $R(x, \theta, t)$ denotes the radius of the vessel at a particular point. Figure 1.2 contains a diagram showing the meaning of the x and r coordinates.

Let $u_x(x, r, \theta, t), u_r(x, r, \theta, t)$, and $u_\theta(x, r, \theta, t)$ denote the respective x, r, and θ components of blood velocity, $p(x, r, \theta, t)$ the blood pressure, and let μ and ρ denote the viscosity and density of blood, respectively. The following assumptions are standard in the field of 1D blood flow models [53, 2, 26, 30, 32, 79, 73, 91]:

1. The density of blood, ρ, is constant.
2. Gravitational effects are negligible.
3. Blood velocity and pressure are axisymmetric, that is, there is no dependence on θ
4. There is no "swirl," i.e. $u_\theta = 0$
5. The pressure is constant on vessel cross sections, $p(x, r, \theta, t) = P(x, t)$.

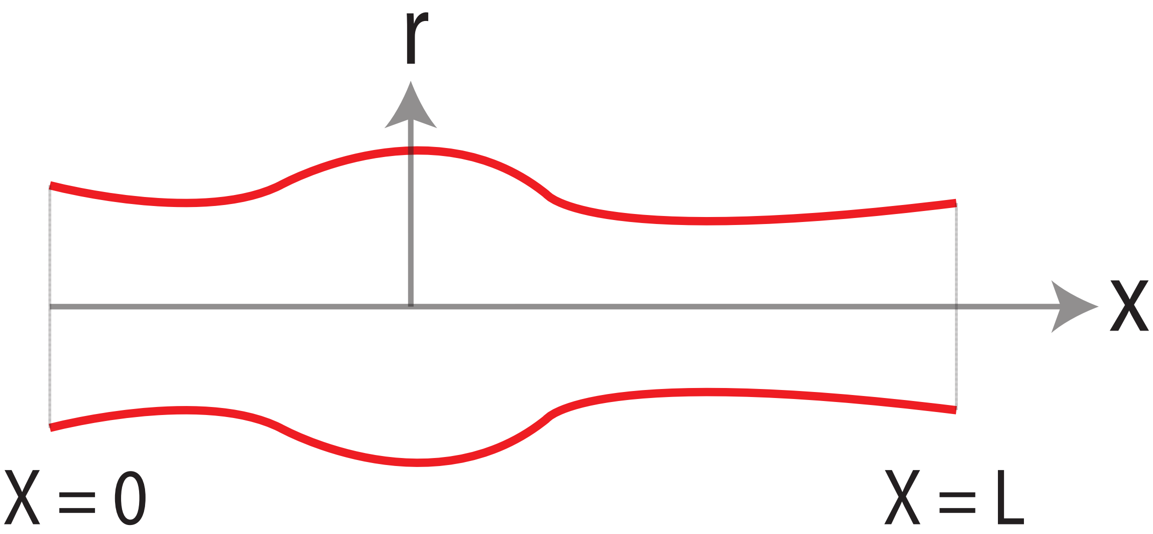

Figure 1.2: Diagram showing the meaning of the x and r coordinates

6. The no-slip boundary condition holds on the vessel wall, that is, $u_x(x, R(x,t), t) = 0$. In the transversal direction, the fluid on the wall is assumed to move with the vessel wall itself, meaning $u_r(x, R(x,t), t) = \partial_t R(x,t)$.

The x-momentum and continuity equations of the Navier-Stokes equations are (for a reference, see [1])

$$\frac{\partial u_x}{\partial t} + u_r \frac{\partial u_x}{\partial r} + \frac{u_\theta}{r}\frac{\partial u_x}{\partial \theta} + u_x \frac{\partial u_x}{\partial x} = -\frac{1}{\rho}\frac{\partial p}{\partial x} + \frac{\mu}{\rho}\left[\frac{1}{r}\frac{\partial}{\partial r}\left(r\frac{\partial u_x}{\partial r}\right) + \frac{1}{r^2}\frac{\partial^2 u_x}{\partial \theta^2} + \frac{\partial^2 u_x}{\partial x^2}\right]$$

$$\frac{1}{r}\frac{\partial}{\partial r}(r u_r) + \frac{1}{r}\frac{\partial u_\theta}{\partial \theta} + \frac{\partial u_x}{\partial x} = 0$$

Using the above assumptions, these equations reduce to the following:

$$\frac{\partial u_x}{\partial t} + u_r \frac{\partial u_x}{\partial r} + u_x \frac{\partial u_x}{\partial x} = -\frac{1}{\rho}\frac{\partial P}{\partial x} + \frac{\mu}{\rho}\left[\frac{1}{r}\frac{\partial}{\partial r}\left(r\frac{\partial u_x}{\partial r}\right) + \frac{\partial^2 u_x}{\partial x^2}\right] \tag{1.1}$$

$$\frac{1}{r}\frac{\partial}{\partial r}(r u_r) + \frac{\partial u_x}{\partial x} = 0 \tag{1.2}$$

It is also common to ignore the $\partial_{xx} u_x$ term. This can be justified by a nondimensionalization argument where the axial velocity is assumed to be substantial greater than the radial velocity [26, 64]. We now drop this $\partial_{xx}u_x$ term and integrate both equations over the cross-sectional area of the vessel. In doing so it will be useful to define the flowrate, $Q(x,t)$, and cross-sectional area, $A(x,t)$:

$$\begin{aligned} Q(x,t) &\triangleq 2\pi \int_0^{R(x,t)} u_x(x,r,t) r dr \\ A(x,t) &\triangleq \pi R(x,t)^2 \end{aligned}$$

To begin, we integrate the continuity equation (1.2) over vessel cross-sections.

$$\begin{aligned} 0 &= 2\pi \int_0^R \partial_r(ru_r)dr + 2\pi \int_0^R \frac{\partial u_x}{\partial x} r dr \\ &= 2\pi R u_r(x,R,t) + 2\pi \left[\partial_x \int_0^R u_x r dr - \partial_x R u_x(x,R,t) R \right] \\ &= 2\pi R \partial_t R + \partial_x Q \\ &= \partial_t A + \partial_x Q \end{aligned}$$

We now integrate the x-momentum equation (1.1) over vessel cross-sections. The integration of the first term in (1.1) is straightforward:

$$2\pi \int_0^R \frac{\partial u_x}{\partial t} r dr = 2\pi \left[\frac{\partial}{\partial t} \int_0^R u_x r dr - \frac{\partial R}{\partial t} u_x R \right] = \partial_t Q$$

where in the above we have used the fact that $u_x = 0$ when $r = R$, which follows from the no-slip condition. The integrals of the nonlinear terms of (1.1) do not admit a closed form formulation in terms of A and Q:

$$\begin{aligned} 2\pi \int_0^R u_r \frac{\partial u_x}{\partial r} r dr &= 2\pi \left[u_r u_x r \Big|_0^R - \int_0^R u_x \frac{\partial (u_r r)}{\partial r} \right] \\ &= 2\pi \int_0^R u_x \frac{\partial u_x}{\partial x} r dr \\ &= \pi \int_0^R \frac{\partial (u_x^2)}{\partial x} r dr \end{aligned}$$

In the above we have used (1.2) and the fact that u_x vanishes when $r = R$. Since P is constant on cross sections, the computation of the integral of $\partial P / \partial x$ is trivial:

$$\frac{1}{\rho} 2\pi \int_0^R \frac{\partial P}{\partial x} r dr = \frac{A}{\rho} \partial_x P.$$

The integral of the final term in (1.1) cannot be written in terms of Q and A and requires information on the derivative of u_x in the radial direction at the vessel wall:

$$2\pi\frac{\mu}{\rho}\int_0^R \frac{1}{r}\partial_r(r\partial_r u_x)rdr = 2\pi\frac{\mu}{\rho}r\partial_r(u_x)\Big|_0^R = 2\pi\frac{\mu}{\rho}R\partial_r(u_x)\Big|_{r=R}.$$

We now plug the above results into (1.1)

$$\partial_t Q + 2\pi\int_0^R \frac{\partial(u_x^2)}{\partial x}rdr + \frac{A}{\rho}\partial_x P = 2\pi\frac{\mu}{\rho}R\partial_r(u_x)\Big|_{r=R}$$

For the x-momentum equation, it is impossible to obtain a closed equation for A and Q without additional assumptions. To complete this process, we need to make additional assumptions to handle the inertial term (the integral of u_x^2), the wall friction term (the term on the right hand side involving $\partial_r(u_x)\Big|_{r=R}$, and the relationship between P and A. The typical approach to address these two terms is to assume a particular velocity profile (see [91] for a summary of various velocity profiles). We assume that the x-component of velocity adheres to the following profile, where U denotes the cross-sectional average of u_x and γ is a parameter that determines the shape of the profile

$$u_x(x,r,t) = \frac{\gamma+2}{\gamma}U(x,t)\left[1-\left(\frac{r}{R(x,t)}\right)^\gamma\right]$$

This assumption allows us to write the inertial and wall friction terms explicitly in terms of A and Q:

$$\begin{aligned}
2\pi\int_0^R \frac{\partial(u_x^2)}{\partial x}rdr &= \partial_x\int_0^R u_x^2 rdr - \partial_x R u_x^2(x,R,t)R \\
&= 2\pi\left[\frac{\gamma+2}{\gamma}\right]^2\partial_x\left(U(x,t)^2\int_0^R r\left[1-\left(\frac{r}{R}\right)^\gamma\right]dr\right) \\
&= 2\pi\left[\frac{\gamma+2}{\gamma}\right]^2\partial_x\left(U(x,t)^2\int_0^R \left[r-2\frac{r^{\gamma+1}}{R^\gamma}+\frac{r^{2\gamma+1}}{R^{2\gamma}}\right]dr\right) \\
&= 2\pi\left(\frac{\gamma+2}{\gamma}\right)^2\partial_x\left(U(x,t)^2R(x,t)^2\left[\frac{1}{2}-\frac{2}{\gamma+2}+\frac{1}{2(\gamma+2)}\right]\right) \\
&= \frac{\gamma+2}{\gamma+1}\partial_x\left(\frac{Q^2}{A}\right)
\end{aligned}$$

$$2\pi\frac{\mu}{\rho}R\partial_r(u_x)\Big|_{r=R} = -2\pi\frac{\mu}{\rho}R(\gamma+2)U(x,t)\left(\frac{R^{\gamma-1}}{R^\gamma}\right) = -\frac{2\pi\mu(\gamma+2)}{\rho}\frac{Q}{A}$$

To finish closing the system, we use the following constitutive law that relates P to A

$$P - P_0 = \frac{4Eh}{3r_0}\left(1 - \sqrt{\frac{A_0}{A}}\right) \tag{1.3}$$

In the above, P_0 is the pressure applied to the wall from outside the vessel, E is Young's modulus, h is the thickness of the vessel wall, and r_0 is the radius of the unstressed vessel ($A_0 = \pi r_0^2$). The constitutive law (1.3) is derived by treating the arterial wall as a thin elastic shell whose deformations are axisymmetric [63].

This yields the following 1st-order system of partial differential equations for A and Q:

$$\partial_t A + \partial_x Q = 0 \tag{1.4}$$

$$\partial_t Q + \frac{\gamma+2}{\gamma+1}\partial_x\left(\frac{Q^2}{A}\right) + \frac{A}{\rho}\partial_x P = -\frac{2\pi\mu(\gamma+2)}{\rho}\frac{Q}{A} \tag{1.5}$$

In Chapter 2 we show that this system is a hyperbolic system of balance laws. Although hyperbolic systems are well known for often lacking smooth solutions [47], in the regimes we consider the solutions appear to be smooth (see Appendix A). This allows these equations to be solved numerically with little difficulty.

Chapter 2

Boundary Conditions for Hemodynamics

To begin our discussion of boundary conditions, we determine the eigenvalues of the Jacobian matrix of the system (1.4,1.5). If these eigenvalues are real, their signs determine the locations at which boundary conditions must be imposed. For this system, the Jacobian matrix is

$$J = \begin{pmatrix} 0 & 1 \\ \dfrac{AP'(A)}{\rho} + \bar{\gamma}\dfrac{Q^2}{A^2} & 2\bar{\gamma}\dfrac{Q}{A} \end{pmatrix}$$

where $\bar{\gamma} = (\gamma + 2)/(\gamma + 1)$. The eigenvalues of this Jacobian are:

$$\bar{\gamma}U \pm \sqrt{\frac{2Eh}{3R}}$$

where $R = \sqrt{A/\pi}$ and $U = Q/A$ is the cross sectionally averaged blood velocity. In this dissertation, we follow [63] and set $Eh/r_0 = k_1 e^{k_2 r_0} + k_3$, where $k_1 > 0$ and $k_3 = 8.65 \times 10^5$. This means that $\sqrt{2Eh/3R} = \sqrt{2Eh/3r_0}\sqrt{r_0/R} \geq \sqrt{2(8.65)(10^5)/3}\sqrt{r_0/R} \approx 759\sqrt{r_0/R}$. We use a value of $\gamma = 2$, so $\bar{\gamma} = 4/3$. Branching parameter data in Section 3.1.1 implies that the total cross sectional area increases as the distance from the heart increases. Conservation of flowrate at junctions would then imply that blood velocity tends to decrease as you move down the arterial network away from the heart. We expect the maximum value of U to occur at the aorta, where it is roughly 100 cm/s (see Chapter 5). Therefore, we would only expect both eigenvalues to be positive if $r_0/R < (400/(3 \times 759))^2 \approx 0.03$. We do not expect for r_0/R to be less than 0.03 in any physiological setting as this would imply that the vessel radius, R is more than 30 times bigger than its unstressed radius, r_0.

This argument shows that the Jacobian of this system admits two real eigenvalues of differing signs. Thus the system (1.4,1.5) is hyperbolic and we need to impose one scalar condition at each end of each vessel. The appropriate boundary conditions depend on a given vessel's location in the arterial network being modeled. We classify each boundary as one of the following types:

1. Inflow Boundaries - Points where blood is flowing into the network. Although the velocity of blood does not have a definite sign for all vessels in the human body, we are able to determine the direction of blood flow in all boundary vessels in networks simulated in this document. For example, see vessels 1, 8, and 9 in Figure 1.1.

2. Junctions - Points where a vessel intersects another vessel. For example, see the intersection of vessels 1, 2, and 3 in Figure 1.1.

3. Outflow Boundaries - Points where blood is flowing out of the network. For example, see vessels 4, 5, 10, 11, 15, and 16 in Figure 1.1.

Each of these boundary types is fundamentally different. The purpose of inflow and outflow boundaries is to incorporate what is "outside" the modeling domain. For inflow boundaries, this corresponds to a relatively small number of larger vessels and the heart. For outflow boundaries, this corresponds to an enormous number of small arteries, capillaries, and veins. At junctions, boundary conditions are motivated by continuity and conservation principles.

Inflow Boundary Conditions

In this dissertation, we perform numerous simulations of blood flow in the Circle of Willis, a ring-like structure of arteries at the base of the brain. At inflow boundaries of the Circle of Willis, we enforce $Q(t)/A(t) = \mathcal{U}(t)$, where $\mathcal{U}(t)$ is velocity data measured using digital transcranial Doppler technology at the Beth Israel Deaconess Medical Center. The raw data contains 8 "periods" of quasi-periodic noisy data, so we average this data to obtain a smoother waveform. Specifically, for $i = 0, ..., 7$, we approximate the following integrals via discrete Fourier transform

$$\widehat{U}_k^i = \frac{1}{T} \int_i^{i+T} U(t) e^{i\omega_k t} dt$$

where $\omega_k = 2\pi k/T$, T is the period length. We then take the simple average of these 8 Fourier representations. The raw and averaged data obtained through this procedure are displayed in Figure 2.1. When implemented, each of these three curves is placed in phase with the others. Since each inflow point of the Circle of Willis is roughly the same distance from the heart, we

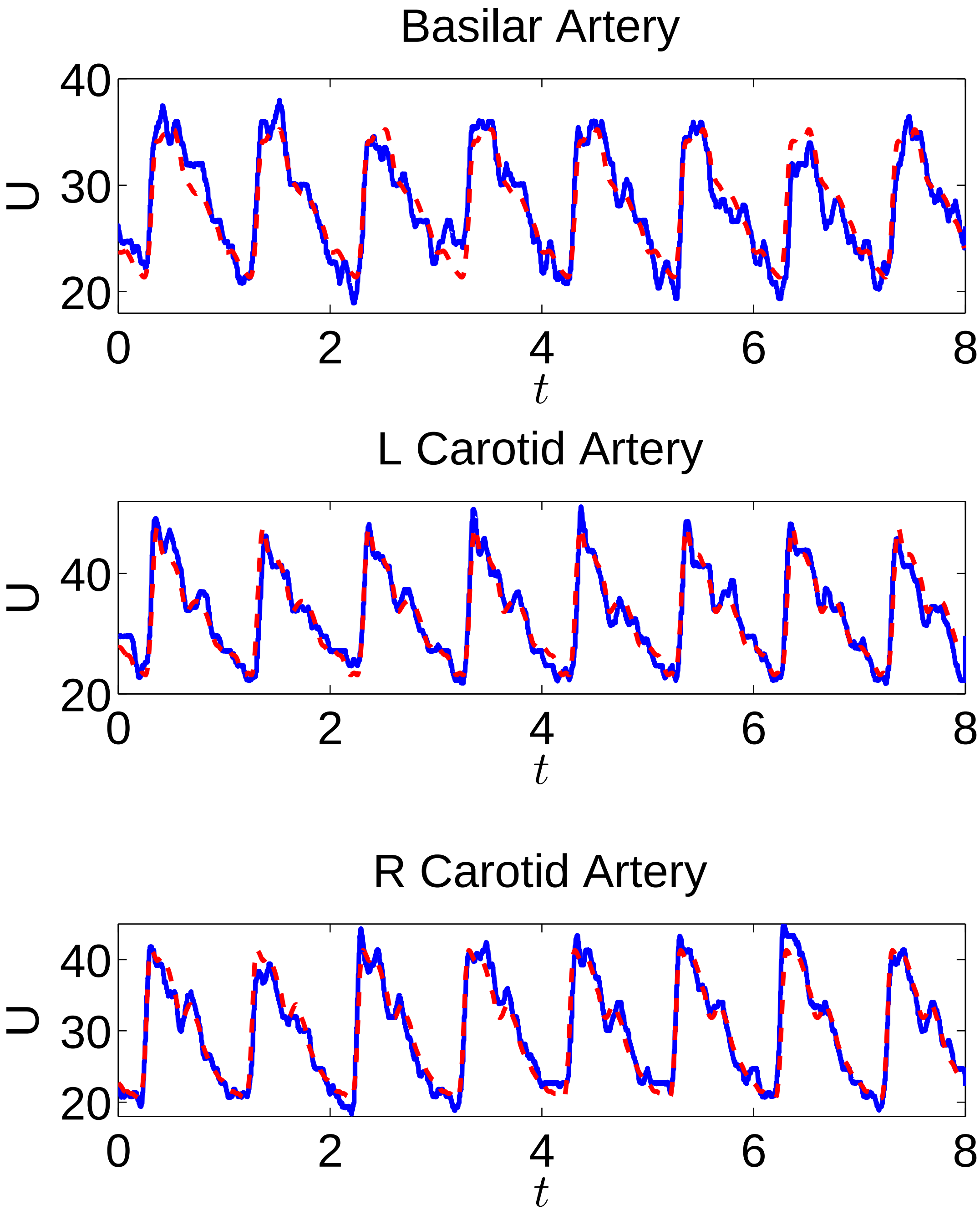

Figure 2.1: Inflow velocity data used as a boundary condition in simulations of the Circle of Willis. The blue curve corresponds to raw, measured velocity data, and the red, dashed curve is the smoothed data.

expect these curves will be roughly in phase. Another similar inflow condition is to impose the flowrate, which we do in a simulation of the systemic arterial tree in Chapter 5.

An alternative inflow boundary condition is to couple the PDE system (1.4,1.5) to a heart model if the inflow boundary vessel is the aorta. One example of such a model is the time-varying elastance model [75], which enforces:

$$E(t) = \frac{p_{lv}(t)}{V_{lv}(t) - V_0}$$

p_{lv} and V_{lv} are the pressure and volume of the left ventricle, and $E(t)$ is the time-varying elastance of the left ventricle. An empirical function for $E(t)$ can be found in [77]. Alternative heart models to the time varying elastance model exist, such as the single-fiber model [7, 12, 24].

Junction Boundary Conditions

At junctions, we require that the pressure be continuous and the flowrate be conserved. Specifically, we impose

$$\sum_{k=1}^{m} Q_{\mathrm{IN}}^{(k)}(t, L_k) = \sum_{k=1}^{n} Q_{\mathrm{OUT}}^{(k)}(t, 0), \tag{2.1}$$

$$P_{\mathrm{IN}}^{(1)}(t, L_1) = \cdots = P_{\mathrm{IN}}^{(m)}(t, L_m) = P_{\mathrm{OUT}}^{(1)}(t, 0) = \cdots = P_{\mathrm{OUT}}^{(n)}(t, 0), \tag{2.2}$$

where L_k denotes the length of vessel k. Such boundary conditions are common in the field [26, 9, 73, 63]. Some authors choose to enforce continuity of the total pressure $P + \frac{1}{2}\rho U^2$ rather than the continuity of P, that is,

$$P_{\mathrm{IN}}^{(1)}(t, L_1) + \frac{1}{2}\rho\left(\frac{Q_{\mathrm{IN}}^{(1)}(t, L_1)}{A_{\mathrm{IN}}^{(1)}(t, L_1)}\right)^2 = \cdots = P_{\mathrm{IN}}^{(m)}(t, L_m) + \frac{1}{2}\rho\left(\frac{Q_{\mathrm{IN}}^{(m)}(t, L_m)}{A_{\mathrm{IN}}^{(m)}(t, L_m)}\right)^2 \tag{2.3}$$

$$= P_{\mathrm{OUT}}^{(1)}(t, 0) + \frac{1}{2}\rho\left(\frac{Q_{\mathrm{OUT}}^{(1)}(t, 0)}{A_{\mathrm{OUT}}^{(1)}(t, 0)}\right)^2 = \cdots = P_{\mathrm{OUT}}^{(n)}(t, 0) + \frac{1}{2}\rho\left(\frac{Q_{\mathrm{OUT}}^{(n)}(t, 0)}{A_{\mathrm{OUT}}^{(n)}(t, 0)}\right)^2 \tag{2.4}$$

The authors of [9] suggest that there is only a negligible difference between (2.2) and (2.4), and we simply use (2.2) rather than the conservation of total pressure boundary condition in this work. Additional information on this condition may be found in [53, 3].

Outflow Boundary Conditions

We use four different types of outflow boundary conditions at various points in this work: the pure resistor boundary condition, the 3-element RCR Windkessel, the periodic structured tree, and the generalized structured tree. The pure resistor states that the pressure at each outflow boundary is proportional to the flowrate at that point. Specifically,

$$P = R_0 Q$$

here R_0 is a constant, but R_0 can vary between different outlets. The pure resistor boundary condition can be derived by using Poiseuille's law within individual vessels and enforcing pressure continuity and flowrate conservation at junctions. Although this boundary condition is simple to implement and sees some use in practice [78, 95, 31], it often produces physiologically unreasonable results in general ([9, 36], and Section 5.3 of this work.) Furthermore, this condition also forces the pressure and flowrate to be in phase, which is not the case physiologically [36]. Also, it is not obvious how to determine the resistance parameter R_0 without direct measurements of pressure and flowrate at each outlet of the arterial network.

The RCR Windkessel boundary condition enforces a relationship between the pressure, flowrate, and their time derivatives.

$$CR_1R_2\partial_t Q + (R_1 + R_2)Q = CR_2\partial_t P + P.$$

C, R_1, and R_2 are parameters whose specific values are dependent on the particular outflow boundary vessel. The Windkessel differs from the pure resistor by incorporating the compliant effect of the elastic arteries (the Windkessel reduces to the pure resistor condition when $C = 0$). The Windkessel can be thought of as an RCR electrical circuit, where P represents voltage and Q represents current. An unfortunate drawback of the Windkessel model is that the parameters have limited physiological meaning [100], and in the absence of flow and pressure measurements, they must be estimated on a vessel by vessel basis. Some rough rules of thumb do exist for estimating these parameters [73, 91]. Alastruey et. al. [4, 5] also gave methods to estimate the Windkessel parameters.

The structured tree boundary condition is a physiologically based boundary condition that is derived by treating the "un-modeled" vascular network outside an outflow vessel as a structured, self-similar tree of arteries. Within these arteries, a linearized model is solved exactly to provide a relation between pressure and flowrate at the outflow boundary. This approach will be discussed at length in Chapter 3. Unfortunately, the original derivation of this condition requires an assumption of periodicity in time, which is not the case in a variety of situations. A generalized version of this condition that is applicable to general, non-periodic flows will be derived in Chapter 4.

There are a variety of other outflow boundary conditions that we do not consider in detail in this work. One simple option is to impose the pressure at outlets. Although straightforward to implement, this condition requires one to have knowledge of the correct pressure. For simulations with multiple outlets, there is the additional problem of ensuring that the phases of the imposed pressures are appropriately aligned [36]. Another option, described in [36], is to impose the velocity at each outlet. The authors of [36] describe a way to do so while ensuring stability. An obvious limitation of this condition is that it requires one to know the velocity values at outlets, which is unreasonable in certain cases. In fact, attaining flow information at the outlets is often the central goal of numerical simulation [3, 27]. Other outflow boundary conditions include the 4-element Windkessel [60] and the imposition of a single, long tapered vessel [59].

Chapter 3

Implementation of The Original Structured Tree

As discussed in Chapter 2, fully detailed modeling of the entire cardiovascular system is unrealistic due to the massive size and complexity of the arterial network. Although it is possible to partially mitigate this issue by only modeling a small subset of the arterial network in detail, the "un-modeled" network still must be taken into account through boundary conditions. Therefore, it is necessary to develop boundary conditions that correctly account for the effects of the un-modeled vasculature.

The structured tree boundary condition, developed by Olufsen, is a physiologically based boundary condition which relies on solving a blood flow model in a self-similar binary tree of arteries [62, 63, 64]. In Section 3.1, we briefly overview Olufsen's derivation of the structured tree, which is based on Womersley's solution to the linearized Navier-Stokes momentum equation in a rigid-walled tube. In Section 3.1.3, we provide an alternative derivation that incorporates elastic arterial walls by solving the linearization of the equations derived in Section 1.2.1.

The structured tree condition provides a condition on the Fourier coefficients of the states, so its implementation as a boundary condition in the time domain is necessarily nontrivial. In Section 3.2 we show that the implementation method advocated by Olufsen et. al. in [64] inappropriately makes use of the convolution theorem, which raises serious theoretical and practical questions. Despite this issue, we then show that the specific implementation advocated by Olufsen et. al. in [64] is valid, but its interpretation as a convolution integral is dangerous and misleading.

In [62], Olufsen noted that the structured tree condition has a critical sensitivity to the parameter that determines where the self-similar arterial tree terminates. In Section 3.3, we provide an analytical explanation of the cause of this sensitivity. Additionally, we provide numerical results quantifying the strong dependence of model output on this termination parameter.

3.1 Derivation of Original Structured Tree

The structured tree boundary condition was originally proposed by Olufsen [62, 63, 64]. Taylor also considered wave propagation in trees of arteries [86, 87] in a similar manner. Olufsen's derivation of the structured tree boundary condition can be broken up into two main components. First, Olufsen treats the downstream vasculature as a self-similar binary tree of arteries. Within this tree, the linearized, axisymmetric Navier-Stokes equations are solved exactly by assuming that the flow and pressure are periodic in time [64].

3.1.1 Geometry of the Structured Tree

The concept of the structured tree model of the arterial network, as described for instance in [63], assumes that vessels end by bifurcating into two daughter vessels. Vessels are taken to be cylindrical. For a parent vessel of radius r_p, the radii of the daughter vessels r_{d_1} and r_{d_2} are determined by two scaling parameters ξ and η

$$\begin{aligned} r_p^{\xi} &= r_{d_1}^{\xi} + r_{d_2}^{\xi}, \\ \eta &= \left(r_{d_2}/r_{d_1}\right)^2, \end{aligned}$$

where η is the ratio of the cross-sectional areas of the two daughter vessels. The meaning of ξ is less obvious, although $\xi = 2$ corresponds to conservation of area at the bifurcation. Knowledge of these two parameters allows us to express the radii of the two daughter vessels in terms of the radius of the parent

$$r_{d_1} = \alpha\, r_p, \quad r_{d_2} = \beta\, r_p,$$

where $\alpha = \left(1 + \eta^{\xi/2}\right)^{-1/\xi}$ and $\beta = \alpha\sqrt{\eta}$. Additionally, the ratio of a vessel's length to its radius, λ, is assumed to be constant. Vessels with radius less than a specified minimum radius, r_{min}, terminate, i.e., they do not bifurcate.

3.1.2 Hemodynamics in the Tree

In [64], Olufsen treats the Navier-Stokes momentum equation in a way similar to Womersley's classical solution [101]. Specifically, the flow is assumed to be axisymmetric, the angular component of velocity is taken to be zero, body forces are ignored, the vessel is treated as a rigid pipe with radius r_0, and the equations are linearized. The linearization is justified by the fact that this model is designed to be used in the smaller arteries, where viscous effects become more important than inertial effects [18]. These simplifications yield the following simplified form of the Navier-Stokes axial momentum equation:

$$\frac{\partial u_x}{\partial t} + \frac{1}{\rho}\frac{\partial P}{\partial x} = \frac{\nu}{r}\frac{\partial}{\partial r}\left(r\frac{\partial u_x}{\partial r}\right), \tag{3.1}$$

where u_x is the axial velocity component. Olufsen then assumes u_x, P, and Q are periodic in time with period T.

$$P(t) = \sum_{k=-\infty}^{\infty} \hat{P}_k e^{i\omega_k t} \qquad\qquad Q(t) = \sum_{k=-\infty}^{\infty} \hat{Q}_k e^{i\omega_k t}$$

where $Q(x,t) = 2\pi\int_0^{r_0} u_x(x,r,t) r dr$ and $\omega_k = 2\pi k/T$, where T is the period of P and Q. Equation (3.1) is then multiplied by $e^{-i\omega_k t}$ and integrated in time from 0 to T. The resulting equation is then solved exactly and integrated over cross sectional area to yield the following ODE:

$$\hat{Q}_k = -\frac{A_0}{\rho}\partial_x \hat{P}_k \left(1 - F_k\right) \tag{3.2}$$

where $F_k = \frac{2J_1(\mathrm{w}_k)}{\mathrm{w}_k J_0(\mathrm{w}_k)}$, with J_n being the nth order Bessel function, and $\mathrm{w}_k = r_0\sqrt{-i\omega_k\rho/\mu}$. In [64], Olufsen uses the continuity equation derived in Section 1.2.1.

$$\partial_t A + \partial_x Q = 0$$

Linearizing this equation about $A = A_0$ yields

$$C\partial_t P + \partial_x Q = 0, \tag{3.3}$$

where $C = \frac{\partial A}{\partial P}\big|_{P=P_0} = 3A_0 r_0/2Eh$, which is obtained from the following elastic constitutive law (see (1.3), Section 1.2.1):

$$P - P_0 = \frac{4Eh}{3r_0}\left(1 - \sqrt{\frac{A_0}{A}}\right) \tag{3.4}$$

where E is the elastic modulus, h is the thickness of the vessel wall, r_0 is the radius of the unstressed vessel. Multiplying the linearized continuity equation (3.3) by $e^{-i\omega_k t}$ and integrating from 0 to T yields the following ODE:

$$i\omega_k C \partial_t \hat{P}_k + \partial_x \hat{Q}_k = 0 \tag{3.5}$$

Equations (3.2) and (3.5) are then solved analytically, yielding

$$\hat{Q}_k(0) = i c_k C \hat{P}_k(L) \sin\left(\frac{\omega_k}{c_k} L\right) + \hat{Q}_k(L) \cos\left(\frac{\omega_k}{c_k} L\right)$$

$$\hat{P}_k(0) = \hat{P}_k(L) \cos\left(\frac{\omega_k}{c_k} L\right) + \frac{i}{c_k C} \hat{Q}_k(L) \sin\left(\frac{\omega_k}{c_k} L\right)$$

where $c_k = \sqrt{(1 - F_k)\frac{A_0}{\rho C}}$, $A_0 = \pi r_0^2$, and L is the length of the vessel. The solution for $\hat{P}_k$ may be divided by the solution for $\hat{Q}_k$ to get an expression for the vascular impedance, $\hat{Z}_k$, where $\hat{Z}_k \triangleq \hat{P}_k / \hat{Q}_k$:

$$\hat{Z}_k(0) = \frac{\hat{Z}_k(L) + i\,(c_k C)^{-1} \tan\left(\frac{\omega_k L}{c_k}\right)}{1 + i c_k C \tan\left(\frac{\omega_k L}{c_k}\right) \hat{Z}_k(L)}, \tag{3.6}$$

$$\hat{Z}_0(0) \triangleq \lim_{\omega_k \to 0} \hat{Z}_k(0) = \hat{Z}_0(L) + \frac{8\mu\lambda}{\pi r_0^3}. \tag{3.7}$$

The limit with respect to ω_k was done by viewing ω_k in the continuous sense. The above expressions relate the impedance at the end of an individual vessel ($x = L$) to the impedance at the beginning of that vessel ($x = 0$). At junctions, Olufsen assumes that the pressure is continuous and flowrate is conserved:

$$P^{(pa)}(L,t) = P^{(d1)}(0,t) = P^{(d2)}(0,t)$$
$$Q^{(pa)}(L,t) = Q^{(d1)}(0,t) + Q^{(d2)}(0,t)$$

Computing the Fourier coefficients of each side of the above expressions yields the following condition on the impedance at junctions:

$$\frac{1}{\hat{Z}_k^{(pa)}(L)} = \frac{1}{\hat{Z}_k^{(d1)}(0)} + \frac{1}{\hat{Z}_k^{(d2)}(0)} \tag{3.8}$$

The structured tree model is closed by assuming the impedance at the ends of all terminal vessels to be equal to a specific constant denoted $\hat{Z}_{term}$. This value is typically taken to be 0

[63, 64]; we take $\hat{Z}_{term} = 0$ in all analysis unless otherwise noted. Given merely the radius of the root vessel, the impedance at the end of that vessel may be calculated for any integer k using the above results. The geometric scaling laws determine the length and radii of all vessels in the tree. The terminal impedance is then imposed at the ends of all terminal vessels, and by repeatedly applying expressions (3.6) and (3.8) in succession, a value for the impedance of the root vessel is obtained. Figure 3.1 contains a visualization of this process, and an explicit description is in Appendix A.0.3.

3.1.3 Alternative Formulation

In Section 3.1.2, the momentum equation was solved by treating the vessel as a rigid cylindrical tube. Here, we linearize and solve the 1D equations (1.4,1.5) derived in Section 1.2.1, which incorporate elastic arterial walls in the momentum equation. In addition, the work in the following section serves as a general blueprint for how one could derive a structured tree condition using one's particular equations of choice. In Section 1.2.1, we derive equations (1.4) and (1.5) by assuming blood flow follows the axisymmetric, incompressible Navier-Stokes equations. The effect of gravity is neglected. The equations are then averaged on-cross sections, leading to the following one-dimensional formulation:

$$\partial_t A + \partial_x Q = 0, \tag{3.9}$$

$$\partial_t Q + \frac{\gamma+2}{\gamma+1}\,\partial_x\left(\frac{Q^2}{A}\right) + \frac{A}{\rho}\,\partial_x P = -2\pi(\gamma+2)\,\frac{\mu}{\rho}\,\frac{Q}{A}, \tag{3.10}$$

where A is the cross-sectional area and Q the flowrate; the density ρ is assumed to be constant, μ is the viscosity. The system is closed by a constitutive law for the pressure P (3.4). The parameter γ determines the velocity profile. More precisely, the axial velocity is given by

$$u_x(r,x,t) = \frac{\gamma+2}{\gamma}U(x,t)\left(1-\left(\frac{r}{R(x,t)}\right)^{\gamma}\right), \tag{3.11}$$

where $R(x,t)$ is the radius of the vessel ($A = \pi R^2$), and $U = Q/A$ is the cross-sectionally averaged velocity.

In a second step, the system (3.9, 3.10) is linearized in A around the constant value A_0 and in Q around $Q = 0$. Further, the system is expressed in terms of P and Q, rather than A and

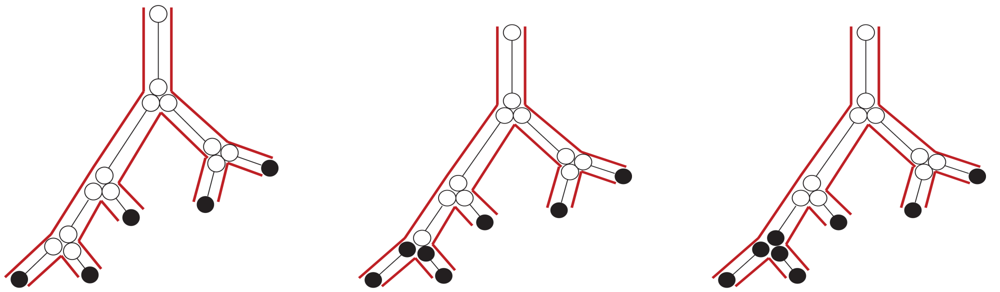

(a) Impose $\hat{Z}_{term}$ at leafs

(b) Use (3.6)/(3.7) to move from end to beginning of a vessel

(c) Use (3.8) to move across junction

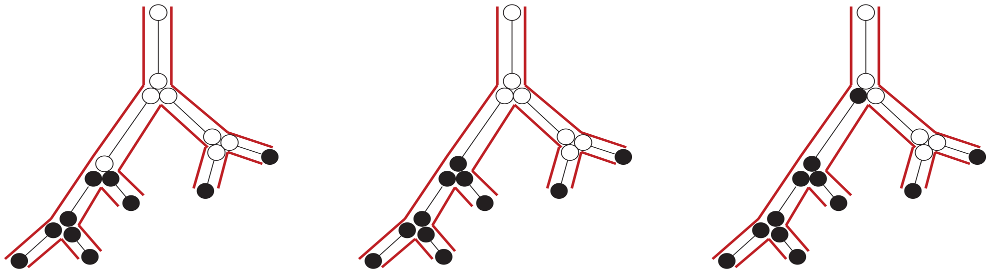

(d) Use (3.6)/(3.7)

(e) Use (3.8) to move across junction

(f) Use (3.6)/(3.7)

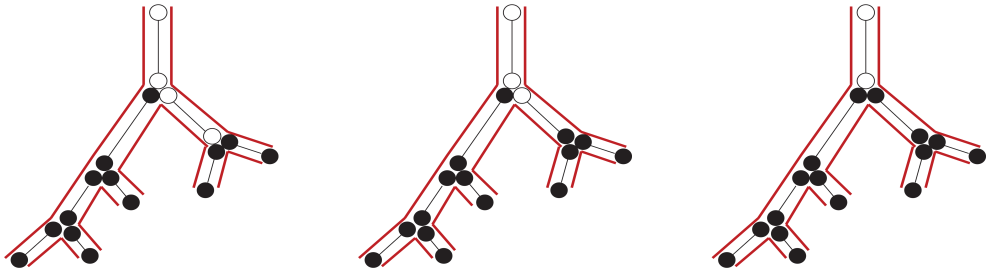

(g) Use (3.6)/(3.7)

(h) Use (3.8) to move across junction

(i) Use (3.6)/(3.7)

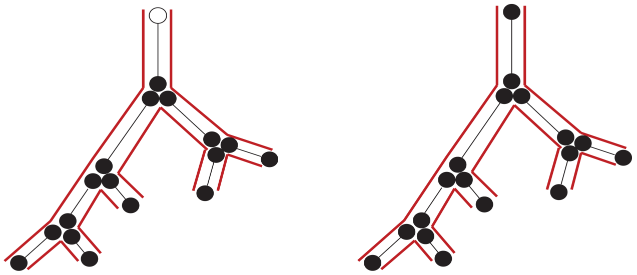

(j) Use (3.8) to move across junction

(k) Use (3.6)/(3.7)

Figure 3.1: Visualization of Olufsen's algorithm for computing the impedance at the root of the structured tree.

Q through a linearization of the constitutive equation (3.4). This results in

$$C\,\partial_t P + \partial_x Q = 0 \tag{3.12}$$

$$\partial_t Q + \frac{A_0}{\rho}\,\partial_x P = -2\pi(\gamma+2)\,\frac{\mu}{\rho}\,\frac{Q}{A_0}, \tag{3.13}$$

where $C = \frac{\partial A}{\partial P}\big|_{P=P_0} = 3A_0 r_0/2Eh$ is the compliance. The third and final step consists in assuming that P and Q are periodic in time and are suitably regular to justify their representation by Fourier series. We then multiply equations (3.12) and (3.13) by $e^{-i\omega_k t}$ and integrated in time from 0 to T. This gives the following system for their Fourier coefficients

$$i\omega_k C\,\hat{P}_k + \partial_x \hat{Q}_k = 0, \tag{3.14}$$

$$(i\omega_k + \delta)\hat{Q}_k + \frac{A_0}{\rho}\,\partial_x \hat{P}_k = 0, \tag{3.15}$$

where $\delta = 2\frac{\mu(\gamma+2)}{\rho r_0^2}$. Solving the above system yields

$$\hat{Z}_k(0) = \frac{\hat{Z}_k(L) + i(d_k C)^{-1}\tan\left(\frac{\omega_k}{d_k}L\right)}{1 + i d_k C\tan\left(\frac{\omega_k}{d_k}L\right)\hat{Z}_k(L)}, \tag{3.16}$$

$$\hat{Z}_0(0) = \lim_{\omega_k\to 0}\hat{Z}_k(0) = \hat{Z}_0(L) + \frac{2(\gamma+2)\mu\lambda}{\pi r_0^3}, \tag{3.17}$$

where d_k satisfies $d_k^2 = \frac{\omega_k A_0}{(\omega_k - i\delta)\rho C}$ and $\lambda = L/r_0$.

The expressions for the impedances (3.16, 3.17) and (3.6, 3.7) are similar. In fact, the values of the average impedance $\hat{Z}_0(0)$ are identical for a Poiseuille flow, i.e., for $\gamma = 2$ in (3.17). For both models, direct evaluation shows $\hat{Q}_0(0) = \hat{Q}_0(L)$, i.e., the temporally averaged flow rate is spatially constant throughout the vessel. Denoting the corresponding value $\overline{Q}$, we observe that both (3.17) (with $\gamma = 2$) and (3.7) are simply the Hagen-Poiseuille equation [80]

$$\overline{P}(0) - \overline{P}(L) = \frac{8\mu L\overline{Q}}{\pi r_0^4},$$

where $\overline{P}(x) = \hat{P}_0(x)$. Figure 3.2 displays the root impedance when each of these formulations is implemented in the structured tree algorithm, showing that the use of these two formulations yields very similar results.

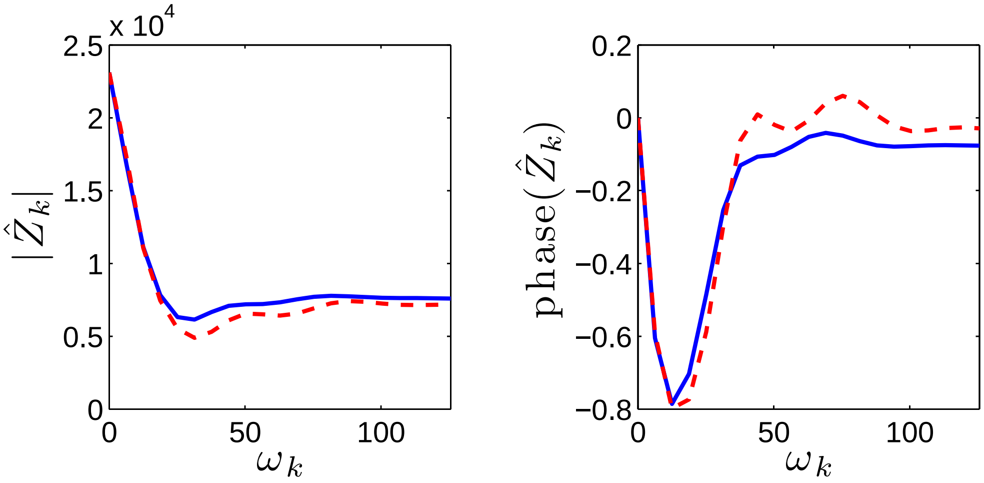

Figure 3.2: Modulus and phase of the root impedance generated by the structured tree algorithm using impedance relations (3.6) (blue, solid curve) and (3.16) (red, dashed curve). All parameter values (see Table 3.1) are from [64].

Table 3.1: Parameters used to generate Figure 3.2.

geometric parameters	$\xi = 2.76$, $\eta = 0.41$, $\lambda = 50$, $r_{root} = 0.2$cm, $r_{min} = 50\mu$m
fluid parameters	$\gamma = 2$, $\rho = 1.06$g cm^{-3}, $\mu = 0.0488$g cm^{-1}s^{-1}
elastic relations	$C = 3\pi r^3/2Eh$, $Eh/r = k_1 e^{k_2 r} + k_3$
elastic parameters	$k_1 = 2.00 \times 10^7$ gs^{-2}cm^{-1}, $k_2 = -22.53$ cm^{-1} $k_3 = 8.65 \times 10^5$ gs^{-2}cm^{-1}

3.2 Structured Tree Implementation

The purpose of the procedure outlined in Section 3.1 is to provide a boundary condition at outflow boundaries of an arterial network in which a more complicated model is solved numerically. At each outflow boundary, the structured tree gives the following condition:

$$\hat{P}_k = \hat{Z}_k \hat{Q}_k$$

where $\hat{P}_k$ and $\hat{Q}_k$ are the respective Fourier coefficients of pressure and flowrate, and $\hat{Z}_k$ is the kth Fourier coefficient of the impedance. Prior to running a simulation, values of $\hat{Z}_k$ may be computed for any k with minimal computational expense. $\hat{P}_k$ and $\hat{Q}_k$ are the Fourier coefficients of the state variables, which are not known a priori.

To illustrate issues involved with implementing the structured tree, we consider the following initial boundary value problem, which models the flow of blood in a single vessel where measured velocity data $\mathcal{U}(t)$ is imposed at the inlet of the vessel:

$$(\partial_t + F\partial_x)\begin{bmatrix} A \\ Q \end{bmatrix} = G \qquad x \in (0,L), t > 0 \tag{3.18}$$

$$Q(0,t) = \mathcal{U}(t)A(0,t) \qquad x = 0, t > 0 \tag{3.19}$$

$$\hat{P}_k(L) = \hat{Z}_k(L)\hat{Q}_k(L) \qquad x = L \tag{3.20}$$

The precise form of F and G in (3.18) may be found in (1.4,1.5). P and A are related through the elastic constitutive law (3.4). The structured tree condition (3.20) implicitly introduces the additional requirement that solutions to (3.18)-(3.20) be periodic in time. This periodicity requirement means that the imposed inflow velocity, $\mathcal{U}(t)$, must be periodic to avoid ill-posedness of the problem.

Due to the periodicity requirement, a natural approach to numerically solving (3.18)-(3.20) would be to use a Fourier expansion-based method in time. Such an approach would allow for a direct imposition of the Fourier coefficients of the impedance computed by the structured tree condition. However, requiring the use of Fourier-based time integration would limit the applicability of the structured tree as a boundary condition since most numerical methods for differential equations utilize a serial time-stepping algorithm that does *not* strictly enforce periodicity in time.

For the reasons outlined above, it is important to consider how the structured tree condition should be implemented in conjunction with a serial time-stepping method. The numerical solution generated by such a method will, of course, not be strictly periodic. This conflicts with the fact that the structured tree condition *requires* periodicity. This conflict generates practical and theoretical questions that require attention.

First, since the numerically computed approximations of these variables are not periodic and thus *do not have* Fourier coefficients, how can condition (3.20) be implemented? In Section 3.2.1, we show that the implementation method advocated by Olufsen et. al. in [7] inappropriately makes use of the convolution theorem, which raises serious theoretical and practical questions. Despite this issue, we then show that the specific implementation advocated by Olufsen et. al. in [7] is valid, but its interpretation as a convolution integral is misleading and introduces a number of potential pitfalls for users of the structured tree condition. Second, it is not clear in what sense non-periodic numerical approximations constitute a solution to the periodic problem (3.18)-(3.20). The procedure advocated by Olufsen et. al. in [64] is to numerically solve the problem until the solution converges to a periodic regime, with this periodic limit being taken as the solution to (3.18)-(3.20) [64]. In Section 3.2.2, we examine various aspects of this process and quantify the rate of convergence of the solution to a periodic regime through a fixed point analysis of the linearized problem.

3.2.1 Enforcement of Structured Tree Condition

The structured tree imposes conditions on the Fourier coefficients of the solution. This makes numerical implementation of the structured tree condition nontrivial since numerically generated solutions will not be strictly periodic. Additionally, the condition (3.20) must be transformed to an equivalent formulation in the time domain to be used along with a numerical method for solving differential equations. To deal with these issues, the implementation by Olufsen et. al. in [64] only considered the most recent "period" of the numerical solution. That is, at time t, only values Q and P in the time interval $[t-T,t]$ were considered. To obtain a condition in the time domain, in [64] Olufsen et. al. make use of the convolution theorem, which states that if the Fourier coefficients of $P(t)$ and $Q(t)$ are related by $\hat{P}_k = \hat{Z}_k\hat{Q}_k$, then $P(t)$ and $Q(t)$ are related by the following convolution integral [11]:

$$P(t) = \frac{1}{T}\int_0^T Z(\tau)Q(t-\tau)d\tau, \tag{3.21}$$

where Z is the function whose Fourier coefficients are $\hat{Z}_k$, and Z and Q are assumed to be integrable over $[t-T,t]$. For simplicity, we are omitting the spatial dependency, but it should be understood that all variables are being evaluated at the end of the vessel ($x = L$). In [64], the authors suggest numerically implementing (3.21) by discretizing the convolution integral via quadrature and approximating Z by an Inverse Discrete Fourier Transform of values of $\hat{Z}_k$. This yields the following condition at time $t = n\Delta t$:

$$P_M^{(n)} = \Delta t \sum_{k=0}^{N-1} Z^{(k)} Q_M^{(n-k)} \tag{3.22}$$

where $\Delta t = T/N$, and P_j^i is an approximation of $P(x_j, i\Delta t)$. Here x_j denotes the jth spatial node and M is the total number of spatial nodes in the vessel. Equation (3.22) provides a boundary condition for advancing from time $(n-1)\Delta t$ to time $n\Delta t$. At time $(n-1)\Delta t$, values of $Q_M^{(n-k)}$ are known for $k > 0$ and all values of $Z^{(k)}$ will have been computed as a preprocessing step. This means that (3.22) is a single equation relating the unknowns $P_M^{(n)}$ and $Q_M^{(n)}$.

However, as we show in Theorem 3.2.1, the function Z in (3.21) is *not* integrable. In the proof of this theorem, we make use of the Riemann-Lebesgue Lemma:

Riemann-Lebesgue Lemma [11]. *If $Z \in L_1(0,T)$, then*

$$\lim_{|k|\to\infty} \hat{Z}_k = 0$$

.

Theorem 3.2.1. *The function Z in (3.21) is not integrable*

Proof. We show that the expression (3.6) converges to a real, nonzero limit as $\omega_k \to \infty$. Olufsen evaluates $1 - F_k$ by the use of two different asymptotic expansions (one for $\omega_k \approx 0$, another for large values of ω_k) [63]. For large values of ω_k:

$$1 - F_k \approx 1 - \frac{2}{r}\sqrt{\frac{\mu}{i\omega_k \rho}}$$

Defining $\bar{C} = L\sqrt{\frac{\rho C}{A_0}}, \bar{D} = \frac{2}{r}\sqrt{\frac{\mu}{\rho}}$ (note $\bar{C}, \bar{D}$ are positive reals), and recalling that $c_k = \sqrt{(1-F_k)\frac{A_0}{\rho C}}$, we have

$$\begin{aligned}
\frac{\omega_k L}{c_k} &= \bar{C}\omega_k \left(1 - \bar{D}/\sqrt{i\omega_k}\right)^{-1/2} \\
&= \bar{C}\omega_k \left[1 - \bar{D}/\sqrt{2\omega_k} + i\bar{D}/\sqrt{2\omega_k}\right]^{-1/2} \\
&= \frac{\bar{C}\omega_k}{\sqrt[4]{1 - \bar{D}\sqrt{\frac{2}{\omega_k}} + \frac{\bar{D}^2}{\omega_k}}} e^{-\frac{i}{2}\arctan(f(\omega_k))}
\end{aligned}$$

where $f(\omega_k) = \bar{D}/(\sqrt{2\omega_k} - \bar{D})$

$$\begin{aligned}
Im\left(\frac{\omega_k L}{c_k}\right) &= \frac{-\bar{C}\omega_k}{\sqrt[4]{1 - \bar{D}\sqrt{\frac{2}{\omega_k}} + \frac{\bar{D}^2}{\omega_k}}} \sin\left[\frac{1}{2}\arctan\left(f(\omega_k)\right)\right] \\
&= \frac{-\bar{C}\omega_k}{\sqrt[4]{1 - \bar{D}\sqrt{\frac{2}{\omega_k}} + \frac{\bar{D}^2}{\omega_k}}} \frac{f(\omega_k)}{\sqrt{\left(1 + \sqrt{1 + f(\omega_k)^2}\right)^2 + f(\omega_k)^2}}
\end{aligned}$$

since $\lim_{k\to\infty} f(\omega_k) = 0$ and $\lim_{k\to\infty} \omega_k f(\omega_k) = +\infty$, $\lim_{k\to\infty} Im\left(\frac{\omega_k L}{c_k}\right) = -\infty$ and thus

$\lim_{k\to\infty} \tan\left(\frac{\omega_k L}{c_k}\right) = 1/i$. We use this fact to compute the high-frequency limit of the impedance

$$\begin{aligned}\lim_{k\to\infty} \hat{Z}_k^{root}(0) &= \lim_{k\to\infty} \frac{\hat{Z}_k^{root}(L) + i\,(c_k C)^{-1} \tan\left(\frac{\omega_k L}{c_k}\right)}{1 + i c_k C \tan\left(\frac{\omega_k L}{c_k}\right) \hat{Z}_k^{root}(L)} \\ &= \lim_{k\to\infty} \frac{1}{c_k C} = \sqrt{\frac{\rho}{A_0 C}}\end{aligned}$$

Since ρ, the density of blood, is nonzero, Z is not integrable by the Riemann-Lebesgue Lemma.

□

Theorem 3.2.1 implies that the standard numerical implementation of the structured tree condition involves numerically approximating an integral which does not exist. To address this issue, we introduce a new numerical implementation that does not use the convolution theorem. To begin, we consider the Fourier series for the pressure at time $t = n\Delta t$:

$$P(L, n\Delta t) = \sum_{k=-\infty}^{\infty} \hat{P}_k(L) e^{i\omega_k n\Delta t} = \sum_{k=-\infty}^{\infty} \hat{Z}_k \hat{Q}_k(L) e^{i\omega_k n\Delta t}, \tag{3.23}$$

We seek an equation relating $P(L, n\Delta t)$ and $Q(L, n\Delta t)$. To obtain such an equation, we propose approximating the infinite series in (3.23) by an N-term partial sum and $\hat{Q}_k(L)$ by a Discrete Fourier Transform of the values $\{Q_M^{(n-N+1)}, ..., Q_M^{(n)}\}$. This approximation yields the following condition (without any loss of generality, we have taken N to be odd):

$$P_M^{(n)} = \sum_{k=-\frac{N-1}{2}}^{\frac{N-1}{2}} \hat{Z}_k \tilde{Q}_k^{(N)} e^{i\omega_k n\Delta t} \tag{3.24}$$

where $\tilde{Q}_k^{(N)}$ is the approximation of $\hat{Q}_k$ computed by DFT. Specifically,

$$\tilde{Q}_k^{(N)} \triangleq \frac{1}{N} \sum_{j=0}^{N-1} Q_M^{(n-j)} e^{-i\omega_k (n-j)\Delta t} \approx \frac{1}{T} \int_{t-T}^{t} Q(\tau) e^{-i\omega_k \tau} d\tau \tag{3.25}$$

We now show that as $N \to \infty$, the numerical approximation in (3.24) converges to the exact Fourier Series of P in (3.23). In the following proof we make use of the following relationship between the true Fourier coefficients of a function and approximations computed by DFT:

Discrete Poisson Summation Formula [14]. *If Q has a pointwise convergent Fourier series representation, then the exact Fourier coefficients of Q, denoted $\hat{Q}_k$, and the approximate Fourier coefficients of Q computed by a DFT of N values of Q, denoted $\hat{Q}_k^{(N)}$, are related by* *the following equality:*

$$\hat{Q}_k^{(N)} = \hat{Q}_k + \sum_{m=1}^{\infty} \left(\hat{Q}_{k+mN} + \hat{Q}_{k-mN} \right)$$

Additionally, we make use of the following lemma stating sufficient conditions for the absolute summability of a function's Fourier Series.

Lemma 3.2.1. *If f is a periodic function on $[0,T]$, and $f'(t)$ is continuous on $[0,T]$, then the Fourier Series for f is absolutely summable, that is,*

$$\sum_{k=-\infty}^{\infty} |\hat{f}_k| < \infty$$

Proof. Let $\hat{f}_k$ and $\widehat{f'_k}$ denote the kth respective Fourier coefficients of $f(t)$ and $f'(t)$. These coefficients are related in the following way:

$$\widehat{f'_k} = \frac{1}{T} \int_0^T f'(t) e^{-i\omega_k t} dt = i\omega_k \widehat{f_k}$$

In the above we have integrated by parts and made use of the periodicity of $f(t)$. The Cauchy-Schwarz inequality then gives the desired result:

$$\sum_{k=-\infty}^{\infty} |\widehat{f_k}| \leq \sqrt{\sum_{k=-\infty}^{\infty} \left(\frac{1}{\omega_k} \right)^2 \sum_{k=-\infty}^{\infty} \omega_k^2 |\widehat{f_k}|^2} = C||f'||_{L^2[0,T]}$$

where $C < \infty$ and $||f'||_{L^2[0,T]} < \infty$ since $f'(t)$ is continuous. □

We now show that the discrepancy between (3.23) and (3.24), denoted E_N, converges to 0 as $N \to \infty$.

Theorem 3.2.2. *For any T-periodic function $Q \in C^1[0,T]$, the approximation in (3.24) is an asymptotically valid approximation of (3.23) as $N \to \infty$. Specifically,*

$$\lim_{N \to \infty} \sum_{k=-\frac{N-1}{2}}^{\frac{N-1}{2}} \hat{Z}_k \tilde{Q}_k^{(N)} e^{i\omega_k n \Delta t} = \sum_{k=-\infty}^{\infty} \hat{Z}_k \hat{Q}_k e^{i\omega_k n \Delta t},$$

Proof.

$$\begin{aligned}
E_N &= \left| \sum_{k=-\infty}^{\infty} \hat{Q}_k \hat{Z}_k e^{i\omega_k n \Delta t} - \sum_{k=-\frac{N-1}{2}}^{\frac{N-1}{2}} \tilde{Q}_k^{(N)} \hat{Z}_k e^{i\omega_k n \Delta t} \right| \\
&\leq \left| \sum_{|k|>(N-1)/2} \hat{Q}_k \hat{Z}_k e^{i\omega_k n \Delta t} \right| + \left| \sum_{k=-\frac{N-1}{2}}^{\frac{N-1}{2}} (\hat{Q}_k - \tilde{Q}_k) \hat{Z}_k e^{i\omega_k n \Delta t} \right| \\
&\leq \sup_{k\in\mathbb{Z}} |\hat{Z}_k| \left(\sum_{|k|>\frac{N-1}{2}} \hat{Q}_k + \sum_{k=-\frac{N-1}{2}}^{\frac{N-1}{2}} \sum_{m=1}^{\infty} |\hat{Q}_{k+mN}| + |\hat{Q}_{k-mN}| \right) \\
&= 2 \sup_{k\in\mathbb{Z}} |\hat{Z}_k| \sum_{|k|>\frac{N-1}{2}} |\hat{Q}_k|
\end{aligned}$$

As shown in Theorem 3.2.1, $\hat{Z}_k$ converges to a finite limit as $|k| \to \infty$. This means that the sequence $\{\hat{Z}_k\}_{k\in\mathbb{Z}}$ is bounded. Since Q is T-periodic and in $C^1[0,T]$, $\{\hat{Q}_k\} \in \ell^1$ by Lemma 3.2.1. This means that

$$\lim_{N\to\infty} \sum_{|k|>\frac{N-1}{2}} \left|\hat{Q}_k\right| = 0$$

Therefore $\lim_{N\to\infty} E_N = 0$ and the proof is complete. □

We now simplify the numerical approximation in (3.24)

$$\begin{aligned}
\sum_{k=-\frac{N-1}{2}}^{\frac{N-1}{2}} \hat{Z}_k \tilde{Q}_k^{(N)} e^{i\omega_k n \Delta t} &= \sum_{k=-\frac{N-1}{2}}^{\frac{N-1}{2}} \hat{Z}_k \left(\frac{1}{N} \sum_{j=0}^{N-1} Q_M^{(n-j)} e^{-i\omega_k (n-j)\Delta t} \right) e^{i\omega_k n \Delta t} \\
&= \frac{\Delta t}{T} \sum_{j=0}^{N-1} Q_M^{(n-j)} \sum_{k=-\frac{N-1}{2}}^{\frac{N-1}{2}} \hat{Z}_k e^{i\omega_k j \Delta t} \\
&= \frac{\Delta t}{T} \sum_{j-0}^{N-1} Q_M^{(n-j)} Z^{(j)}
\end{aligned}$$

This is identical to (3.22), which is the equation obtained when one follows the implementation procedure suggested in [64], namely, approximating the convolution integral in (3.21) by a composite right-hand rectangle rule and approximating Z by computing the inverse DFT of N values of $\hat{Z}_k$. Therefore, Theorem 3.2.2 transitively implies that this implementation proposed by Olufsen et. al. in [64] is valid.

In summary, the results in this section suggest that the original implementation suggested by Olufsen et. al. in [64] is valid. However, the interpretation of "discretizing the integral" in (3.21) is both incorrect and dangerous. One potential danger is that if one uses a composite Simpson's rule instead than the composite right-hand rule, one will obtain an answer that differs substantially from the result obtained from the composite right-hand rectangle rule. Furthermore, as the grid is refined, the numerical results using Simpson's rule will even *converge to an incorrect answer*. To illustrate this issue, we consider the simple example where $\hat{Z}_k = R$ for all $k \in \mathbb{Z}$, where R is a constant. This means that $Z(t) = R\delta(t)$ where $\delta(t)$ is the Dirac delta function. The convolution integral in (3.21) is thus well defined in a weak sense:

$$\int_{t-T}^{t} Z(\tau)Q(t-\tau)d\tau = RQ(t) \tag{3.26}$$

Approximating Z by inverse Discrete Fourier Transform gives

$$\begin{aligned} Z_n &= \sum_{k=-\frac{N-1}{2}}^{\frac{N-1}{2}} R\omega_N^{kn} \\ &= R\left(\sum_{k=0}^{N-1} \omega_N^{kn}\right) \\ &= NR\delta_n \end{aligned}$$

where $\delta_n = 1$ if $n = 0$ and $\delta_n = 0$ otherwise, and $\omega_N = e^{i2\pi/N}$. Approximating the convolution integral in (3.26) by a composite right hand rule gives

$$\frac{1}{T}\int_{t-T}^{t} Z(\tau)Q(t-\tau)d\tau \approx N\frac{\Delta t}{T}\sum_{k=0}^{N-1} R\delta_k Q(t-k\Delta t) = RQ(t)$$

in the above we have used the fact that $\Delta t = T/N$. Thus, we have shown that in the case where $\hat{Z}_k$ is constant, approximating Z by inverse Discrete Fourier Transform and the convolution integral by a composite right hand rule yields the correct result *exactly* regardless of mesh size. Unfortunately, this is no longer true if one uses the composite Simpson's rule [34]:

$$\int_a^b f(t)dt \approx \frac{\Delta t}{3}\left(f(t_0) + 4f(t_1) + 2f(t_2) + 4f(t_3) + 2f(t_4) + \cdots + 4f_{t_{n-1}} + f(t_n)\right)$$

where $t_k = a + k\Delta t$, $\Delta t = (b-a)/n$. Applying the composite Simpson's rule to (3.26) with

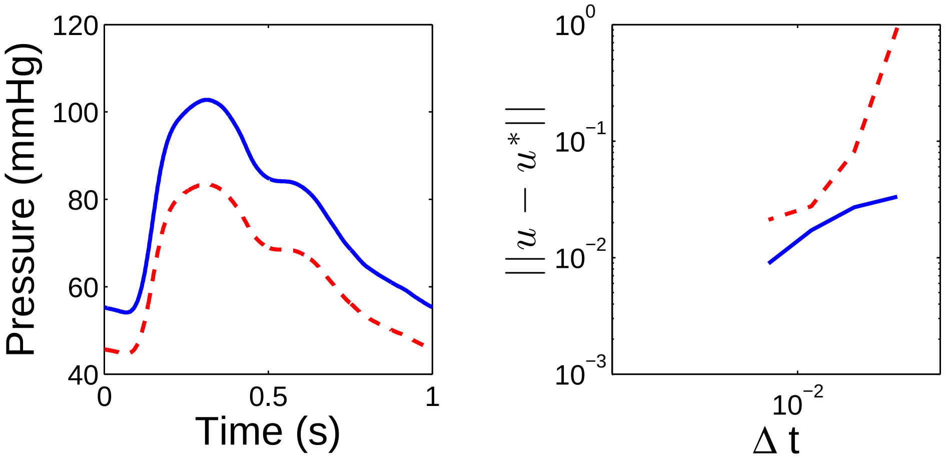

Figure 3.3: Left: Pressure curves obtained from a numerical simulation of the Circle of Willis using a composite right hand rule (blue) and composite Simpson's rule (red) to discretize the convolution integral in (3.21). Right: Results of a grid refinement study, indicating convergence of both methods as $\Delta t \to 0$. u^* indicates the limiting solution as $\Delta t \to 0$.

inverse DFT approximation of Z gives:

$$\frac{1}{T}\int_{t-T}^{t} Z(\tau)Q(\tau)d\tau \approx \frac{2}{3}RQ(t) \tag{3.27}$$

again this approximation is independent of the choice of Δt, but it is *wrong*. Specifically, the composite Simpson's rule with inverse DFT approximation of Z gives a result that is 2/3 times the correct answer. This phenomena persists when the structured tree is implemented in numerical simulations of blood flow in the Circle of Willis. Figure 3.3 displays the results of two grid refinement studies who differ only in their discretization of the convolution integral (3.21). The results for the pressure obtained from discretizing the convolution integral using composite Simpson's rule are markedly different from the correct results obtained from the use of the composite right hand rule. Disturbingly, results from using Simpson's rule converge to this incorrect answer as $\Delta t \to 0$.

In summary, the implementation (3.22) originally advocated by Olufsen et. al. in [64] is valid, but its incorrect use of the convolution theorem is dangerous and misleading. To properly implement the structured tree, one must take care to implement (3.22) precisely as written. Since the integral in (3.21) does not exist in a classical sense, seemingly innocent deviations from (3.22) can yield incorrect results with no apparent signs of failure.

3.2.2 Convergence of Solution to Periodic Regime

It is not obvious in what sense the non-periodic numerical approximations generated by a serial time-stepping method constitute a solution to the periodic IBVP. The claim made by Olufsen et. al. in [64] is that as $t \to \infty$, the solution converges to a periodic regime. This periodic limit should be taken to be the solution of the periodic IBVP. We now numerically investigate the claim that the solution becomes periodic. To do so, we rewrite the solution $\vec{u} = [A, Q]$ "modulo T" into a sequence of grid functions $\vec{u}_k(x_m, t_n) \triangleq \vec{u}(x_m, t_n + kT)$. We also define

$$\Delta_k \vec{u} \triangleq \max_{n=1,\dots N, x_m \in \Omega} ||\vec{u}_k(x_m, t_n) - \vec{u}_{k-1}(x_m, t_n)||_\infty,$$

where N is the number of time steps per period and Ω is the set of all spatial points in the network. The components of $\vec{u}_k - \vec{u}_{k-1}$ are scaled by their temporal averages to make $\Delta_k \vec{u}$ a measure of the relative change in the solution from one period to the next. In the case of the structured tree boundary condition, the issue of convergence is complicated by the fact that in addition to providing initial data for all unknowns, one must also prescribe an initial history of the flowrate Q for $t \in [-T, 0]$ at the end of each outlet vessel, see (3.22). To examine well-posedness of the structured tree boundary condition, we examine the following:

1. Does the solution converge to a periodic regime as $t \to \infty$? That is, does $\lim_{k\to\infty} \Delta_k \vec{u} = 0$?
2. Is this limiting periodic regime independent of the initial history of the flowrate one chooses to prescribe?

To test the dependence of the solution on the initial history of Q, we solve the problem with 1,000 randomly generated sets of initial histories of Q for the outflow vessels of the Circle of Willis. We use constant initial histories with values of Q between 0 cm^3/s and 10 cm^3/s. With each choice of initial history, the solution converged to the *same* limiting periodic regime to a tolerance of $\Delta_k \vec{u} < 10^{-3}$ in six periods or less. This confirms convergence to a periodic regime and negligible dependence of the choice of initial history. An example plot of the convergence of $\Delta_k \vec{u}$ is displayed in Figure 3.4.

For the nonlinear problem, we must resort to this sort of numerical investigation of the convergence of the solution to a periodic regime. However, the analysis for the linear problem is amenable to analytical investigation. Discretization of the linearized equations (3.12) and

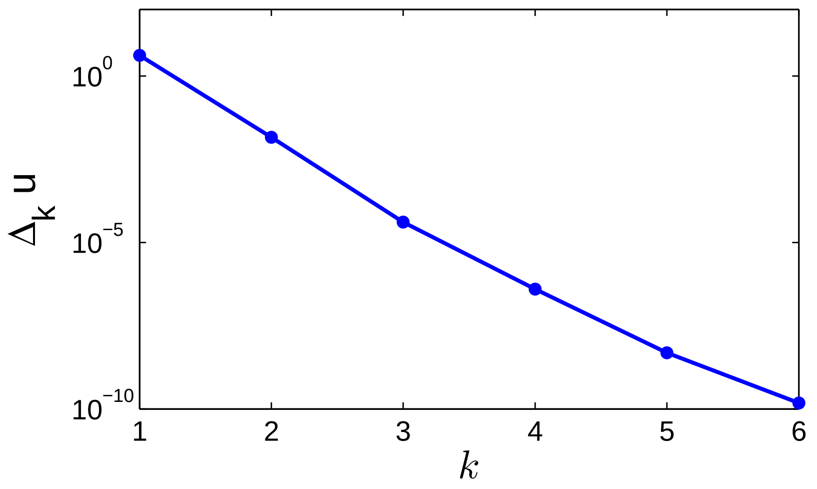

Figure 3.4: Convergence of $\Delta_k \vec{u}$ to 0, indicating convergence of the numerical solution to a periodic regime.

(3.12) using Chebyshev collocation in space and backward Euler time integration yields:

$$\left[\begin{array}{c|c} I & \frac{\Delta t}{C} D \\ \hline \Delta t \frac{A_0}{\rho} D & (1+\delta \Delta t)\, I \end{array}\right] \left[\begin{array}{c} \vec{P}^{n+1} \\ \hline \vec{Q}^{n+1} \end{array}\right] = \left[\begin{array}{c} \vec{P}^{n} \\ \hline \vec{Q}^{n} \end{array}\right]$$

where $\vec{P}^n = [P_0^n, ..., P_M^n]^T$ with P_k^n denoting the approximation of $P(n\Delta t, x_m)$. Here Δt is the time step size and x_m is the mth Chebyshev node. D is the $(M+1) \times (M+1)$ Chebyshev differentiation matrix. To account for the inflow boundary condition we replace equation $M+1$ by $Q_0^{n+1} = q_{n+1}$, where $q_{n+1(\mathrm{mod} N_T)}$ is the imposed periodic flowrate at time $(n+1)\Delta t$. N_T is the number of time steps per period ($N_T = T/\Delta t$). To account for the structured tree boundary condition, we replace equation $M+2$ by (3.22), which requires

$$P_M^{n+1} = \sum_{k=0}^{N_T-1} Z_k Q_M^{n+1-k}.$$

where $\{Z_k\}$ are the values of the inverse discrete Fourier transform of values of $\hat{Z}_k$. This yields

$$A \left[\begin{array}{c} \vec{P}^{n+1} \\ \hline \vec{Q}^{n+1} \end{array}\right] = \left(\tilde{I} + B_1\right) \left[\begin{array}{c} \vec{P}^{n} \\ \hline \vec{Q}^{n} \end{array}\right] + \sum_{k=2}^{N_T-1} B_k \left[\begin{array}{c} \vec{P}^{n+1-k} \\ \hline \vec{Q}^{n+1-k} \end{array}\right]$$

$\widetilde{I}$ is the $2(M+1)\times 2(M+1)$ identity matrix altered so $\widetilde{I}_{M+1,M+1} = \widetilde{I}_{M+2,M+2} = 0$. A and B_k are defined as follows:

$$A = \left[\begin{array}{c|cccc} & \multicolumn{4}{c}{\widetilde{D}^{(M+1)}} \\ I_{M+1} & & & & \\ & 0 & \cdots & 0 & -Z_0 \\ \hline 0 \ \cdots \ 0 & 1 & 0 & \cdots & 0 \\ & 0 & & & \\ \Delta\frac{A_0}{\rho}\widetilde{D}^{(1)} & \vdots & \multicolumn{3}{c}{(1+\delta\Delta t)I_M} \\ & 0 & & & \end{array}\right], \qquad B_k = \left[\begin{array}{c|cccc} & \multicolumn{4}{c}{0} \\ 0 & & & & \\ & 0 & \cdots & 0 & Z_k \\ \hline 0 & \multicolumn{4}{c}{0} \\ & & & & \end{array}\right].$$

in the above $\widetilde{D}^{(k)}$ is the Chebyshev differentiation matrix with the kth row deleted. We now express the map of the solution from period k to period $k+1$ as a linear fixed point iteration:

$$R\begin{bmatrix} \vec{P}^{(k+1)N_T} \\ \vec{Q}^{(k+1)N_T} \\ \vec{P}^{(k+1)N_T+1} \\ \vec{Q}^{(k+1)N_T+1} \\ \vdots \\ \vec{P}^{(k+2)N_T-1} \\ \vec{Q}^{(k+2)N_T-1} \end{bmatrix} = S\begin{bmatrix} \vec{P}^{kN_T} \\ \vec{Q}^{kN_T} \\ \vec{P}^{kN_T+1} \\ \vec{Q}^{kN_T+1} \\ \vdots \\ \vec{P}^{(k+1)N_T-1} \\ \vec{Q}^{(k+1)N_T-1} \end{bmatrix} + \begin{bmatrix} \vec{q}^{\,0} \\ \vec{q}^{\,1} \\ \vdots \\ \vec{q}^{\,N_T-1} \end{bmatrix} \tag{3.28}$$

where R is a block Toeplitz, block lower triangular matrix where the individual blocks of R are as follows:

$$R_{ij} = \begin{cases} A & i = j \\ -(\widetilde{I} + B_1) & i - j = 1 \\ -B_{i-j} & i - j < 1 \end{cases}$$

S is block Toeplitz, block strictly upper triangular whose individual blocks are as follows:

$$S_{ij} = \begin{cases} B_{N_T+i-j} & i < j, (i,j) \neq (1, N_T) \\ -(\widetilde{I} + B_1) & (i,j) = (1, N_T) \\ 0 & i \geq j \end{cases}$$

To analyze the convergence of the numerical solution to a periodic regime, we compute the spectral radius of $R^{-1}S$. The reason for this is that a necessary and sufficient condition for convergence of this fixed point iteration for all $\vec{q}^{\,k}$ is for the spectral radius of $R^{-1}S$ to be strictly less than 1 (see Theorem 1.3.1 in [46]). R is invertible as long as A is invertible, and numerical evidence indicates that this is the case. The inverse of R was computed semi-analytically using a numerically computed inverse of A. The spectral radius was computed using MATLAB's eig command. To verify this computation, the spectral radius was computed using two other approaches. First, the spectral radius was also computed for a numerically computed $R^{-1}S$ (using MATLAB's backslash command). Secondly, the spectral radius was computed through MATLAB's eig using the option for generalized eigenvalue problems of the form $Av = \lambda Bv$. The spectral radii computed via each of these three methods agreed to 10 digits in all cases. We computed the spectral radius for each of the outflowing vessels of the Circle of Willis, and the results are displayed in Table 4.1. In all cases, the spectral radius is substantially less than 1, indicating convergence of the numerical solution to a periodic regime.

Table 3.2: Spectral radii of $R^{-1}S$ in (3.28) for the right and left Posterior Cerebral Arteries (PCA), Middle Cerebral Arteries (MCA), and Anterior Cerebral Arteries (ACA).

Vessel	R PCA	L PCA	R MCA	L MCA	R ACA	L ACA
Periodic Spec. Rad.	3.7e-03	4.0e-03	8.7e-03	9.1e-03	6.7e-02	1.2e-03

3.3 Sensitivity to Minimum Radius

In [62], Olufsen performs numerical sensitivity studies with respect to the minimum radius, r_{min}, and concluded that the structured tree boundary condition is highly sensitive to this parameter. We now provide an analytical explanation of this fact by analyzing the DC component of the root impedance, $\hat{Z}_0^{\mathrm{root}}(0)$. Consider first that instead of terminating according to a minimum radius threshold, the tree terminates after a specific number of generations. An induction argument shows that the DC component of the root impedance of this equi-generational tree, with N generations, can be expressed as a truncated geometric series:

Lemma 3.3.1. *For an equi-generational tree with N generations*

$$\hat{Z}_0^{root}(0) = \frac{8\mu\lambda}{\pi r_{root}^3} \sum_{i=0}^{N} \left(\frac{1}{\alpha^3 + \beta^3} \right)^i \tag{3.29}$$

Proof. The result follows from a straightforward induction argument. For a tree with a single vessel (N=0), the DC impedance relation (3.7) implies that

$$\hat{Z}_0^{\text{root}}(0) = \frac{8\mu\lambda}{\pi r_{\text{root}}^3},$$

meaning that (3.29) holds for $N = 0$. Now suppose that (3.29) holds for any tree with N generations. If d_1 and d_2 denote the two daughters of the root vessel of a tree with $N + 1$ generations, then the induction hypothesis implies

$$\begin{aligned}
\hat{Z}_0^{d_1}(0) &= \frac{8\mu\lambda}{\pi(\alpha r_{\text{root}})^3} \sum_{i=0}^{N} \left(\frac{1}{\alpha^3 + \beta^3} \right)^i \\
\hat{Z}_0^{d_2}(0) &= \frac{8\mu\lambda}{\pi(\beta r_{\text{root}})^3} \sum_{i=0}^{N} \left(\frac{1}{\alpha^3 + \beta^3} \right)^i
\end{aligned}$$

Applying the junction relation (3.8) and the single vessel impedance relation (3.7), we have

$$\begin{aligned}
\hat{Z}_0^{\text{root}}(0) &= \frac{8\mu\lambda}{\pi r_{\text{root}}^3} + \frac{\hat{Z}_0^{\text{d1}}(0)\hat{Z}_0^{\text{d2}}(0)}{\hat{Z}_0^{\text{d1}}(0) + \hat{Z}_0^{\text{d2}}(0)} \\
&= \frac{8\mu\lambda}{\pi r_{\text{root}}^3} + \frac{1/(\alpha^3\beta^3)}{\frac{1}{\alpha^3} + \frac{1}{\beta^3}} \frac{8\mu\lambda}{\pi r_{\text{root}}^3} \sum_{i=0}^{N} \left(\frac{1}{\alpha^3 + \beta^3} \right)^i \\
&= \frac{8\mu\lambda}{\pi r_{\text{root}}^3} \sum_{i=0}^{N+1} \left(\frac{1}{\alpha^3 + \beta^3} \right)^i
\end{aligned}$$

By induction, the formula (3.29) holds for all $N \geq 0$. $\square$

We now use Lemma 3.3.1 to prove a result for the structured tree with the minimum radius termination criterion described in Section 3.1.1.

Theorem 3.3.1. *As $r_{min} \to 0$, $\hat{Z}_0^{root}(0)$ converges to a finite limit if and only if $\xi > 3$, where ξ, defined in Section 3.1.1, is the unique real number satisfying*

$$r_{pa}^{\xi} = r_{d1}^{\xi} + r_{d2}^{\xi}$$

Proof. To begin, we show that adding a branch to a leaf of a tree increases the DC component of the impedance at the root. To compute the DC component of the root impedance, one successively applies the following two functions repeatedly:

$$\hat{Z}_0(0) = \hat{Z}_0(L) + \frac{8\mu\lambda}{\pi r_0^3} \tag{3.30}$$

$$\hat{Z}_0^{(pa)}(L) = \frac{\hat{Z}_0^{(d1)}(0) \cdot \hat{Z}_0^{(d2)}(0)}{\hat{Z}_0^{(d1)}(0) + \hat{Z}_0^{(d2)}(0)} \tag{3.31}$$

The first of the two above functions is clearly an increasing function of $\hat{Z}_0(L)$. Elementary calculus shows that the second function is increasing with respect to $\hat{Z}_0^{(d1)}(0)$ and $\hat{Z}_0^{(d2)}(0)$.

For a leaf vessel, $\hat{Z}_0^{\text{leaf}}(L) = \hat{Z}_{term} = 0$. If a branch is added to the end of this leaf vessel, this changes $\hat{Z}_0(L)$ for that vessel. With the branch added,

$$\begin{aligned}
\hat{Z}_0^{\text{leaf}}(L) &= \frac{\hat{Z}_0^{(d1)}(0) \cdot \hat{Z}_0^{(d2)}(0)}{\hat{Z}_0^{(d1)}(0) + \hat{Z}_0^{(d2)}(0)} \\
&= \frac{\dfrac{8\mu\lambda}{\pi\alpha^3 r_{leaf}^3} \cdot \dfrac{8\mu\lambda}{\pi\beta^3 r_{leaf}^3}}{\dfrac{8\mu\lambda}{\pi\alpha r_{leaf}^3} + \dfrac{8\mu\lambda}{\pi\beta^3 r_{leaf}^3}} \\
&= \frac{1}{\alpha^3 + \beta^3} \frac{8\mu\lambda}{\pi r_{leaf}^3} > 0.
\end{aligned}$$

Thus, adding a branch to a leaf vessel increases $\hat{Z}_0^{\text{leaf}}(L)$ from 0 to a positive number. Since the DC component of the root impedance, $\hat{Z}_0^{\text{root}}(0)$, is an increasing function of $\hat{Z}_0^{\text{leaf}}(L)$, we have that adding a branch to a leaf vessel increases the DC component of the root impedance.

This allows us to use Lemma 3.3.1 to create upper and lower bounds for the DC component of the root impedance

$$\frac{8\mu\lambda}{\pi r_{\text{root}}^3} \sum_{i=0}^{N_1} \left(\frac{1}{\alpha^3 + \beta^3} \right)^i \leq \hat{Z}_0^{\text{root}}(0) \leq \frac{8\mu\lambda}{\pi r_{\text{root}}^3} \sum_{i=0}^{N_2} \left(\frac{1}{\alpha^3 + \beta^3} \right)^i, \tag{3.32}$$

where N_1 and N_2 are the smallest and largest generation terminal vessels, respectively. As $r_{min} \to 0$, $N_1 \to \infty$. Thus (3.32) implies that as $r_{min} \to 0$, $\hat{Z}_0^{\text{root}}(0)$ behaves like a geometric series which converges only when the quantity $\alpha^3 + \beta^3$ is larger than 1. By definition of the

ξ, α, and β, we have $\alpha^\xi + \beta^\xi = 1$ and thus

$$\frac{1}{\alpha^3 + \beta^3} < \frac{1}{\alpha^\xi + \beta^\xi} = 1,$$

for $\xi > 3$. Therefore, $\hat{Z}_0^{\text{root}}(0)$ converges as $r_{min} \to 0$ if and only if $\xi > 3$. □

Table 3.3: Published values for the scaling parameter ξ.

$\boldsymbol{\xi}$	**samples**	**sd**	**notes**	**source**
2.66	1533	0.081	$r \geq 100\mu m$	Suwa et al. [84]
2.71	1455	0.092	$r < 100\mu m$	Suwa et al. [84]
2.9	157	0.7	Measurements from ICA, ACA, MCA	Rossitti et al. [74]
3.0	N/A	N/A	Theoretical optimum, laminar flow	Murray [58]
2.33	N/A	N/A	Theoretical optimum, turbulent flow	Uylings [90]
2.76	N/A	N/A		Olufsen [63]

Physiological and theoretical values of ξ from the literature are given in Table 3.3. In [58], Murray develops an expression for the work required to operate a section of vessel, and later calculates that a value of $\xi = 3$ minimizes this work [57]. Uylings [90] generalizes Murray's results to include the possibility of non-laminar flow, leading to $\xi = 2.33$ for turbulent flow and agreeing with Murray's $\xi = 3$ flow laminar flow. Olufsen proposes $\xi = 2.76$ [63]. Additionally, Suwa et al. [84] and Rossitti et al. [74] have obtained estimated values of ξ by direct measurement. In Table 3.3, a "sample" refers to a triplet of values (r_p, r_{d1}, r_{d2}) measured at a single bifurcation.

While this collection of measured and theoretically determined values for ξ does exhibit some variation, all of these values share one important characteristic: they are all no bigger than 3. Thus, using *any* of these values will result in the average root impedance being highly sensitive to the choice of r_{min} for small values of r_{min}, since the process is akin to truncating a divergent series.

Figure 3.5 shows numerically computed solution curves at the end of the right middle cerebral artery in simulations of the Circle of Willis using values of r_{min} equal to $20, 40, 60, 80$, and $100\mu m$. The details of the numerical simulation are given in Appendix A. The above analytical result shows that one component of the boundary condition, $\hat{Z}_0^{\text{root}}(0)$, is sensitive to r_{min}; these numerical results confirm that this sensitivity to r_{min} is also present in the solution itself. For instance, merely changing r_{min} from $40\mu m$ to $20\mu m$ changes the average pressure at the end of the right middle cerebral artery from 160 mmHg to 267 mmHg.

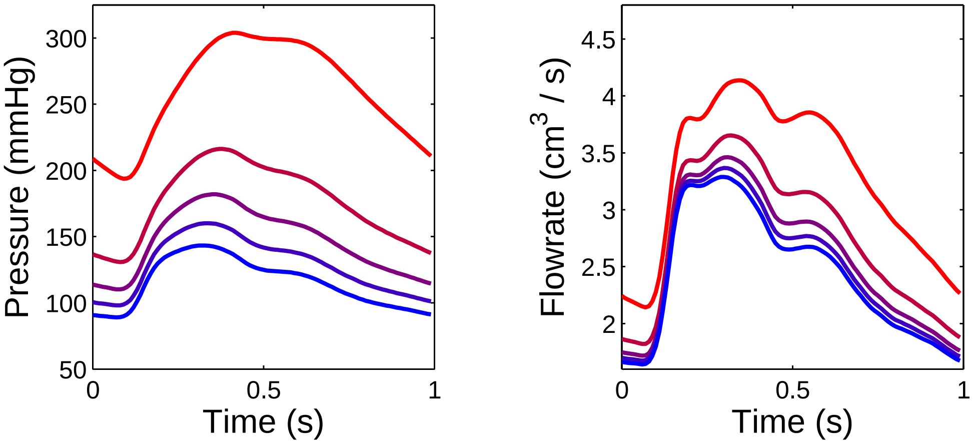

Figure 3.5: Pressure and flowrate curves using $r_{min} = 20, 40, 60, 80,$ and $100\mu m$. The red (top) curves correspond to $r_{min} = 20\mu m$ and the blue (bottom) curves correspond to $r_{min} = 100\mu m$.

Chapter 4

The Generalized Structured Tree Boundary Condition

In Chapter 3, we outlined Olufsen's derivation of the structured tree boundary condition. This boundary condition has a number of advantages over its competitors and has been used with success in [9, 21, 51, 62, 63, 64, 82, 88]. However, the structured tree boundary condition suffers from a major shortcoming: its assumption of strict flow periodicity does not hold in many physiologically relevant conditions. This limitation, which has also been noted in [35, 95], means that the structured tree may not be used to simulate conditions such as exercise, cardiac arrhythmia, or sudden vessel occlusion.

Here we develop a generalized structured tree boundary condition that does not involve a periodicity assumption and is thus applicable to all flow regimes. We do so by replacing the Fourier Series approach used in Chapter 3 with a Laplace transform approach. Furthermore, in Section 4.2 we describe how this condition may be implemented *without* performing a perilous numerical inverse Laplace transform. In Section 4.4.1, we show that this boundary condition reduces to the original condition for periodic problems (up to differences in numerical implementation). We then implement this boundary condition to simulate a variety of non-periodic phenomena in the Circle of Willis.

Although the original structured tree is derived under the assumption of temporal periodicity, for reasons discussed in Section 3.2 its numerical implementation in no way enforces temporal periodicity. Thus, it is possible to use the original structured tree to model non-periodic flows, even in the absence of any justification for doing so. In Section 4.5, we provide such justification by showing that the numerical implementation of the original structured tree condition may be viewed as a rough numerical approximation of the generalized structured tree condition. This fact, which is confirmed by numerical experiments in Section 4.4.2, implies that it may be appropriate to use the unaltered original structured tree condition to model non-periodic phenomena.

4.1 Derivation

4.1.1 Single vessel equations

To begin, we consider the linearized, cross-sectionally averaged Navier-Stokes Equations (3.12), (3.13)

$$\begin{aligned} C\,\partial_t P + \partial_x Q &= 0 \\ \partial_t Q + \frac{A_0}{\rho}\,\partial_x P &= -2\pi(\gamma+2)\,\frac{\mu}{\rho}\,\frac{Q}{A_0} \end{aligned}$$

Instead of expressing the above unknowns in terms of their Fourier coefficients, as done in the derivation of the original structured tree condition [22, 62, 63, 64, 82], we take the Laplace transform of the system with respect to time. Assuming zero initial pressure and flow, we obtain

$$Cs\,\widehat{P} + \partial_x \hat{Q} = 0, \tag{4.1}$$

$$(s+\delta)\hat{Q} + \frac{A_0}{\rho}\,\partial_x \hat{P} = 0, \tag{4.2}$$

where $\hat{P} = \mathcal{L}(P)$, $\hat{Q} = \mathcal{L}(Q)$ and $\delta = 2\mu(\gamma+2)/(\rho r_0^2)$. The solutions to (4.1) and (4.2) evaluated at $x = 0$ are

$$\begin{aligned} \hat{Q}(0,s) &= s d_s C \hat{P}(s,L)\sinh\left(\frac{L}{d_s}\right) + \hat{Q}(s,L)\cosh\left(\frac{L}{d_s}\right), \\ \hat{P}(0,s) &= \hat{P}(s,L)\cosh\left(\frac{L}{d_s}\right) + \frac{1}{s d_s C}\hat{Q}(s,L)\sinh\left(\frac{L}{d_s}\right), \end{aligned}$$

with $d_s^2 = A_0/[C\rho s(s+\delta)]$. Defining the impedance through its Laplace transform

$$\hat{Z}(x,s) = \frac{\hat{P}(x,s)}{\hat{Q}(x,s)}, \tag{4.3}$$

yields, for $s \neq 0$,

$$\hat{Z}(0,s) = \frac{\hat{Z}(L,s) + \frac{1}{s d_s C}\tanh L/d_s}{s d_s C\,\hat{Z}(L,s)\tanh L/d_s + 1}. \tag{4.4}$$

The above equation has a removable singularity at $s = 0$, which we use to define $Z(0,0)$ as a function of $Z(L,0)$:

$$Z(0,0) \triangleq \lim_{s \to 0} Z(0,s) = Z(L,0) + \frac{2(\gamma+2)\mu\lambda}{\pi r_0^3} \tag{4.5}$$

The above formula links the impedance at the beginning of the vessel to the impedance at its end. For s restricted to the imaginary axis, i.e., $s = i\omega$, $\omega \in \mathbb{R}$, (4.4) corresponds to the impedance found in Section 3.1.3 (see relation (3.16)), where Fourier series were used.

4.1.2 Extension to structured vascular trees

As was done for the periodic structured tree, we assume that the vascular trees share the following structure:

1. Vessels end by bifurcating into two daughter vessels; vessels with radii smaller than a minimal value $r_{min} > 0$, terminate, i.e., they do not bifurcate.
2. There are two parameters α and β where $0 < \beta < \alpha < 1$ and for any parent/daughter vessels
$$r_{d1} = \alpha r_{pa} \text{ and } r_{d2} = \beta r_{pa}$$
where r_{pa}, r_{d1} and r_{d2} are the radii of the parent/daughter vessels respectively.
3. There is a positive parameter λ such that for any vessel in the tree
$$\lambda = r/L.$$

We follow [22, 62, 63, 64, 82] to compute the impedance of the entire tree by noting that (4.3), together with continuity of pressure and conservation of mass at each junction, leads to

$$\frac{1}{\hat{Z}_{pa}(L,s)} = \frac{1}{\hat{Z}_{d1}(0,s)} + \frac{1}{\hat{Z}_{d2}(0,s)} \text{ for any } s. \tag{4.6}$$

The impedances at the ends ($x = L$) of all terminal vessels are assumed to share a common constant value $\hat{Z}_{term}$, which is usually set to $\hat{Z}_{term} = 0$ [22, 63, 64]. For any s, a value for the impedance of the root vessel is obtained by recursively applying relations (4.4) and (4.6).

4.1.3 Algorithm to compute the impedance

Sections 4.1.1 and 4.1.2 describe how to compute $\hat{Z}(s)$ for a structured tree. Here we describe a recursive algorithm for performing this task, which is analogous to the original algorithm proposed by Olufsen [62]. In the following, the function “singleVesselImp” denotes (4.4).

```
procedure IMPEDANCE
Input: $r$ - radius of vessel
Output: ZPA_0

    if $r < r_{min}$ then
        $ZPA\_L = Z_{term}$
    else
        $ZD1 = \text{IMPEDANCE}(\alpha \cdot r)$
        $ZD2 = \text{IMPEDANCE}(\beta \cdot r)$
        $ZPA\_L = ZD1 \cdot ZD2/(ZD1 + ZD2)$
    end if
    $ZPA\_0 = singleVesselImp(ZPA\_L)$
end procedure
```

The above algorithm is not optimal as it contains redundant evaluations of the impedance. For example, one will separately compute the impedance corresponding to $\alpha\beta r$ and $\beta\alpha r$ even though these values are the same. A more efficient approach, described in [64] and Appendix A of this dissertation, is to record previously computed values of the impedance to avoid repeating calculations.

4.2 Numerical Implementation

Using the construction described in Section 4.1, we compute the Laplace transform of the impedance corresponding to a given tree. To use this result as a boundary condition in a major vessel, we note that (4.3) implies

$$P(t) = \int_0^t Z(\tau)Q(t-\tau)\,d\tau, \tag{4.7}$$

where all quantities are evaluated at the end of the outflow vessel[1] and $Z = \mathcal{L}^{-1}(\hat{Z})$.

To evaluate (4.7), we use a convolution quadrature approach [48], which utilizes the values of the Laplace transform $\hat{Z} = \mathcal{L}(Z)$ rather than the values of Z. This allows us to avoid entirely the delicate numerical inversion of the Laplace transform [67] to go from $\hat{Z}$, computed in Section 4.1, to Z, which we cannot access directly. Furthermore, convolution quadrature methods are provably convergent even in the case when the inverse Laplace transform of the $\hat{Z}$ only exists in a weak sense [50].

---

[1] The end of the outflow vessel is the beginning ($x = 0$) of the root vessel of the tree. From here on and for the sake of simplicity, we omit explicit mention of the spatial variables.

4.2.1 Convolution quadrature

For the sake of completeness, the convolution quadrature method is summarized below in the present context. Applying Mellin's inversion formula, we obtain

$$Z(\tau) = \frac{1}{2\pi i} \lim_{T\to\infty} \int_{\nu-iT}^{\nu+iT} \hat{Z}(\lambda) e^{\lambda\tau}\, d\lambda, \tag{4.8}$$

where the integration is taken along the vertical line $Re(\lambda) = \nu$ with ν is greater than the real part of all singularities of $\hat{Z}$. An analysis of the locations of the singularities of $\hat{Z}$ is provided in Section 4.3. The convolution quadrature algorithm [48] consists of substituting (4.8) into (4.7),

$$P(t) = \frac{1}{2\pi i} \lim_{T\to\infty} \int_{\nu-iT}^{\nu+iT} \hat{Z}(\lambda)\, y(\lambda; t)\, d\lambda, \qquad y(\lambda; t) = \int_0^T e^{\lambda t} Q(t-\tau)\, d\tau \tag{4.9}$$

and observing that y is the unique solution to the initial value problem

$$y' = \lambda y + Q, \qquad y(0) = 0. \tag{4.10}$$

The next step in the convolution quadrature method is to apply a multistep method to (4.10) and to approximate $P(n\Delta t)$ by replacing y the integral (4.9) with

$$\sum_{j=0}^{k} \alpha_j y_{n+j-k} = \Delta t \sum_{j=0}^{k} \beta_j (\lambda y_{n+j-k} + Q((n+j-k)\Delta t)), \tag{4.11}$$

where Δt is the time step size and the parameters α_j and β_j $(j = 0, \ldots, k)$ are the coefficients of the chosen multistep method. Even after approximating y by a multistep method, it is challenging to directly evaluate the improper integral in (4.9) numerically. The remaining analysis, also from [48], recasts this integral into a more computationally appealing form.

Consider the formal expansions

$$\mathbb{Y}(\zeta) = \sum_{n=0}^{\infty} y_n \zeta^n \text{ and } \mathbb{Q}(\zeta) = \sum_{n=0}^{\infty} Q(n\Delta t)\zeta^n.$$

Multiplying (4.11) by ζ^n and summing yields

$$\mathbb{Y}(\zeta) = \left(\frac{\Xi(\zeta)}{\Delta t} - \lambda\right)^{-1} \mathbb{Q}(\zeta), \quad \text{where } \Xi(\zeta) = \frac{\alpha_0 \zeta^n + \cdots + \alpha_k}{\beta_0 \zeta^n + \cdots + \beta_k}. \tag{4.12}$$

Evaluating (4.9) at discrete times $n\Delta t$ ($n = 0, 1, \dots$), we consider an expansion of P similar to (4.12)

$$\begin{aligned}\sum_{n=0}^{\infty} P_n \zeta^n &= \frac{1}{2\pi i} \lim_{T\to\infty} \int_{\nu-iT}^{\nu+iT} \hat{Z}(\lambda) \mathbb{Y}(\zeta)\, d\lambda \\ &= \frac{1}{2\pi i} \lim_{T\to\infty} \int_{\nu-iT}^{\nu+iT} \hat{Z}(\lambda) \left(\frac{\Xi(\zeta)}{\Delta t} - \lambda\right)^{-1} \mathbb{Q}(\zeta)\, d\lambda.\end{aligned}$$

where P_n is the approximation of (4.9) obtained by approximating y by (4.11). Cauchy's integral formula leads to

$$\sum_{n=0}^{\infty} P_n \zeta^n = \hat{Z}\left(\frac{\Xi(\zeta)}{\Delta t}\right) \mathbb{Q}(\zeta). \tag{4.13}$$

We then expand $\hat{Z}$ as

$$\hat{Z}\left(\frac{\Xi(\zeta)}{\Delta t}\right) = \sum_{n=0}^{\infty} z_n \zeta^n, \qquad z_n = \frac{1}{2\pi i} \int_{|\zeta|=r} \hat{Z}\left(\frac{\Xi(\zeta)}{\Delta t}\right) \zeta^{-n-1}\, d\zeta, \tag{4.14}$$

so that (4.13) becomes

$$\sum_{n=0}^{\infty} P_n \zeta^n = \sum_{n=0}^{\infty} z_n \zeta^n \sum_{n=0}^{\infty} Q(n\Delta t) \zeta^n.$$

Equating the like powers of ζ, we approximate the pressure P by

$$P(n\Delta t) \approx P_n = \sum_{j=0}^{n} z_{n-j} Q(j\Delta t). \tag{4.15}$$

During a simulation, (4.15) is enforced at the end of each outflow vessel.

It remains to compute the weights z_n, $n = 0, \dots, N$, where N is the total number of time steps. Following [49], this can be efficiently done through a trapezoidal rule approximation of the Cauchy integral in (4.14). More precisely, we approximate z_n by

$$\tilde{z}_n = \frac{r^{-n}}{M} \sum_{m=0}^{M-1} \hat{Z}\left(\frac{\Xi(r\, e^{im2\pi/M})}{\Delta t}\right) e^{-inm2\pi/M}, \tag{4.16}$$

where M is the number of quadrature points.

The $\tilde{z}_n$'s can be computed simultaneously using FFT; this requires M evaluations of $\hat{Z}$ and $\mathcal{O}(M \log M)$ arithmetical operations. If $\hat{Z}$ is computed with an accuracy of ϵ, one may compute z_n, $n = 0, ..., N$ with accuracy $O(\sqrt{\epsilon})$ by choosing $M = N$ and $r^N = \sqrt{\epsilon}$ [49]. For safety, we typically take $M = 2N$. We take $\epsilon = 10^{-10}$, but nearly identical results were obtained for ϵ ranging from 10^{-6} to 10^{-13}. $\Xi(\zeta) = \zeta^2/2 - 2\zeta + 3/2$, which corresponds to the second order backward differentiation formula.

4.2.2 Impedance Implementation Algorithm

The algorithm for computing the impedance weights z_n with the convolution quadrature method is as follows.

```
procedure ImpedanceWeights
    Input:
        $t_f$ = final simulation time
        $\Delta t$ = time step size
        $N$ = number of time steps ($N = t_f/\Delta t$)
        $\epsilon$ = accuracy of computation of $\hat{Z}$
    Output:
        impedance weights $z_n$, $n = 0, ..., N$

    $M = 2N$
    $r = \epsilon^{1/2N}$
    for $m = 0 : M - 1$ do
        $\zeta = re^{i2\pi m/M}$
        $\Xi = \frac{1}{2}\zeta^2 - 2\zeta + \frac{3}{2}$
        $Z^{(m)} = \hat{Z}\left(\Xi/\Delta t\right)$
    end for
    for $n = 0 : N$ do
        $z_n = \frac{r^{-n}}{M}\sum_{m=0}^{M-1} Z^{(m)} e^{-i2\pi mn/M}$
    end for
end procedure
```

We compute the impedance weights for each outflow vessel prior to running a simulation; this requires $2N$ evaluations of $\hat{Z}$ per outflow vessel. The periodic structured tree condition requires N_T evaluations of the impedance, where N_T is the number of time steps per period. If N is not a small multiple of N_T, the algorithm described above could be more costly than the original structured tree. However, values of z_n converge to 0 quickly as n grows (see Figure 4.1). Therefore, for the generalized structured tree one could simply compute the weights for $n \leq N_T$ and set z_n to 0 for $n > N_T$. This approach would cause no noticeable difference in the solution, and would require precisely the same computational cost as the original structured tree.

The evaluation of $\hat{Z}$ is done directly and requires a few thousand floating point operations for the vascular trees considered here. One evaluation corresponds to $\mathcal{O}(\ell^2)$ floating point operations, where ℓ is the number of generations in the structured tree. Typically, ℓ is no more than 30. Both boundary conditions can thus be implemented at very low cost.

4.3 Singularities of the Laplace Transform of Impedance

The location of the singularities of the Laplace transform of the impedance plays a critical role in the implementation of the general structured tree boundary condition. For instance, the convolution quadrature method requires the existence of a real number ν such that for any singularity s^*, $\Re s^* \leq \nu$ [48]. Additionally, locations of the singularities of $\hat{Z}(s)$ play a critical role in Section 4.4, where we compare the general condition to the original, periodic version. Unfortunately, characterizing the singularities of $\hat{Z}(s)$ is not trivial since the impedance is only defined algorithmically as a repeated composition of (4.4) and (4.6). However, by analyzing the properties of the maps (4.4) and (4.6) individually, we prove that the impedance has only one singularity with nonnegative real part: a removable singularity at $s = 0$.

Theorem 4.3.1. *If the terminal impedance $\hat{Z}_{term}$ has nonnegative real part, i.e., $\Re\hat{Z}_{term} \geq 0$, then the Laplace transform of the impedance of the structured tree, as defined in Section 4.1, has no singularities for any s such that $\Re s \geq 0$, $s \neq 0$. There is a removable singularity at $s = 0$.*

Proof. The Laplace transform of the impedance is a repeated composition of the maps (4.4) and (4.6). These formulas are reproduced below:

$$\hat{Z}(0,s) = \frac{\hat{Z}(L,s) + \frac{1}{sd_sC}\tanh L/d_s}{sd_sC\,\hat{Z}(L,s)\tanh L/d_s + 1}$$

$$\frac{1}{\hat{Z}_{pa}(L,s)} = \frac{1}{\hat{Z}_{d1}(0,s)} + \frac{1}{\hat{Z}_{d2}(0,s)}$$

where $d_s^2 = A_0/[C\rho s(s+\delta)], \delta = 2\mu(\gamma+2)/(\rho r_0^2)$. Therefore, the possible singularities of the impedance of the structured tree can be characterized into seven different cases:

Singularities of (4.4)

1. $s = 0$
2. $d_s = 0$ or $s = -\delta$
3. For some vessel in the tree, $s(s + \delta)$ is not in the region of analyticity of the square root function
4. L/d_s is a singularity of tanh
5. $sd_sC \tanh(L/d_s)\hat{Z}(s, L) + 1 = 0$

Singularities of (4.6)

6. $\hat{Z}(s, 0) = 0$
7. For some junction in the tree, $\hat{Z}_{d1}(s, 0) = -\hat{Z}_{d2}(s, 0)$.

The proof consists of eliminating all the above cases. Since the real part of expression (4.4) is unchanged under complex conjugation of s, we only need to consider the quadrant $\Re s \geq 0$ and $\Im s \geq 0$. Additionally, we use the fact that $\delta, C, \rho, r_0, \mu, \nu$ and L are positive real constants due to their physiological meaning.

It is elementary to check that case 1 corresponds to a removable singularity. Since $\delta > 0$, case 2 is impossible. By Lemma 4.3.1 below, case 3 cannot be realized. Lemma 4.3.1 also implies that $\Re(L/d_s) > 0$, therefore case 4 is impossible since the singularities of tanh are purely imaginary.

Theorem 4.3.2 (below), which deals with the properties of (4.4) and relies on auxiliary Lemmas 4.3.2–4.3.6, allows us to eliminate cases 5, 6 and 7. Since $\hat{Z}_{term}$ has non-negative real part by assumption, it follows from Theorem 4.3.2 that $\hat{Z}(s, 0)$ has positive real part for any terminal vessel. Furthermore, for $\hat{Z}_{d1}(s, 0)$ and $\hat{Z}_{d2}(s, 0)$ with positive real part, the junction condition (4.6) implies that $\hat{Z}_{pa}(s, L)$ has positive real part as well. Therefore, in *any* vessel in the tree, $\hat{Z}(s, 0)$ has positive real part and $\hat{Z}(s, L)$ has nonnegative real part, with $\Re[\hat{Z}(s, L)] = 0$ being possible only for terminal vessels. This fact, combined with Lemma 4.3.5 implies that a singularity of the type 5 is not possible. Also, since $\Re(\hat{Z}(s, 0)) > 0$ for all vessels in the tree, singularities of the type 6 and 7 do not exist. This completes the proof of Theorem 4.3.1.

Theorem 4.3.2. *Consider the following family of mappings parameterized by s*

$$F_s(z) = \frac{z + a_s}{b_s z + 1},$$

where $a_s = \frac{1}{sd_sC}\tanh(L/d_s), b_s = sd_sC\tanh(L/d_s)$. *For any* $s \neq 0$ *with nonnegative real part,* F_s *maps the region* $\{z \in \mathbb{C}; \Re z \geq 0\}$ *into the region* $\{z \in \mathbb{C}; \Re z > 0\}$.

The proof of the above Theorem relies on several technical lemmas which we now state and prove.

Lemma 4.3.1. *For any nonzero* $s \in \mathbb{C}$ *in the first quadrant, i.e.,* $\Re(s) \geq 0$, $\Im(s) \geq 0$, *and* $s \neq 0$, *we have* $\Re\sqrt{s(s+\delta)} > 0$ *and* $\Im\sqrt{s(s+\delta)} \geq 0$ *where* δ *is a positive real number.* $\Im\sqrt{s(s+\delta)} = 0$ *only when* $s \in \mathbb{R}$.

Proof. Elementary. ☐

Lemma 4.3.2. *For* $s \in \mathbb{C}$ *such that* $\Re(s) \geq 0$ *and* $\Im(s) \geq 0$, *we have*

$$0 \leq \arg(sd_s) < \pi/4.$$

Proof. By definition of d_s, see Section 4.1.1, we note

$$\arg(sd_s) = \arg\sqrt{\frac{s}{s+\delta}} = \frac{1}{2}\left(\arg(s) - \arg(s+\delta)\right).$$

The desired inequalities are then easily obtained due to the fact that δ is real and positive. ☐

Lemma 4.3.3. *For* $z = x + iy \in \mathbb{C}$ *such that* $\Re(z) > 0$, *we have*

$$\tanh(z) = \frac{\sinh(2x)}{\cosh(2x) + \cos(2y)} + i\frac{\sin(2y)}{\cosh(2x) + \cos(2y)}$$

Proof. Elementary ☐

Lemma 4.3.4. *For* $z \in \mathbb{C}$ *such that* $\Re(z) > 0$ *and* $\Im(z) \geq 0$, *we have*

$$-\arg(z) \leq \arg(\tanh(z)) \leq \arg(z).$$

Equality only occurs when $\Im[z] = 0$

Proof. Set $z = x + iy, y > 0$. By Lemma 4.3.3,

$$\frac{\Im\left(\tanh(z)\right)}{\Re\left(\tanh(z)\right)} = \frac{\sin(2y)}{\sinh(2x)}.$$

Thus, the right of the two inequalities in the lemma is equivalent to showing the following for $x > 0, y > 0$,

$$\frac{\sin(2y)}{\sinh(2x)} < \frac{y}{x},$$

We first show that for $y > 0$, $\frac{\sin(2y)}{y} < 2$. Trivially, $\lim_{y\to 0} \frac{\sin(2y)}{y} = 2$. Also, $\frac{\sin(2y)}{y} < 2$ for $y > 1/2$, meaning we only need to consider $y \in (0, 1/2)$.

$$\frac{d}{dy}\frac{\sin(2y)}{y} = \frac{2y\cos(2y) - \sin(2y)}{y^2}$$

The numerator is 0 when $y = 0$ and $\frac{d}{dy}(2y\cos(2y) - \sin(2y)) = -4y\sin(2y) < 0$ for $y \in (0, 1/2)$ so $2y\cos(2y) - \sin(2y) < 0$ for $y \in (0, 1/2)$, meaning that $\frac{\sin(2y)}{y}$ is *decreasing* on $(0, 1/2)$, giving the desired result: $\frac{\sin(2y)}{y} < 2$ for $y > 0$.

We now show that $\frac{\sinh(2x)}{x} > 2$ for all $x > 0$. Trivially, $\lim_{x\to 0} \frac{\sinh(2x)}{x} = 2$.

$$\frac{d}{dx}\frac{\sinh(2x)}{x} = \frac{2x\cosh(2x) - \sinh(2x)}{x^2}$$

The numerator is 0 only when $2x = \tanh(2x)$. Since $\frac{d}{dz}\tanh(z) = \operatorname{sech}^2(z) < 1 = \frac{d}{dz}z$ for $z > 0$, the only value of x that satisfies $2x = \tanh(2x)$ is $x = 0$. Therefore, we have that for $x > 0$, $2x > \tanh(2x)$. Using the fact that $\cosh(2x) > 0$, we have that $\frac{d}{dx}\frac{\sinh(2x)}{x} > 0$, which implies that $\frac{\sinh(2x)}{x} > 2$ for all $x > 0$. This completes the proof of the rightmost inequality in the lemma, $\arg(\tanh(z)) \leq \arg(z)$.

We now prove the leftmost inequality in the lemma. To begin, we first show that for $y > 0$, $\frac{\sin(2y)}{y} > -2$. Clearly this holds for $y > 1/2$, so we need only consider $y \in (0, 1/2)$. Above we showed that $\frac{\sin(2y)}{y}$ is decreasing for $y \in (0, 1/2)$. Since $2\sin(1) > -2$, we have that $\frac{\sin(2y)}{y} > -2$ for *all* $y > 0$.

Also, our above arguments showed that for all $x > 0$, $-\frac{\sinh(2x)}{x} < -2$. Therefore, we have that for all $x > 0, y > 0$

$$-\frac{\sinh(2x)}{x} < \frac{\sin(2y)}{y}$$

since $\sinh(2x) > 0$ for $x > 0$, this inequality is equivalent to

$$-\frac{y}{x} < \frac{\sin(2y)}{\sinh(2x)}$$

This proves the leftmost of the 2 inequalities stated in the lemma.

□

Lemma 4.3.5. *For $s \in \mathbb{C}$ such that $\Re(s) \geq 0$ and $\Im(s) \geq 0$, we have $\Re[sd_s \tanh(L/d_s)] \geq 0$, with equality holding only when $s = 0$*

Proof. If $s \in \mathbb{R}, s \neq 0$ then the result is obvious. For the case $\Im[s] > 0$, we show $\Re[sd_s \tanh(L/d_s)] > 0$ by showing $|\arg(sd_s \tanh(L/d_s))| < \pi/2$. It follows from Lemma 4.3.1 that $\Re[\tanh(L/d_s)] > 0$ so $\arg[\tanh(L/d_s)] > -\pi/2$, which, when combined with Lemma 4.3.2, yields the following:

$$\arg(sd_s \tanh(L/d_s)) = \arg(sd_s) + \arg(\tanh(L/d_s)) > -\pi/2$$

For $\Im[s] > 0$, $\Im[\sqrt{s(s+\delta)}] > 0$ by Lemma 4.3.1 so we may use Lemma 4.3.4 to obtain the following:

$$\arg(sd_s \tanh(L/d_s)) = \arg(sd_s) + \arg(\tanh(L/d_s)) < \arg(s) + \arg(d_s) + \arg(1/d_s) = \arg(s) < \pi/2$$

□

Lemma 4.3.6. *For any $s \in \mathbb{C}$ where $\Re[s] \geq 0, \Im[s] > 0$, the following inequality holds*

$$\Im^2(a_s\overline{b_s}) < 4\Re(a_s)\Re(b_s)$$

where a_s and b_s are defined in Theorem 4.3.2.

Proof. We begin by simplifying the right hand side of the first inequality

$$\Re[a_s] = \frac{1}{C}\Re\left[\frac{1}{sd_s}\tanh(L/d_s)\right] = \frac{1}{C|sd_s|^2}\left(\Re(sd_s)\Re(\tanh(L/d_s)) + \Im(sd_s)\Im(\tanh(L/d_s))\right)$$

$$\Re[b_s] = C\Re[sd_s \tanh(L/d_s)] = C\left(\Re[sd_s]\Re[\tanh(L/d_s)] - \Im[sd_s]\Im[\tanh(L/d_s)]\right)$$

The above results yield a simplified form of $\Re[a_s]\Re[b_s]$:

$$\Re[a_s]\Re[b_s] = \frac{1}{|sd_s|^2}\left(\Re[sd_s]^2\Re[\tanh(L/d_s)]^2 - \Im[sd_s]^2\Im[\tanh(L/d_s)]^2\right)$$

The left hand side of the first inequality may also be simplified:

$$\Im[a_s\overline{b_s}] = \Im\left[\frac{|\tanh(L/d_s)|^2}{|sd_s|^2}\right]|\tanh(L/d_s)|^2 = -2\frac{|\tanh(L/d_s)|^2}{|sd_s|^2}\Re[sd_s]\Im[sd_s]$$

We can use the above results to simplify the first inequality

$$\begin{aligned}
\Im^2(a_s\overline{b_s}) &< 4\Re(a_s)\Re(b_s) \\
\frac{|\tanh(L/d_s)|^4}{|sd_s|^4}\Re[sd_s]^2\Im[sd_s]^2 &< \frac{1}{|sd_s|^2}\left(\Re[sd_s]^2\Re[\tanh(L/d_s)]^2 - \Im[sd_s]^2\Im[\tanh(L/d_s)]^2\right) \\
|\tanh(L/d_s)|^4\frac{\Im[sd_s]^2}{|sd_s|^2} &< \Re[\tanh(L/d_s)]^2 - \Im[\tanh(L/d_s)]^2\tan(\arg(sd_s)) \\
|\tanh(L/d_s)|^4\sin^2(\arg(sd_s)) &< \Re[\tanh(L/d_s)]^2 - \Im[\tanh(L/d_s)]^2\tan^2(\arg(sd_s))
\end{aligned}$$

For simplicity let $x \triangleq \Re[L/d_s], y \triangleq \Im[L/d_s]$. We may simplify the above inequality further by appealing to Lemma 4.3.3 and the identities $\sin^2(\theta) + \cos^2(\theta) = 1$ and $\cosh^2(\theta) - \sinh^2(\theta) = 1$:

$$[\cosh(2x) - \cos(2y)]^2\sin^2(\arg(sd_s)) < \sinh^2(2x) - \sin^2(2y)\tan^2(\arg(sd_s))$$

Denote $p \triangleq \Re[sd_s], q \triangleq \Im[sd_s]$. Substituting p and q into the above inequality gives

$$\left(\cosh^2(2x) - 2\cos(2y)\cosh(2x) + \cos^2(2y)\right)\frac{q^2}{p^2+q^2} + (1 - \cos^2(2y))\frac{q^2}{p^2} < \cosh^2(2x) - 1$$

Equivalently,

$$\frac{p^2+q^2}{p^2} < \frac{p^2}{p^2+q^2}\cosh^2(2x) + 2\frac{q^2}{p^2+q^2}\cosh(2x)\cos(2y) + \frac{q^4}{p^2(p^2+q^2)}\cos^2(2y)$$

Multiplying both sides by $p^2(p^2+q^2)$ gives

$$(p^2+q^2)^2 < (p^2\cosh(2x) + q^2\cos(2y))^2$$

By Lemma 4.3.2, $q < p$, which means that $p^2\cosh(2x) + q^2\cos(2y) > 0$, meaning we may take the positive square root of both sides of the above inequality. Simple trigonometric and hyperbolic trigonometric identities then show that the this inequality is equivalent to:

$$\frac{q^2}{p^2} < \frac{\sinh^2(x)}{\sin^2(y)}$$

Substituting $p = \Re[sd_s], q = \Im[sd_s]$ gives

$$\tan^2(\arg(sd_s)) < \cot^2(\arg(\tanh(L/d_s)))$$

By Lemma 4.3.4 and Lemma 4.3.1, $|\arg(\tanh(L/d_s))| < \arg(1/d_s) < \pi/2$. Therefore,

$$\cot^2(\arg(1/d_s)) < \cot^2(|\arg(\tanh(L/d_s))|) = \cot^2(\arg(\tanh(L/d_s))) \tag{4.17}$$

Furthermore, by assumption we have that $\Re[s] \geq 0, \Im[s] > 0$ so $\arg(s) < \frac{\pi}{2}$. This gives

$$\arg(sd_s) = \arg(s) + \arg(d_s) < \frac{\pi}{2} - \arg(1/d_s)$$

We use these two facts to complete the proof of the theorem by showing that inequality (4.17) holds. In the following we make use of the fact that $\arg(sd_s)$ and $\frac{\pi}{2} - \arg(1/d_s)$ are in $[0, \pi/2]$ ($\tan^2(\theta)$ is increasing for $\theta \in [0, \pi/2]$).

$$\tan^2(\arg(sd_s)) < \tan^2\left(\frac{\pi}{2} - \arg(1/d_s)\right) = \cot^2(\arg(1/d_s)) < \cot^2(\arg(\tanh(L/d_s)))$$

□

We may now turn to the proof of Theorem 4.3.2. Consider the mapping F_s for a particular s with nonnegative real part. Since we are only concerned with the real part of F_s, which is unchanged under complex conjugation of s, we need only consider $s \in \mathbb{C}$ where $\Re[s] \geq 0$ and $\Im[s] \geq 0$. We wish to show that for any $z \in \mathbb{C}$ where $\Re[z] \geq 0$, $\Re[F_s(z)] > 0$. Since $\Re[z] \geq 0$, $|\arg(z)| \leq \pi/2$. Lemma 4.3.5 implies $|\arg(b_s)| < \pi/2$, which means that the denominator of $F_s(z)$, $b_s z + 1$, is not zero (if $s = 0$ then the denominator is clearly nonzero also). Therefore, $\Re[F_s(z)] > 0$ if and only if:

$$\begin{aligned} 0 &< \Re\left[(z + a_s)\overline{(b_s z + 1)}\right] \\ &= \Re[b_s]\,|z|^2 + \Re[a_s \overline{b_s z}] + \Re\left[\overline{z}\right] + \Re[a_s] \end{aligned}$$

Write $z = x + iy$ and view the above function of a complex variable z as a function g_s of two real variables x and y. The above inequality is equivalent to the following inequality holding for all $x \in [0, \infty]$, $y \in \mathbb{R}$.

$$0 < \Re[b_s][x^2 + y^2] + \Re[a_s\overline{b_s}]x + \Im\left[a_s\overline{b_s}\right]y + x + \Re[a_s] \triangleq g_s(x, y)$$

We may find the minimum of g_s easily by analyzing its partial derivatives

$$\begin{aligned}\frac{\partial}{\partial x}g(x,y) &= 2\Re[b_s]x + \Re[a_s\overline{b_s}] + 1\\ &= 2\Re(b_s)x + \Re\left(\frac{\overline{sd}}{sd}\right)|\tanh(L/d_s)|^2 + 1\end{aligned}$$

By Lemma (4.3.5), $b_s \geq 0$. Lemma (4.3.2) implies that $\Re[\overline{sd}/sd] \geq 0$, so g_s is increasing with respect to x. Therefore, the minimum of g_s in the right half plane occurs on the imaginary axis($x = 0$) and this minimum may be found easily

$$\min_{x\geq 0, y\in\mathbb{R}} g(x,y) = \min_{y\in\mathbb{R}} g(0.y) = \Re(a_s) - \frac{\Im^2(a_s\overline{b_s})}{4\Re(b_s)}$$

Therefore, Theorem 4.3.2 is equivalent to the following inequality holding for all $s \neq 0$ with nonnegative real part:

$$\Im^2(a_s\overline{b_s}) < 4\Re(a_s)\Re(b_s) \tag{4.18}$$

By Lemma 4.3.6, the above inequality holds, which concludes the proof of the theorem.

□

4.4 Connection to Periodic Version of Structured Tree

We now investigate how our general structured tree boundary condition compares with the original boundary condition, which assumes periodicity in time. In Section 4.4.1, we show that for flow regimes that are periodic, both boundary conditions yield the same analytic solution. Furthermore, we have found that even in non-periodic regimes, the two boundary conditions give startlingly similar results. An explanation for this phenomenon is given in Section 4.4.2.

4.4.1 Comparison for Periodic Flows

If P and Q are periodic with period T, then

$$\frac{\hat{P}(i\omega_k)}{\hat{Q}(i\omega_k)} = \frac{\frac{\int_0^T P(t)e^{-i\omega_k t}dt}{1-e^{i\omega_k T}}}{\frac{\int_0^T Q(t)e^{-i\omega_k t}dt}{1-e^{i\omega_k T}}} = \frac{\hat{P}_k}{\hat{Q}_k},$$

where $\hat{P}(i\omega_k)$ and $\hat{Q}(i\omega_k)$ denote the Laplace transforms of pressure and flowrate evaluated at $i\omega_k$ with $\omega_k = 2\pi k/T$, and $\hat{P}_k$ and $\hat{Q}_k$ are the respective Fourier coefficients of P and Q.

Furthermore, the Laplace transform of the impedance satisfies $\hat{Z}(i\omega_k) = \hat{Z}_k$, where $\hat{Z}_k$ denotes the kth Fourier coefficient of the impedance (3.16). For periodic flow and pressure, enforcing $\hat{Z}(s) = \hat{P}(s)/\hat{Q}(s)$, as is done in the general structured tree condition derived in this dissertation, implies $\hat{Z}_k = \hat{P}_k/\hat{Q}_k$, meaning the *periodic* boundary condition is also satisfied. Thus, in a simulation with periodic inflow velocity data, one obtains the same solution from the periodic structured tree boundary condition and our general structured tree condition (neglecting numerical effects introduced by differences in implementation between the two methods).

4.4.2 Comparison for Non-Periodic Flows

Both the periodic and general structured tree conditions express the pressure as a dot product (discrete convolution) of flowrate history with impedance weights z_ℓ

$$P(n\Delta t) = \sum_{\ell=0}^{n} z_\ell Q((n-\ell)\Delta t). \tag{4.19}$$

For the general condition, the impedance weights are determined through the convolution quadrature method applied to the Laplace transform of the impedance in (4.16). For the periodic condition, the weights are determined by an inverse discrete Fourier transform of values of $\hat{Z}_k \triangleq \hat{P}_k/Q_k$, where $\hat{Z}_k$ are computed in a manner analogous to $\hat{Z}(s)$ (see [22] for full details). Explicitly, the impedance weights for the periodic condition are

$$z_\ell = \begin{cases} \dfrac{\Delta t}{T} \displaystyle\sum_{k=-(N_T-1)/2}^{(N_T-1)/2} \hat{Z}_k \mathrm{e}^{i\omega_k \ell \Delta t} & \text{for } \ell < N_T, \\ 0 & \text{for } \ell \geq N_T, \end{cases} \tag{4.20}$$

where $\omega_k = 2\pi k/T$ with T being the assumed period of P and Q. N_T is the number of time steps per period, so implicitly $z_\ell = 0$ for $\ell \geq N_T$ as the periodic condition only considers flowrate history over the previous period.

Although the derivation of the periodic structured tree condition requires the pressure and flowrate to be periodic in time, the resulting numerical implementation, (4.19), in no way forces the solution to be periodic. Therefore, it is *possible* to apply the periodic structured tree boundary condition to *any* type of flow even in the absence of any justification to do so. We compare this approach to the general structured tree boundary condition developed in this dissertation. Figure 4.1 displays the weights generated by each condition for the left posterior cerebral artery in the Circle of Willis, a ring-like structure of arteries in the human

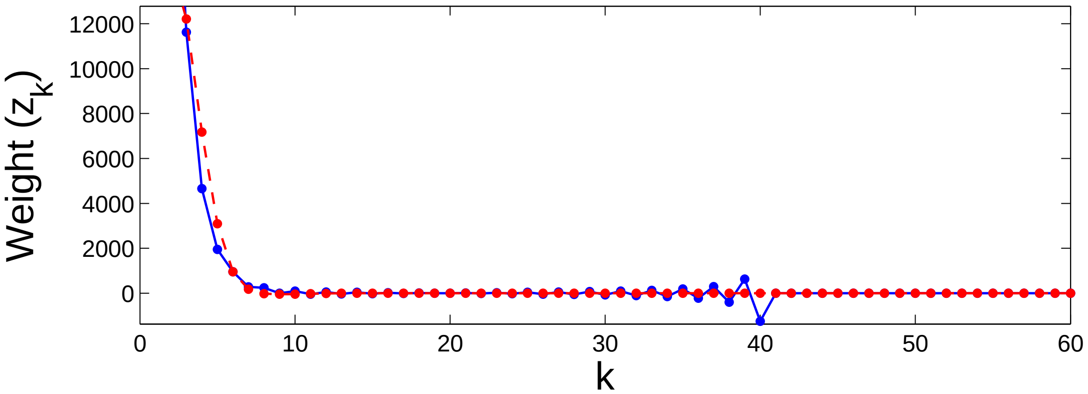

Figure 4.1: Comparison of the impedance weights generated by the periodic (blue, solid curve) and general (red, dashed curve) structured tree boundary conditions.

brain. Details about the Circle of Willis and parameter values used to generate these weights are given in Appendix A.

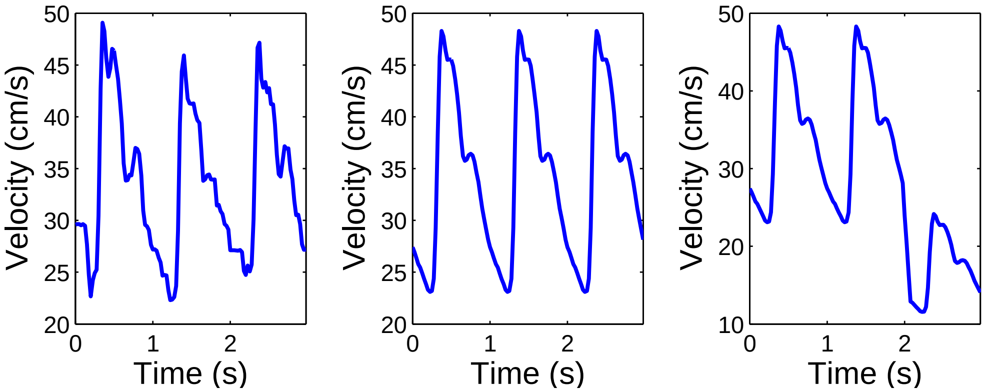

Figure 4.2: Inflow velocity curves for the left internal carotid for each of the three numerical experiments.

The similarity of the weights for both methods suggest that solutions obtained by using either boundary condition may be similar, even for non-periodic problems. This hypothesis is tested via numerical experiments in the Circle of Willis. We consider experiments with three different velocities applied to the inflowing vessels:

Experiment 1: Raw, quasi-periodic measured velocity data

Experiment 2: The raw data in experiment 1 that have been averaged and made periodic with period 1 second

Experiment 3: The periodic data from experiment 2 is used in all vessels except the left internal carotid artery, whose inflow velocity undergoes a rapid 50% decrease beginning at $t = 2$

The velocity for each experiment is displayed in Figure 4.2. Appendix A contains additional technical details on these simulations, such as discretization scheme, parameter values, and the network description of the Circle of Willis.

For each simulation, we measure the difference between the periodic and general structured tree solutions by computing the L^2 norm of the difference between the two solutions at each spatial point for both state variables (A and Q). The solutions at the spatial point in the Circle of Willis with the largest difference are displayed in Figures 4.3. As expected from the proximity of the weights, the solutions obtained by the two methods are remarkably similar.

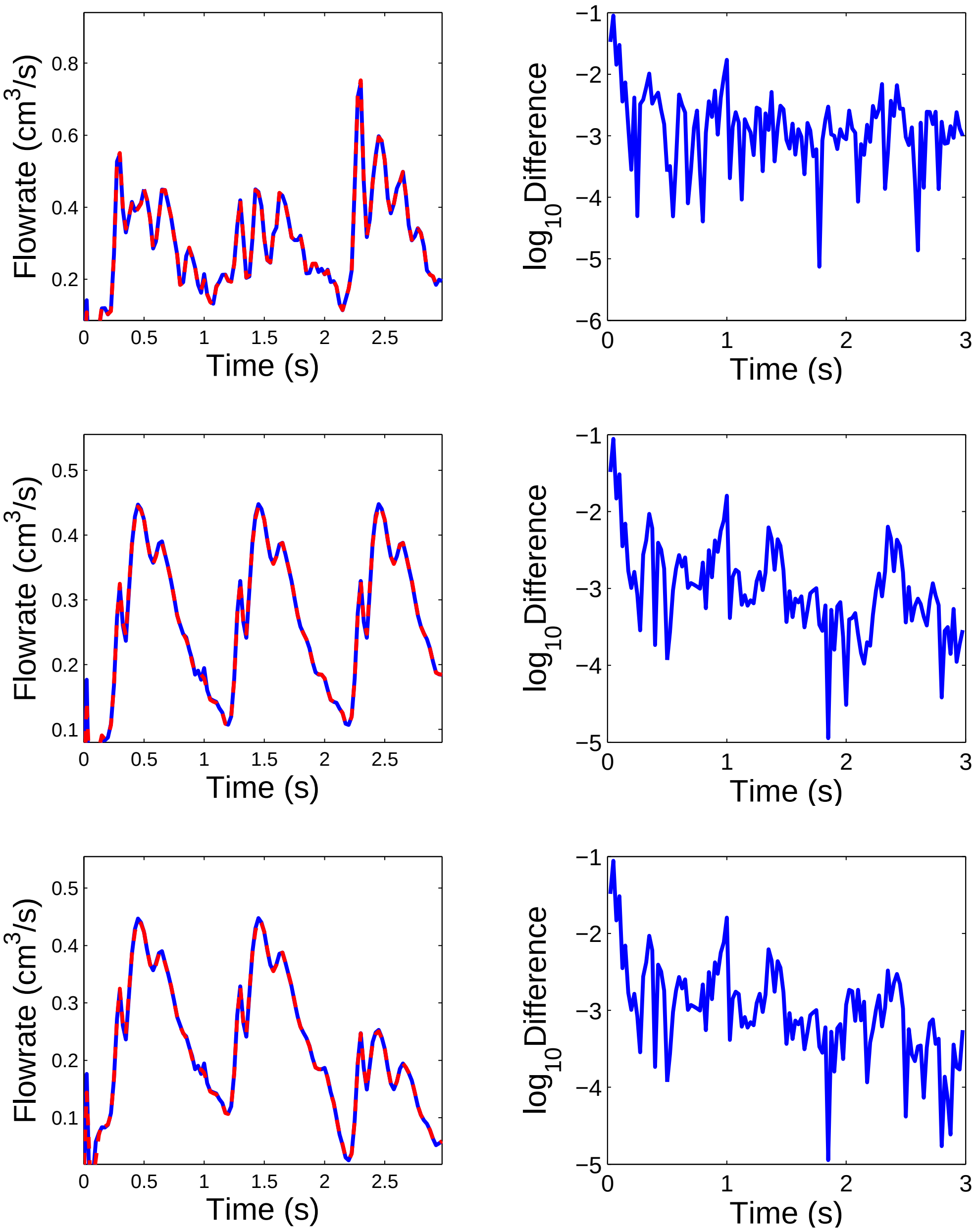

Figure 4.3: Top row: Left: solutions for a simulation using raw inflow velocity data with the periodic (blue, solid curve) and general (red, dashed curve) structured tree boundary conditions (experiment 1). The solution is displayed at the worst point in the network, see text. Right: logarithm of the absolute value of the difference between the two methods at that point. Middle row: idem for periodic inflow velocity data (experiment 2). Bottom row: idem for periodic inflow velocity data that experiences a rapid decrease at $t = 2$ with the periodic (experiment 3).

4.5 The Periodic Condition is an Approximation of the General Condition

The similarity between the periodic and general conditions is not coincidental. We now show that the numerical implementation of the periodic condition may be viewed as a rough approximation of the general condition $\hat{Z}(s) = \hat{P}(s)/\hat{Q}(s)$. Crucial to this argument is the central result of Section 4.3, which states that $\hat{Z}(s)$ has only one singularity for $\Re s \geq 0$: a removable singularity at $s = 0$. Furthermore, we assume that $\hat{Z}(s)$ is bounded in the right half plane $\Re[s] \geq 0$. We provide no analytical justification of this fact; however, based on numerical experiments, it does appear to be the case.

If Q is twice differentiable and $Q(0) = Q'(0) = 0$, then the following condition is equivalent to asserting $\hat{Z}(s) = \hat{P}(s)/\hat{Q}(s)$, where $\hat{Z}_R = \lim_s \to \infty \hat{Z}(s) = \sqrt{\rho/(A_0 C)}$:

$$P(t) = \int_0^t \mathcal{L}^{-1}\left[\frac{\hat{Z}(s) - \hat{Z}_R}{s^2}\right](t-\tau)Q''(\tau)d\tau + \hat{Z}_R Q(t) \tag{4.21}$$

Lemma 4.5.1. *The improper integral*

$$\lim_{T\to\infty} \frac{1}{2\pi i}\int_{\sigma-iT}^{\sigma+iT} \mathcal{L}^{-1}\left[\frac{\hat{Z}(s) - \hat{Z}_R}{s^2}\right] e^{s(t-\tau)}\, ds$$

converges uniformly with respect to T for $\tau \in [0,t]$.

Proof. Consider $\tau \in [0,t]$

$$\begin{aligned}
\mathcal{L}^{-1}\left[\frac{\hat{Z}(s) - \hat{Z}_R}{s^2}\right](t-\tau) &\triangleq \frac{1}{2\pi i}\int_{\sigma-i\infty}^{\sigma+i\infty} \frac{\hat{Z}(s) - \hat{Z}_R}{s^2} e^{s(t-\tau)} ds \\
&= \sum_{k=1}^{\infty} \frac{1}{2\pi i}\left(\int_{\sigma+i(k-1)}^{\sigma+ik} \frac{\hat{Z}(s) - \hat{Z}_R}{s^2} e^{s(t-\tau)} ds + \int_{\sigma-ik}^{\sigma-i(k-1)} \frac{\hat{Z}(s) - \hat{Z}_R}{s^2} e^{s(t-\tau)} ds\right) \\
&\triangleq \sum_{k=1}^{\infty} f_k(t)
\end{aligned}$$

$$
\begin{aligned}
|f_k(t)| &= \frac{1}{2\pi}\left|\int_{\sigma+i(k-1)}^{\sigma+ik} \frac{\hat{Z}(s)-\hat{Z}_R}{s^2}e^{s(t-\tau)}ds + \int_{\sigma-ik}^{\sigma-i(k-1)} \frac{\hat{Z}(s)-\hat{Z}_R}{s^2}e^{s(t-\tau)}ds\right| \\
&\le \frac{1}{2\pi}\left(\left|\int_{\sigma+i(k-1)}^{\sigma+ik} \frac{\hat{Z}(s)-\hat{Z}_R}{s^2}e^{s(t-\tau)}ds\right| + \left|\int_{\sigma-ik}^{\sigma-i(k-1)} \frac{\hat{Z}(s)-\hat{Z}_R}{s^2}e^{s(t-\tau)}ds\right|\right) \\
&\le K_Z\frac{e^{\sigma t}}{2\pi}\left(\left|\int_{\sigma+i(k-1)}^{\sigma+ik} \frac{1}{s^2}ds\right| + \left|\int_{\sigma-ik}^{\sigma-i(k-1)} \frac{1}{s^2}ds\right|\right) \\
&\triangleq M_k
\end{aligned}
$$

where $K_Z \triangleq \sup_{\nu\in\mathbb{R}} |\hat{Z}(\sigma+i\nu)-\hat{Z}_R| < \infty$ since $\hat{Z}(s)$ is analytic in this region by Theorem 4.3.1 and bounded as $|\nu| \to \infty$ by assumption.

$$
\sum_{k=1}^{\infty} M_k \le K_Z\frac{e^{\sigma t}}{\pi}\left(\frac{1}{\sigma^2} + \sum_{k=2}^{\infty}\frac{1}{k(k-1)}\right) < \infty
$$

By Weierstrass, the integral in the inverse Laplace transform operator converges uniformly for $\tau \in [0,t]$, which implies the following:

$$
\begin{aligned}
\int_{t-T}^{t} \mathcal{L}^{-1}\left[\frac{\hat{Z}(s)-\hat{Z}_R}{s^2}\right](t-\tau)Q''(\tau)d\tau &= \int_{t-T}^{t} \lim_{T\to\infty}\frac{1}{2\pi i}\int_{\sigma-iT}^{\sigma+iT}\frac{\hat{Z}(s)-\hat{Z}_R}{s^2}e^{s(t-\tau)}Q''(\tau)dsd\tau \\
&= \lim_{T\to\infty}\frac{1}{2\pi i}\int_{\sigma-iT}^{\sigma+iT}\int_{t-T}^{t}\frac{\hat{Z}(s)-\hat{Z}_R}{s^2}e^{-s\tau}Q''(\tau)d\tau e^{st}ds \\
&= \mathcal{L}^{-1}\left[\int_{t-T}^{t}\frac{\hat{Z}(s)-\hat{Z}_R}{s^2}e^{-s\tau}Q''(\tau)d\tau\right](t)
\end{aligned}
$$

□

In (4.21), $\hat{Z}_R = \lim_s \to \infty \hat{Z}(s) = \sqrt{\rho/(A_0C)}$, by (3.16). By assumption $\hat{Z}(s)$ is bounded, so the inverse Laplace transform of $\hat{Z}(s)/s^2$ exists and is continuous [109]. For large enough $t, \mathcal{L}^{-1}\left[(\hat{Z}(s)-\hat{Z}_R)/s^2\right](t)$ becomes linear. This was observed in extensive numerical experiments with full trees, and we now show this fact analytically for the case of a one vessel tree. The behavior of $\mathcal{L}^{-1}\left[\hat{Z}(s)/s^2\right](t)$ for large values of time is determined by the behavior of $\hat{Z}(s)/s^2$ when $s \approx 0$. Using the approximation $\tanh(L/d_s) \approx L/d_s$ for small s, we obtain the following for a tree with a single vessel:

$$
\frac{\hat{Z}(s)}{s^2} \approx \frac{\rho}{A_0C\hat{Z}_{term}}\left(\frac{1}{s^2} + \frac{a_1-a_2}{s^2(s+a_2)}\right)
$$

where $a_1 = A_0\hat{Z}_{term}/\rho L + \delta$ and $a_2 = 1/CL\hat{Z}_{term}$. We may invert this expression analytically to obtain the following (for $t \geq 0$).

$$\mathcal{L}^{-1}\left[\frac{\hat{Z}(s)}{s^2}\right] \approx \frac{\rho}{A_0 C\hat{Z}_{term}}\left[t - (a_1 - a_2)\left(-\frac{1}{a_2^2} + \frac{1}{a_2}t + \frac{1}{a_2^2}e^{-a_2 t}\right)\right]$$

a_2 is positive so the exponential term in the above quickly vanishes as t becomes large. In the case $\hat{Z}_{term} = 0$ one obtains the following inverse Laplace transform, which is exactly linear

$$\mathcal{L}^{-1}\left[\frac{\hat{Z}(s)}{s^2}\right] \approx \frac{L\rho}{A_0}(1 + \delta t)$$

In implementing the periodic structured tree condition, one must prescribe a value of the expected period T(typically $T \approx 1$). The convergence of $\mathcal{L}^{-1}\left[(\hat{Z}(s) - \hat{Z}_R)/s^2\right](t)$ to a linear regime typically occurs rather quickly with respect to t (within 0.1 to 0.3 seconds, i.e. much smaller than T), so it is reasonable to approximate (4.21) in the following way:

$$\begin{aligned}
P(t) &= \int_{t-T}^{t} \mathcal{L}^{-1}\left[\frac{\hat{Z}(s) - \hat{Z}_R}{s^2}\right](t-\tau)Q''(\tau)d\tau + \int_0^{t-T}\left[m(t-\tau) + b\right]Q''(\tau)d\tau + \hat{Z}_R Q(t) \\
&= I + II + \hat{Z}_R Q(t)
\end{aligned}$$

We may evaluate II exactly

$$\begin{aligned}
II &= mt\left[Q'(t-T) - Q'(0)\right] - m\left[\tau Q'(\tau)\Big|_{\tau=0}^{\tau=t-T} - \int_0^{t-T} Q'(\tau)d\tau\right] + b\left[Q'(t-T) - Q'(0)\right] \\
&= mtQ'(t-T) - m(t-T)Q'(t-T) + m\left[Q(t-T) - Q(0)\right] + b\left[Q'(t-T) - Q'(0)\right] \\
&= mTQ'(t-T) + mQ(t-T) + bQ'(t-T)
\end{aligned}$$

The integral in the inverse Laplace transform operator (4.8) converges uniformly by Lemma 4.5.1, so we may exchange the inverse Laplace transform operator and the outer integral.

$$\begin{aligned}
I &= \int_{t-T}^{t} \mathcal{L}^{-1}\left[\frac{\hat{Z}(s)-\hat{Z}_R}{s^2}\right](t-\tau)Q''(\tau)d\tau \\
&= \int_{t-T}^{t} \mathcal{L}^{-1}\left[e^{-s\tau}\frac{\hat{Z}(s)-\hat{Z}_R}{s^2}\right](t)Q''(\tau)d\tau \\
&= \mathcal{L}^{-1}\left[\frac{\hat{Z}(s)-\hat{Z}_R}{s^2}\int_{t-T}^{t} e^{-s\tau}Q''(\tau)d\tau\right](t) \\
&= \mathcal{L}^{-1}\left[\frac{\hat{Z}(s)-\hat{Z}_R}{s^2}\left(Q'(\tau)e^{-s\tau}\Big|_{\tau=t-T}^{\tau=t} + s\int_{t-T}^{t} Q'(\tau)e^{-s\tau}d\tau\right)\right](t) \\
&= Q'(t)\mathcal{L}^{-1}\left[\frac{\hat{Z}(s)-\hat{Z}_R}{s^2}\right](0) - Q'(t-T)\mathcal{L}^{-1}\left[\frac{\hat{Z}(s)-\hat{Z}_R}{s^2}\right](T) \\
&+ \mathcal{L}^{-1}\left[\frac{\hat{Z}(s)-\hat{Z}_R}{s}\int_{t-T}^{t} Q'(\tau)e^{-s\tau}d\tau\right](t)
\end{aligned}$$

The behavior of a function at $t = 0$ is determined by the behavior of its Laplace transform for large s. Specifically,

$$\mathcal{L}^{-1}\left[\frac{\hat{Z}(s)-\hat{Z}_R}{s^2}\right](0) = \lim_{s\to\infty}\frac{\hat{Z}(s)-\hat{Z}_R}{s} = 0$$

Using this fact and the approximate linearity of $\mathcal{L}^{-1}\left[(\hat{Z}(s)-\hat{Z}_R)/s^2\right](t)$, we have

$$\begin{aligned}
I &\approx -Q'(t-T)\left[mT+b\right] + \mathcal{L}^{-1}\left[\frac{\hat{Z}(s)-\hat{Z}_R}{s}\int_{t-T}^{t} Q'(\tau)e^{-s\tau}d\tau\right](t) \\
&= -Q'(t-T)\left[mT+b\right] + \mathcal{L}^{-1}\left[\frac{\hat{Z}(s)-\hat{Z}_R}{s}\left(Q(\tau)e^{-s\tau}\Big|_{\tau=t-T}^{\tau=t} + s\int_{t-T}^{t} Q(\tau)e^{-s\tau}d\tau\right)\right](t) \\
&= -Q'(t-T)\left[mT+b\right] + Q(t)\mathcal{L}^{-1}\left[\frac{\hat{Z}(s)-\hat{Z}_R}{s}\right](0) - Q(t-T)\mathcal{L}^{-1}\left[\frac{\hat{Z}(s)-\hat{Z}_R}{s}\right](T) \\
&+ \mathcal{L}^{-1}\left[(\hat{Z}(s)-\hat{Z}_R)\int_{t-T}^{t} Q(\tau)e^{-s\tau}d\tau\right](t) \\
&= -Q'(t-T)\left[mT+b\right] - mQ(t-T) + \mathcal{L}^{-1}\left[(\hat{Z}(s)-\hat{Z}_R)\int_{t-T}^{t} Q(\tau)e^{-s\tau}d\tau\right](t)
\end{aligned}$$

Now approximating the integral corresponding to the inverse Laplace transform operator (4.8) by a rectangle rule with spacing $2\pi/T$, we have

$$\begin{aligned}&\approx -Q'(t-T)\,[mT+b] - mQ(t-T)\\&+\sum_{k=-\frac{N-1}{2}}^{\frac{N-1}{2}} (\hat{Z}(i\omega_k+\sigma)-\hat{Z}_R)\left(\frac{1}{T}\int_{t-T}^{t} Q(\tau)e^{-(i\omega_k+\sigma)\tau}d\tau\right)e^{i\omega_k t}\end{aligned}$$

By Theorem 4.3.1 and the (4.8), σ may be any positive real number. Since $\hat{Z}(s)$ is continuous for all s with $\Re[s] \geq 0$, we take the limit as $\sigma \to 0$ to obtain:

$$I \approx -Q'(t-T)\,[mT+b] - mQ(t-T) + \sum_{k=-\frac{N-1}{2}}^{\frac{N-1}{2}} (\hat{Z}_k-\hat{Z}_R)\left(\frac{1}{T}\int_{t-T}^{t} Q(\tau)e^{-i\omega_k\tau}d\tau\right)e^{i\omega_k t}$$

If we approximate the Fourier integral of Q by a discrete Fourier transform of $Q(t-(N-1)\Delta t), ...Q(t)$, we obtain the following:

$$I \approx -Q'(t-T)\,[mT+b] - mQ(t-T) + \sum_{k=-\frac{N-1}{2}}^{\frac{N-1}{2}} \hat{Z}_k\tilde{Q}_k^{(N)}e^{i\omega_k t} - Z_R Q(t)$$

This yields the following approximation of the transient boundary condition

$$P(t) \approx I + II + Z_R Q(t)s = \sum_{k=-\frac{N+1}{2}}^{\frac{N+1}{2}} \hat{Z}_k\tilde{Q}_k^{(N)}e^{i\omega_k t} = \sum_{k=0}^{N-1} z_k Q((N-k)\Delta t)$$

where z_k denote the impedance weights in (3.22) computed by inverse discrete Fourier transform of values of $\hat{Z}_k$, meaning that the *periodic* boundary condition is a numerical approximation of the *general* boundary condition.

4.5.1 Numerical Issues with the Periodic Condition

The impedance weights for the periodic condition, although fairly close to the weights for the general condition, are oscillatory (Fig. 4.1). Additionally, even in a simulation with periodic inflow velocity, the periodic structured tree condition exhibits oscillations near $t = 1$ (middle of Fig. 4.3).

Another issue is that even in a simulation with periodic inflow velocity, the solution using the periodic condition converges to a periodic regime at a *slower* rate than the solution obtained from the general condition. To quantify this, we rewrite the solution "modulo T" into a sequence of grid functions

$$\mathcal{A}_k(x, t_n) = A(x, t_n + kT) \text{ and } \mathcal{Q}_k(x, t_n) = Q(x, t_n + kT).$$

We also define quantities which measure the relative change in the solution from one period to the next

$$\Delta_k \mathcal{A} \triangleq \max_{\substack{n=1,\ldots N_T \\ x\in\Omega}} \left| \frac{\mathcal{A}_{k+1}(x, t_n) - \mathcal{A}_k(x, t_n)}{\frac{1}{N_T}\sum_{n=1}^{N_T} \mathcal{A}_{k=1}(x, t)} \right|,$$

and similarly for $\mathcal{Q}_k$, where Ω is the set of all spatial points in the network. Figure 4.4 displays values of $\Delta_k = \max\{\Delta_k\mathcal{A}, \Delta_k\mathcal{Q}\}$ for each boundary condition for the simulation of the Circle of Willis with periodic inflow velocity data (Figure 4.3, middle). Remarkably, the solution from the general condition converges to a periodic regime at a substantially faster rate than the solution obtained from the periodic condition.

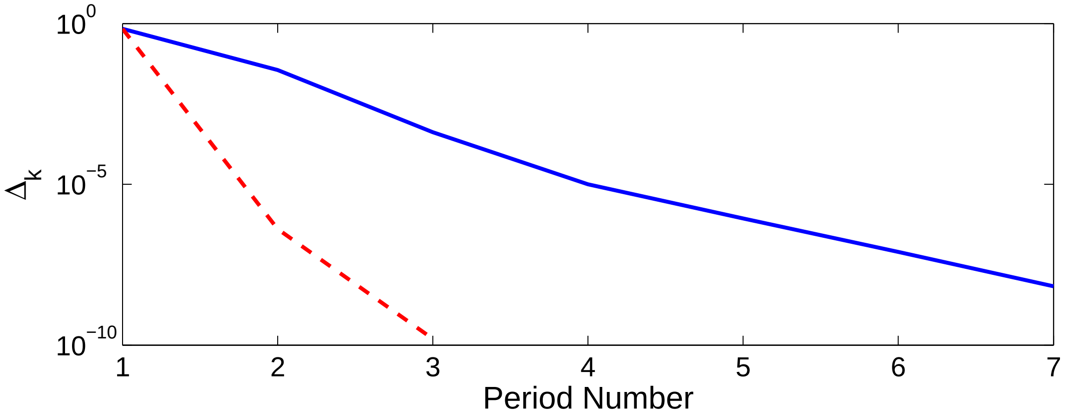

Figure 4.4: Values of Δ_k for the periodic (blue, solid line) and general (red, dashed line) structured tree conditions, showing that the general condition yields a solution converging to periodicity at a much faster rate than the original, periodic condition.

As done in Section (3.2.2), we provide an analysis of this phenomenon for the linearized equations (3.12) and (3.13) in a network consisting of a single vessel. Rather than fixing the velocity at the inlet, we fix the flowrate. Discretizing the system using Chebyshev collocation in space combined with backward Euler time integration allows us to represent the map from the numerical solution at period k to the numerical solution at period $k+1$ as a linear fixed point map. Specifically, if $\vec{z}^{\,k}$ is the solution at period k, we have

$$R\vec{z}^{\,k+1} = S\vec{z}^{\,k} + \vec{q} \tag{4.22}$$

where $\vec{q}$ is a vector containing imposed inlet flowrate values. To analyze the convergence of this fixed point iteration we computed the inverse of R semi-analytically and the computed the spectral radius using MATLAB's eig command. This was done for each of the outflowing vessels of the Circle of Willis. The results, displayed in Table 4.1, show that the spectral radius corresponding to the general condition is many orders of magnitude smaller than the spectral radius corresponding to the periodic condition. This is in agreement with the behavior observed in Fig. 4.4, where the solution obtained from the periodic structured tree converged to a periodic regime substantially slower than the solution obtained from the general structured tree condition.

Table 4.1: Spectral radii of $R^{-1}S$ in (4.22) for the periodic and general structured tree conditions. See Section (3.2.2) for a detailed description of the contents of R and S.

Vessel	R PCA	L PCA	R MCA	L MCA	R ACA	L ACA
Periodic Spec. Rad.	3.7e-03	3.3e-03	5.8e-03	5.2e-03	1.4e-02	8.0e-03
General Spec. Rad.	4.5e-15	4.5e-14	1.2e-12	6.0e-12	1.4e-16	2.5e-13

The slow convergence rate accompanying the periodic condition can have serious computational consequences. For example, the authors of [35] report that the periodic structured tree condition requires 8 periods to converge to a periodic regime in their 3D simulation of the cranial arterial tree, with one period requiring 3 hours of computation time. The results from this section indicate that the use of the general structured tree condition over the original, periodic version may yield substantial computational savings, even when one is performing simulations of blood flow that are periodic in time.

4.6 Conclusions

Unlike most outflow boundary conditions in computational hemodynamics, structured tree boundary conditions [22, 62, 63, 64, 82] have the advantage of being physiologically based. However, their derivation is based on Fourier series arguments which only apply to strictly *periodic* flows—a significant restriction in practice.

The new general structured tree boundary condition proposed here is valid for *all* flows. The periodic conditions from [22, 62, 63, 64, 82] can be viewed as numerical approximations to the new one. Our analysis shows that the new and old conditions yield results which are remarkably similar. One of the practical implications of the present work is that the "traditional" structured tree boundary conditions may be used for non-periodic flows even though they were not derived within that framework.

Cost and complexity being similar, the authors believe the new condition should be preferred over the old one both for periodic flows, as the numerical solution reaches periodicity much faster, and for general flows, as the new method has better stability properties.

Chapter 5

Parameter Selection for the Structured Tree

Despite the fact that the structured tree condition is physiologically based, selecting parameters for this condition is difficult in practice. Users of this condition have been forced to calibrate one or more parameters to get reasonable simulation results [9, 22, 63, 64, 81]. This fact is concerning for two reasons. First, although parameter calibration is often necessary for many models, it comes at the cost of a number of numerical simulations and can be difficult in the absence of experimental data. Second, the parameters in the structured tree represent physiological quantities, but the parameter values obtained by calibration are often physiologically unreasonable and often vary considerably between different outlet vessels within the same simulation [9, 22, 63, 64].

In this section, we attempt to answer the following question: Using the structured tree, is it possible to obtain reasonable simulation results *without* calibration while also using the *same* parameters for all outlet vessels? To do so, we reexamine various structural properties of arterial trees and the mechanics of blood flow in these trees. Specifically, we extend the tiered branching structure proposed by Steele et.al. [82, 81], incorporate non-continuum effects of blood flow in the microcirculation, and use a nonzero value of the terminal impedance at the leaves of the tree. By doing so, we find that we get reasonable results in a simulation of the systemic arterial tree *without* any calibration whatsoever. However, these parameter sets do not generate physiologically reasonable results in a simulation of the Circle of Willis. This may be due to organ specific aspects of arterial trees (see Section 5.4).

Unfortunately, the tiered branching structure we use comes at a substantial computational cost. To effectively eliminate this cost, we fit the Windkessel parameters to match the structured tree impedance as closely as possible. We find that, for a given set of structured tree parameters, it is possible to determine a set of Windkessel parameters so that there is only a small difference between simulation results from the two boundary conditions. We perform this optimization procedure for a variety of root radii, and the end result is an extremely simple method to estimate Windkessel parameters for an outlet vessel of any radius that matches the structured tree with the tiered branching structure.

5.1 A Closer Look at Structured Tree Parameters

Since the structured tree is derived from physiological principles, many of its parameters represent physical, measurable quantities (i.e. the vessel length-to-radius ratio, λ). Unfortunately, to obtain reasonable results, a number of authors have been forced to use parameter values that are physiologically questionable. For example, the authors of [22] use minimum radius values ranging from $80\mu m$ to $200\mu m$. The authors of [9, 64] use minimum radius values ranging from $100\mu m$ to $300\mu m$. As discussed in Section 5.1.5, these values are too large and, most importantly, there is no rule of thumb as to how one should select minimum radius values to get reasonable simulation results.

We now investigate the proper parameter values for the structured tree condition. Specifically, we consider tiered branching structures, blood viscosity properties in the microcirculation, and appropriate pressure values at the terminal sites of the structured tree. We find that these changes allow the structured tree to give acceptable results using physiologically reasonable parameter values *without* performing any calibration procedures or ad-hoc parameter adjustments in a simulation of the systemic arterial tree. However, the same parameter set yields unacceptable results in a simulation of the Circle of Willis.

5.1.1 Branching Parameters

In [81], Steele et. al. discussed the idea of using a tiered branching structure, rather than a single set of branching parameters for the entire tree. The parameters used in this work are included in Table 5.1, where ξ is the parameter satisfying $r_{pa}^{\xi} = r_{d_1}^{\xi} + r_{d_2}^{\xi}$, and ζ satisfies $\zeta = r_{d_2}/r_{d_1}$.

Table 5.2, which contains theoretical and measured values of ξ, suggests that the tiered structure used by Steele et. al. in [81] is accurate. Although there is some variation in the individual values of ξ, the values show a clear trend of being roughly 2.5 for the larger vessels, and

Table 5.1: Tiered branching parameter structure used by Steele et. al. in [81]

Radius Range	ξ	ζ
$250\mu\text{m} < r$	2.50	0.4
$50\mu\text{m} \leq r \leq 250\mu\text{m}$	2.76	0.6
$r < 50\mu\text{m}$	2.90	0.9

Table 5.2: Measured and theoretical values of the branching parameter ξ. A "sample" refers to a triplet of values of r_{pa}, r_{d_1}, r_{d_2} measured at a single junction.

ξ	Num. Samples	SD	Notes	Source
2.66	1533	0.081	$r \geq 100\mu\text{m}$	Suwa et. al. [84]
2.71	1455	0.092	$r < 100\mu\text{m}$	Suwa et. al. [84]
2.9	157	0.7	Measurements from ICA, ACA, MCA	Rossitti et. al. [74]
3	N/A	N/A	Theoretical optimum, laminar flow	Murray [58]
2.33	N/A	N/A	Theoretical optimum, turbulent flow	Uylings [90]
2.76	N/A	N/A		Olufsen [63]
2.55	183	0.03	$r \geq 800\mu\text{m}$	[8]
2.64		0.64	$r_{root} \leq 140\mu\text{m}$	[42]
2.32		0.18	$r_{root} > 140\mu\text{m}$	[42]
2.82	912 total		$r < 80\mu\text{m}$	[92]
2.50			$80\mu\text{m} \leq r \leq 400\mu\text{m}$	
2.35			$400\mu\text{m} < r$	
2.81			$30\mu\text{m} \leq r \leq 80\mu\text{m}$, measured data	[99]

closer to 3 for the smaller vessels. Furthermore, this behavior fits with the theoretical optima determined by Uylings and Murray. Under laminar flow conditions, Murray claimed that $\xi = 3$ is optimal [58]. Uylings claimed that $\xi = 2.33$ was optimal under turbulent flow conditions. In the larger arteries such as the aorta, the Reynolds number is $\mathcal{O}(1000)$ and some turbulence is present, whereas in the smaller arteries the Reynolds number is substantially lower and the flow is laminar [18, 66]. Therefore, if the structure of the arterial system adheres to the optima suggested by Uylings and Murray, ξ would be closer to 2.33 for the larger arteries and closer to 3 for the smaller arteries, which agrees precisely with the trend of the measured data in Table 5.2.

The radius dependence of the asymmetry parameter ζ is less clear, but available data does

Table 5.3: Asymmetry ratio data from VanBavel and Spaan [92]. A "sample" refers to a pair of values of (r_{d_1}, r_{d_2}) from a single junction.

Parent Radius (μm)	Number of Samples	Median ζ
< 60	326	0.765
60-100	425	0.582
100-150	193	0.546
150-280	352	0.501
180-1000	210	0.415
> 1000	157	0.400

support the general trend in the tiered structured devised by Steele et. al. Table 5.3 displays measured values of $\zeta = r_{d_2}/r_{d_1}$ for a variety of different radii. This data shows a clear trend of bifurcations being more symmetric for the smaller arteries. Kalsho and Kassab obtained similar findings in data from pig hearts, with ζ trending upward from roughly 0.1 for the largest vessels to 0.7 for the smaller arteries [43].

5.1.2 Vessel Length-to-Radius Ratio

A tiered set of parameters for λ is not incorporated in the tiered branching structure of Steele et. al. [81]. Rather, for each tree they use a constant value of λ that differs between different trees. These authors vary λ as a mechanism to control the relative impedance between different outlets, and use values of 20-80 for different trees. Although using different values of λ may be appropriate to account for organ specific aspects of these trees (see Section 5.4), this approach requires some calibration to ensure appropriate flow distributions and pressure ranges.

We now discuss how the length-to-radius ratio, λ, also exhibits a tiered structure. Nordsletten et. al [61] provided detailed data-based analysis on how the length-to-radius relationship varies with the vessel radius itself by grouping vessels according to their Strahler order. The Strahler ordering procedure, originally described in [83], labels all terminal vessels as order 0. When two vessels of order i merge, the parent vessel at this junction is assigned order $i + 1$. If two vessels of differing orders merge a at a junction, the order of the parent vessel is set equal to the larger of the two daughter orders. For example, when two order 0 vessels merge, the parent vessel at this junction is assigned order 1. When an order 0 and order 1 vessel merge, the associated parent is assigned order 1.

The data from Nordsletten et. al., reproduced in Table 5.5, implies that λ is larger for the

Table 5.4: Tiered λ structure proposed here combined with the tiered branching parameter structure used in [81].

Radius Range	λ	ξ	ζ
$250\mu\text{m} < r$	10	2.50	0.4
$50\mu\text{m} \leq r \leq 250\mu\text{m}$	20	2.76	0.6
$r < 50\mu\text{m}$	30	2.90	0.9

smaller vessels. These authors only included the radius and length data in their publication–we have extrapolated this data to compute rough estimates of λ by dividing these two values. This should only be taken as a rough estimate as we are estimating the average of L/r by the average of L divided by the average of r. Van Bavel et. al. fit a power law to measured data and obtained $L \approx 16.6r^{0.73}$. If we used this power law to define a radius dependent length-to-radius ratio as $\lambda = 16.6r^{-.27}$, we would see that λ decreases as r increases since $\partial\lambda/\partial r = -4.48r^{-1.27} < 0$.

We seek a set of parameter values for the structured tree that generates physiologically reasonable results without varying these parameters between different trees or performing any calibration. We propose appending a tiered λ structure to the tiered ξ and ζ structure used by Steele et. al. In [108], Zamir computes an average λ of 20 from a measured data set. Zamir also finds that λ has a limiting maximum value of 70, and this value is only approached in a small subset of the smaller arteries in the dataset. To match the mean value suggested by Zamir and the property that λ decreases as r increases [61, 92], we propose appending the tiered structure of Steele et. al. with a tiered structure for λ, with λ ranging from 10 to 30 (see Table 5.4).

5.1.3 Radius Dependent Viscosity

The effective viscosity of blood varies depending on the size of the tube through which it is flowing. This is due to the fact that in smaller arteries and capillaries whose diameter is not much larger than that of a red blood cell, red blood cells aggregate in the center of the vessel. A cell-free layer consisting primarily of plasma lines the interior vessel wall, and the net effect, originally noted experimentally by Fahraeus and Lindqvist, is to reduce the effective viscosity of blood as the vessel radius decreases [28]. The effective viscosity here is derived from Poiseuille's law [18]:

$$\Delta P = 8\frac{\mu L Q}{\pi r^4}. \tag{5.1}$$

Table 5.5: Data from Nordsletten et. al. [61]. We have computed and appended the left-most column of λ values by dividing the length and radius values originally published in [61]. Computed values of λ are rounded to the nearest integer.

Strahler Order	N Samples	Length (mm)	Radius (μm)	λ
0	29,566	312	10.08	31
1	13,070	423	13.90	30
2	4373	404	20.06	20
3	1245	656	29.87	22
4	578	1001	39.29	25
5	247	511	44.23	12
6	90	1031	53.87	19
7	24	2516	86.15	29
8	6	8975	139.83	64
9	3	1440	191.42	8
10	1	185	216.10	1

where ΔP is the pressure gradient between the beginning and end of a vessel, L and r are the length and radius of the vessel, and Q is the flowrate. The effective viscosity is obtained by solving for μ after measuring all other quantities in (5.1). Fahraeus and Lindqvist's findings have been further confirmed experimentally in [70, 10, 33, 37, 38, 72] and have been confirmed via a numerical particle dynamics method in [29].

In [71], Pries et.al. attempted to investigated the agreement of the Fahraeus and Lindqvist effect with in vivo data, as opposed to the in vitro data used by most studies. Although they did find that the effective viscosity does initially decrease as vessel radius decreases, eventually this effective viscosity reaches a local minimum and begins to *increase* as radius gets smaller. Based on this data, they proposed the following relative effective viscosity fit for a normal hematocrit value of 0.45:

$$\eta_{vivo} = \left[1 + (\eta^*_{0.45} - 1)] \left(\frac{D}{D-1.1}\right)^2\right] \left(\frac{D}{D-1.1}\right)^2$$

$$\eta^*_{0.45} = 6e^{-0.085D} + 3.2 - 2.44e^{-0.06D^{0.645}}$$

where D is the vessel diameter in microns. Instead of a constant viscosity value, we use the above diameter dependent viscosity.

5.1.4 Terminal Impedance

The structured tree requires a value of $\hat{Z}_{term}$ to be imposed at the ends of all terminal vessels. The typical convention is to simply set this value to 0 [63, 64, 81, 22, 23]. However, we will show that the correct value of $\hat{Z}_{term}$ is quite large. Suppose Q_{root} and P_{root} are the average flow and pressure at the root of a structured tree. This means that the average root impedance, $\hat{Z}_0$, is equal to P_{root}/Q_{root}. If the root vessel denotes a medium sized artery, a reasonable estimate for P_{root} would be 80mmHg. The location of the terminal sites of the tree will lie in the very small arteries or capillaries, meaning that the pressure there, P_{term}, will be roughly 30mmHg [18]. Therefore, the average pressure decreases by a factor 2-3 from the root to the leaves of the tree. However, Q_{root} must be distributed amongst all of the millions of terminal vessels. This analysis suggests that $\hat{Z}_{term,0}$ is roughly *one million times larger* than $\hat{Z}_0$. Since $\hat{Z}_0$ itself is already $\mathcal{O}(10^4)$ or larger (see Figure 3.2), this would mean that $\hat{Z}_{term}$ is $\mathcal{O}(10^9) \neq 0$.

The above argument makes only a rough estimate as to the magnitude of $\hat{Z}_{term}$. To obtain exact values of $\hat{Z}_{term}$, one would need to know the how the flowrate coming in from the root of the tree is distributed to its millions of terminal vessels. It may be possible to estimate the average flowrate through each of the different terminal vessels, although this would be complicated due to the large number of different radii values of the various leafs. However, the estimation of higher Fourier coefficients of the flowrate would be even more intricate. Instead of attempting to estimate the terminal impedance, we show how to incorporate more easily estimable terminal *pressure* values. At this time, we have only developed a simple algorithm for the case when this terminal pressure is constant in time.

To impose $P(t) = P_{term}$ at the terminal vessels of the structured tree, we slightly modify the definition of $\hat{Z}_k$. Instead of letting $\hat{Z}_k = \hat{P}_k/\hat{Q}_k$, we define $\hat{Z}_k$ as follows:

$$\tilde{Z}_k \triangleq \frac{\hat{P}_k - \hat{P}_{k,term}}{\hat{Q}_k} \tag{5.2}$$

Since P_{term} is constant in time, $\hat{P}_{k,term} = 0$ for $k \neq 0$, we have only changed the definition of the impedance for the $k = 0$ Fourier mode. For the original structured tree, the impedance is propagated from the end to the beginning of a vessel using Poiseuille's law:

$$\hat{P}_0(x = 0) = \hat{P}_0(x = L) + \frac{8\mu\lambda}{\pi r^3}\hat{Q}_0$$

therefore the impedance relation for the 0th Fourier mode is the same as when $\hat{Z}_k$ was defined simply as $\hat{Z}_k = \hat{P}_k/\hat{Q}_k$. Specifically, subtracting P_{term} from both sides and dividing by $\hat{Q}_0$ gives

$$\hat{Z}_0(0) = \hat{Z}_0(L) + \frac{8\mu\lambda}{\pi r^3}$$

this is exactly the same as the original DC impedance relation in Chapter 3 (see 3.17). The junction condition (3.8) also remains unchanged after this definition change of $\hat{Z}_k$. Furthermore, the appropriate terminal impedance for the impedance defined in (5.2) is 0 since what we wish to impose at the terminal sites is $\hat{P}_0 = P_{term}$ and $\hat{P}_k = 0$ for $k \neq 0$. Therefore, to compute actual values of the terminal pressure incorporating impedance, one need only run the original algorithm with $\hat{Z}_{term} = 0$. The difference arises only in the implementation, with P and Q being related by the following:

$$P(t) = P_{term} + \int_{t-T}^{t} Q(\tau)Z(t-\tau)\,d\tau$$

The only difference in this formulation and the original structured tree is the addition of the constant P_{term} to the convolution integral. For reasons discussed in Section 3.2, the above convolution integral should only be interpreted only in a weak since, and numerically it should be implemented strictly according to (3.22) with the terminal pressure added to the summation. [62, 18] suggest that the pressure in the smallest capillaries is roughly 25-35 mmHg. In practice, we use a value of $\hat{P}_{term} = 30$ mmHg.

5.1.5 Minimum Radius

As described in Section 3.1.1, the structured tree requires the user to prescribe a value of minimum radius, r_{min}. This value serves as a termination criterion for the tree, with vessels whose radius is less than r_{min} simply terminating (rather than bifurcating). Choosing r_{min} is challenging since this parameter is more artificial than the other branching parameters. The reason for this is that, in the human cardiovascular system, vessels do not merely terminate. Arteries perpetually branch while decreasing in size and eventually branch into capillaries. These capillaries decrease in size down to a radius of roughly $3\mu m$ [70], and then begin to merge together while increasing in size and eventually become veins. These veins then deliver blood back to the right atrium of the heart [18], meaning that there are no true terminal vessels.

Table 5.6 contains various r_{min} values used in implementations of the structured tree. These values highlight two practical issues that make the selection of r_{min} difficult. First, with the exception of the two studies by Steele, [82, 81], large values of r_{min} are used, meaning that a large portion of the arterial tree is being completely neglected. Steele uses the tiered branching

Table 5.6: Minimum radius values used in a variety of implementations of the structured tree condition. A * by a minimum radius value indicates that this study used a tiered branching structure, rather than a single set of branching parameters.

r_{min} Values	Source
80 μm - 200 μm	Cousins et. al. [22]
100 μm - 300 μm	Olufsen et. al [64]
100 μm - 600 μm	Olufsen [63]
4 μm*	Steele [82]
3 μm*	Steele et. al. [81]
20 μm	Torii et. al [88]

structured described in Section 5.1.1, while the other authors use a single set of branching parameters. Second, and most importantly, there is a tremendous variation in the values of r_{min}, even between different outlet vessels of the same simulation. Furthermore, there is no reliable rule of thumb to select r_{min}, meaning that users of the structured tree are forced to perform calibration procedures [22].

A natural minimum radius choice is 3μm, the radius of the smallest capillaries. For the simulations in Section 5.2, we use this natural choice of $r_{min} = 3\mu$m.

5.2 Simulation Results

We now perform a simulation of the systemic arterial tree using the structured tree with parameters described in Section 5.1. The only inlet in this network is the aorta; at this point we impose flowrate values measured by magnetic resonance techniques. We compare the simulation results to flowrate data at various points in the arterial tree. This data, as well as the radii and length data for the systemic arterial tree, was provided graciously by Mette Olufsen. This comparison is displayed in Figure 5.1, which shows that we have reasonable agreement between the simulation and data. Although we do not have measured pressure data, we display the computed pressure at various locations in Figure 5.2. We would expect the pressure in the aortic arc (top right of Figure 5.1) to range roughly between 80/120 mmHg. The computed pressure ranges between 70 mmHg and 140mmHg, so the average pressure is fairly accurate but the variation between the maximum and minimum pressures is too large.

The agreement of these simulation results with data is noteworthy for two reasons. First,

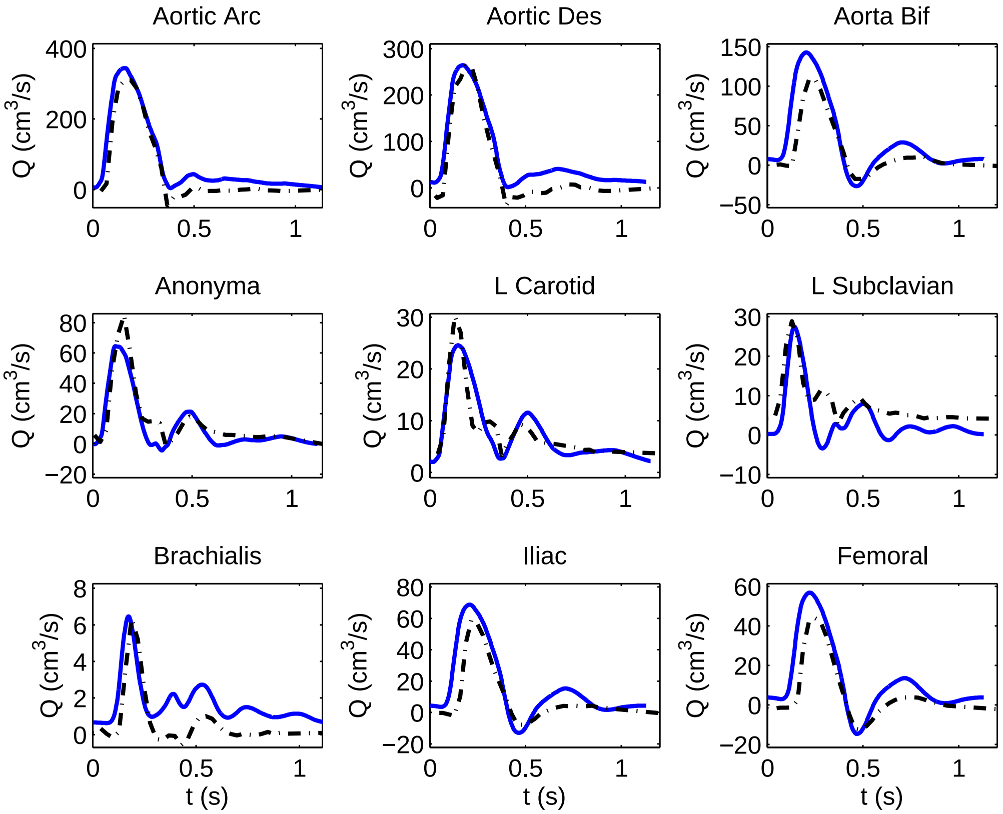

Figure 5.1: Computed (blue, solid curve) and measured (black, dot-dashed curve) flowrate values in various locations in the systemic arterial tree. The computed values were obtained using the structured tree boundary condition with parameters from Section 5.1.

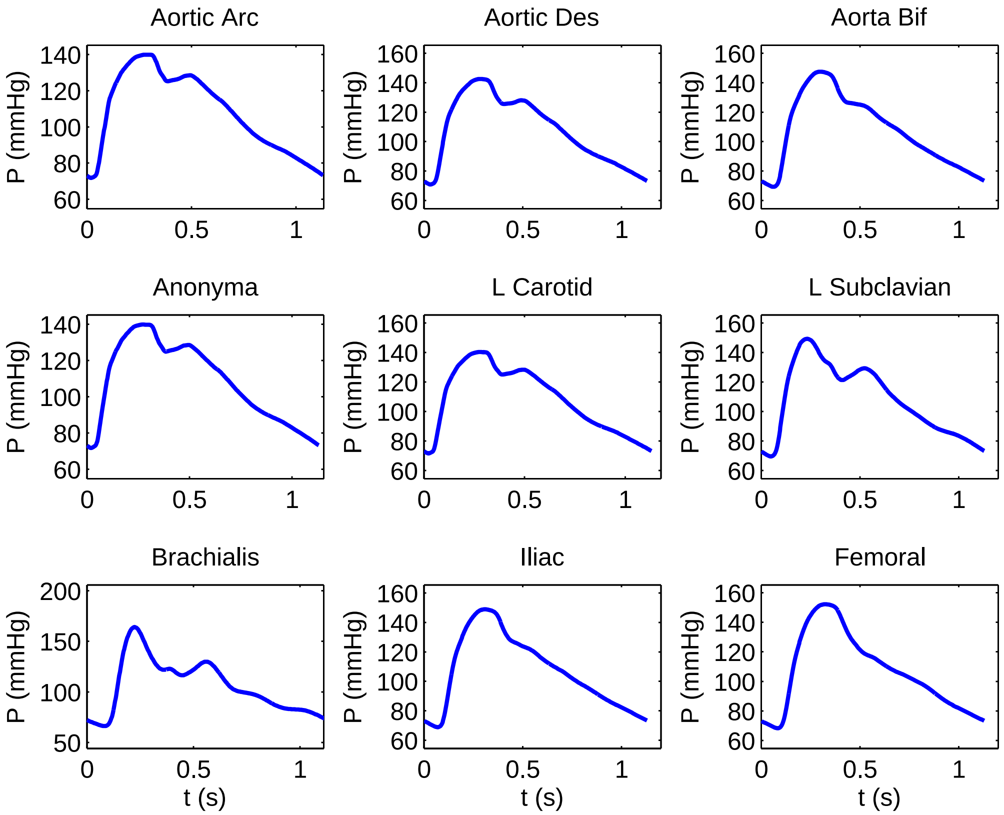

Figure 5.2: Computed pressure values at various locations in the systemic arterial tree using the structured tree condition with parameters from Section 5.1.

we used the *same* set of tree parameters for each outlet vessel in the network. Second, this parameter set was determined *without* any calibration of any kind and is based only on measured values from the literature. However, when we apply these same parameter sets to a simulation of the Circle of Willis, we no longer get physiologically reasonable results. The pressure values in this simulation are substantially larger than the correct physiological values (see Figure 5.3. Possible explanations of this discrepancy are given in Section 5.4.

5.3 Systematic Boundary Condition Comparison

A drawback to the tiered branching structure is that it substantially increases the computational cost of the structured tree. The self-similar structure induced by the single set of branching parameters means that, in a tree with N generations, there are only $\mathcal{O}(N^2)$ different vessel radii values, and the computational cost is thus also $\mathcal{O}(N^2)$, where N is roughly 20. (see Appendix A for a description of this algorithm). However, for the tiered branching structure this is no longer the case. For an N generation tree with k tiers, the computational cost is $\mathcal{O}(N^{k+1})$ since this is the number of distinct vessel radii. Although the computational cost per distinct vessel is small (1 evaluation of hyperbolic tangent and a few basic arithmetic operations, see (3.16)), these small costs can add up for tiered trees. For example, it takes ≈ 1 second to compute the vector of impedance weights for a tree with a global set of parameters, but it takes roughly $2-3$ minutes to perform the same computation for a 3-tiered tree (see Appendix A for a description of the computing environment). Considering the fact that this process must be repeated for each outlet of the network, the computational cost can become unwieldy for tiered trees.

We now investigate the fundamental differences between the pure resistor, Windkessel, and structured tree boundary conditions. Our goal here is to determine if it is possible to "fit" the pure resistor and/or Windkessel to the structured tree condition to eliminate the computational cost of the tiered branching structure. Although the derivations of these boundary conditions vary substantially, this fact alone does not imply that the simulation results obtained with these conditions will be vastly different. Of course, if the Windkessel and structured tree conditions are compared with each condition being supplied with an arbitrary chosen parameter set, their associated simulation results will likely differ. This fact motivates our definition of the concept of boundary condition equivalence: if for every possible choice of structured tree parameters there exists a set of Windkessel parameter such that the simulation results generated using these two conditions are identical, then we say these two boundary conditions are equivalent. For example, the following hypothetical boundary condition is trivially equivalent to the pure resistor condition:

$$P = 2KQ$$

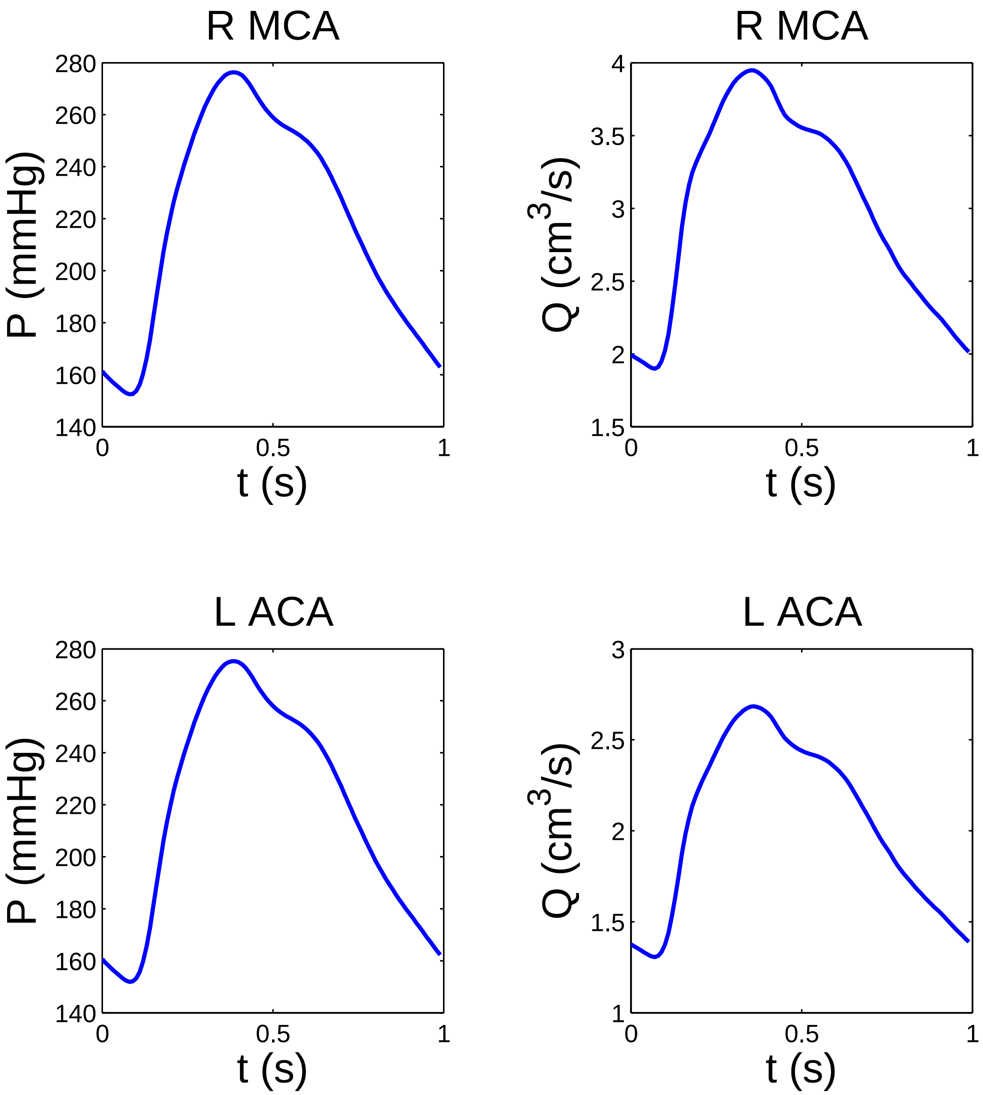

Figure 5.3: Computed pressure and flowrate values in the Circle of Willis using the structured tree boundary condition with parameters from Section 5.1.

Table 5.7: Ranges for randomly generated structured tree parameter sets

Parameter	Range
ξ	$2.3 \leq \xi \leq 3$
η	$0.3 \leq \eta \leq 0.6$
λ	$20 \leq \lambda \leq 70$
r_{min}	0.003 cm$\leq r_{min} \leq 0.02$ cm

since this boundary condition would generate results that agree exactly with the pure resistor condition if the resistance parameter R_0 were chosen to be equal to $2K$. The Windkessel and structured tree conditions do not share such an obvious connection. However, we now perform a number of numerical experiments that suggest that these conditions are *nearly* equivalent. Alternatively, these experiments also show that the pure resistor condition yields differences in simulation results that cannot be eliminated by a careful selection of the resistance parameter.

To investigate the difference between these three boundary conditions, we perform a variety of numerical experiments of blood flow in the Circle of Willis. Details of these experiments may be found in Appendix A. For each of the six outlet vessels in the Circle of Willis, we randomly generate a set of structured tree parameters, with each parameter being selected uniformly from specified ranges. These ranges are given in Table 5.7.

For each structured tree parameter set, we determine the set of Windkessel parameters that most closely fit the structured tree impedance. To do so, we compute the Fourier coefficients of the Windkessel condition, which states:

$$CR_1R_2\partial_t Q + (R_1 + R_2)Q = CR_2\partial_t P + P.$$

Taking the Fourier coefficients of both sides gives

$$\frac{\hat{P}_k}{\hat{Q}_k} = \frac{i\omega_k CR_1R_2 + R_1 + R_2}{1 + i\omega_k CR_2}$$

The structured tree gives us a direct way of computing $\hat{P}_k/\hat{Q}_k$, and we use this information to determine the values of Windkessel parameters (R_1, R_2, C). We enforce that the two conditions

Table 5.8: Numerical values of difference between numerical simulations of the Circle of Willis using the structured tree and Windkessel boundary conditions. The largest, median, and smallest difference rows correspond to the top, middle, and bottom plots in Figure 5.4.

	Difference	**Variable**	**Vessel**
Largest Difference	0.073	Flowrate	R Middle Cerebral Artery
Median Difference	0.031	Flowrate	Anterior Communicating Artery
Smallest Difference	0.016	Pressure	L Anterior Cerebral Artery

agree exactly for the 0th Fourier coefficient, which requires that $\hat{Z}_0 = R_1 + R_2$

$$f(R_1, C) = \sum_{k=1}^{n} \left| \hat{Z}_k - \frac{i\omega_k C R_1(\hat{Z}_0 - R_1) + \hat{Z}_0}{1 + i\omega_k C(\hat{Z}_0 - R_1)} \right|^2 .$$

The optimization is performed using the Levenberg-Marquardt algorithm in the "lsqnonlin" function in MATLAB (2011a, The MathWorks, Natick, Massachusetts, U.S.A.). We use $n = 20$. Numerical experiments in Appendix A suggest that the solutions to our model are smooth, meaning their Fourier coefficients are small for large values of k. Furthermore, our results were insensitive to changes in n. The pure resistor boundary condition enforces $P = RQ$, where R is the resistance parameter. To estimate this resistance parameter, we simply set $R = \hat{Z}_0 = R_1 + R_2$.

We ran 50 simulations of the Circle of Willis, where for each simulation each outflow vessel was prescribed a randomly generated structured tree parameter set according to Table 5.7. We then found the Windkessel and resistance parameters that best fit these randomly generated parameter sets by the optimization procedure described above. We then ran simulations of the Circle of Willis with the structured tree, Windkessel, and resistor conditions. For each of these simulations, we computed the L_∞ norm (in space and time) of the difference between the solutions. To compare the structured tree and Windkessel conditions, we include results from 3 selected simulations in Figure 5.4. The top plot corresponds to the simulation with the largest difference between the structured tree and Windkessel solutions, the middle plot displays the simulation with the median difference out of all of the simulations, and the bottom plot displays the simulation with the smallest difference. The plotted state variable was chosen to be the solution value/spatial location combination where this L_∞ difference between the structured tree and Windkessel is attained. Figure 5.5 contains analogous results for the pure resistor condition.

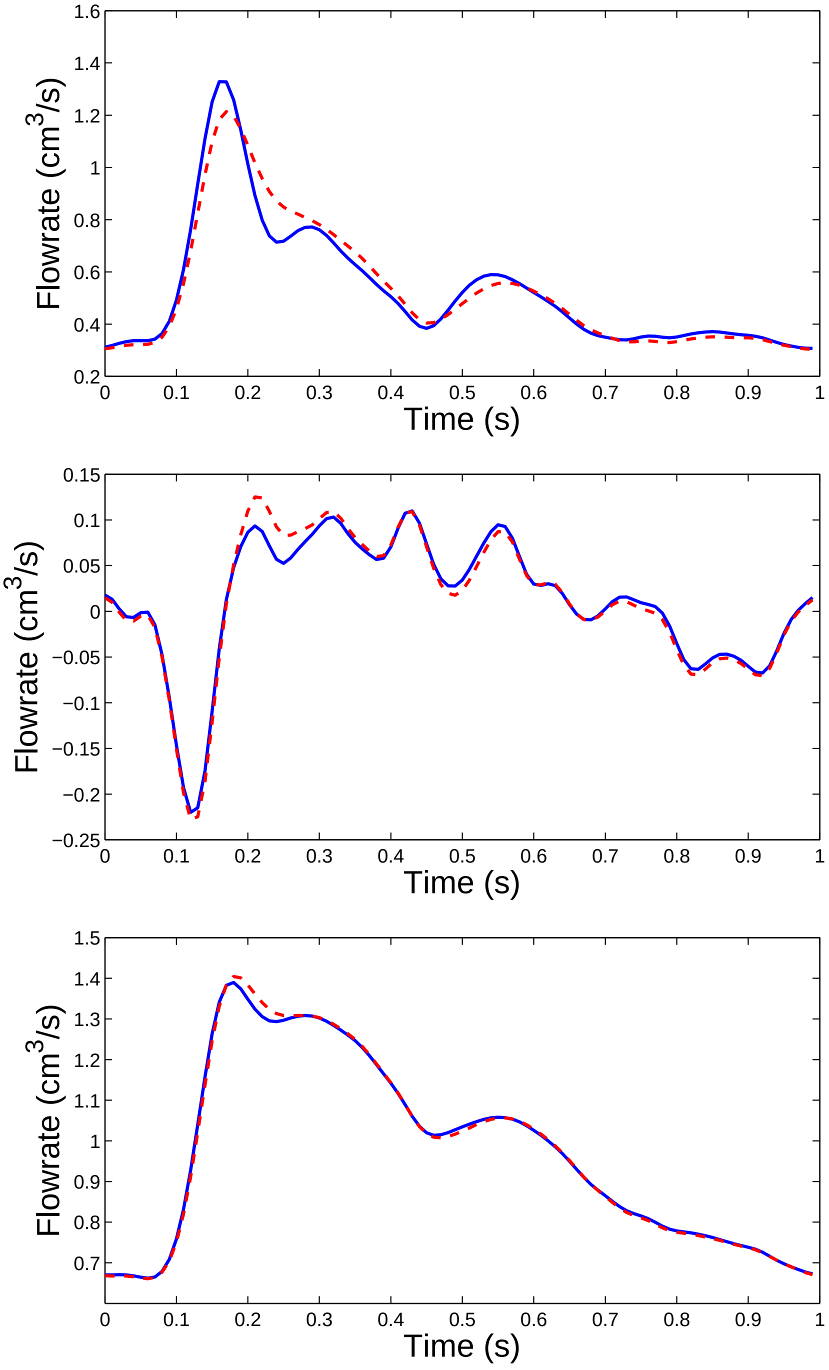

Figure 5.4: Comparison between the structured tree (blue, solid curve) and Windkessel (red, dashed curve) for simulations of the Circle of Willis with randomly generated tree parameters. The top plot displays the largest difference between the two, the middle plot displays the median difference, and the bottom plot is the smallest difference.

Table 5.9: Numerical values of difference between numerical simulations of the Circle of Willis using the structured tree and pure resistor boundary conditions. The largest, median, and smallest difference rows correspond to the top, middle, and bottom plots in Figure 5.5.

	Difference	**Variable**	**Vessel**
Largest Difference	0.301	Flowrate	R Middle Cerebral Artery
Median Difference	0.145	Flowrate	R Anterior Cerebral Artery
Smallest Difference	0.060	Flowrate	Anterior Communicating Artery

The results comparing the structured tree and Windkessel conditions in Figure 5.4 and Table 5.8 indicate that, for simulations of the Circle of Willis, these two boundary conditions are nearly equivalent. In the absolute worst case, the solutions from these two conditions differ by no more than 7%, with the median L_∞ difference being roughly 3%. The pure resistor boundary condition, on the contrary, is clearly not equivalent to the structured tree. Even after fitting the resistance parameter to match the tree, results from these two boundary conditions can differ by as much as 30%, with a median difference of around 15%. Additionally, the pure resistor condition produces qualitatively different flowrate curves in the top and middle plots of Figure 5.5, and lacks the pronounced peak that is present in the structured tree results when $t \approx 0.15$. Azer and Peskin also found substantial differences between the structured tree and pure resistor conditions [9].

Although the pure resistor condition is clearly incapable of matching the results of the structured tree, the numerical evidence in this section suggests that the Windkessel condition can give similar results if its parameters are tuned to the structured tree impedance. We stress that this fact alone does *not* imply that one can simply use the Windkessel rather than the structured tree. To obtain similar results between the two conditions, we first had to generate impedance spectra for the structured tree to produce the cost function used to optimize the Windkessel parameters.

The above results suggest that the Windkessel condition can give similar results to the structured tree if the Windkessel parameters are tuned to match the structured tree impedance. We now fit the Windkessel to the structured tree for a variety of different values of r_{root} using the structured tree parameters described in Section 5.1. We then approximate each of the Windkessel fits by a power law function of r_{root}. Then, rather than perform a costly simulation using 3-tiered structured tree, one can attain similar results by merely using these fits. Since we have already computed these fits, the marginal computational cost for a simulation using these

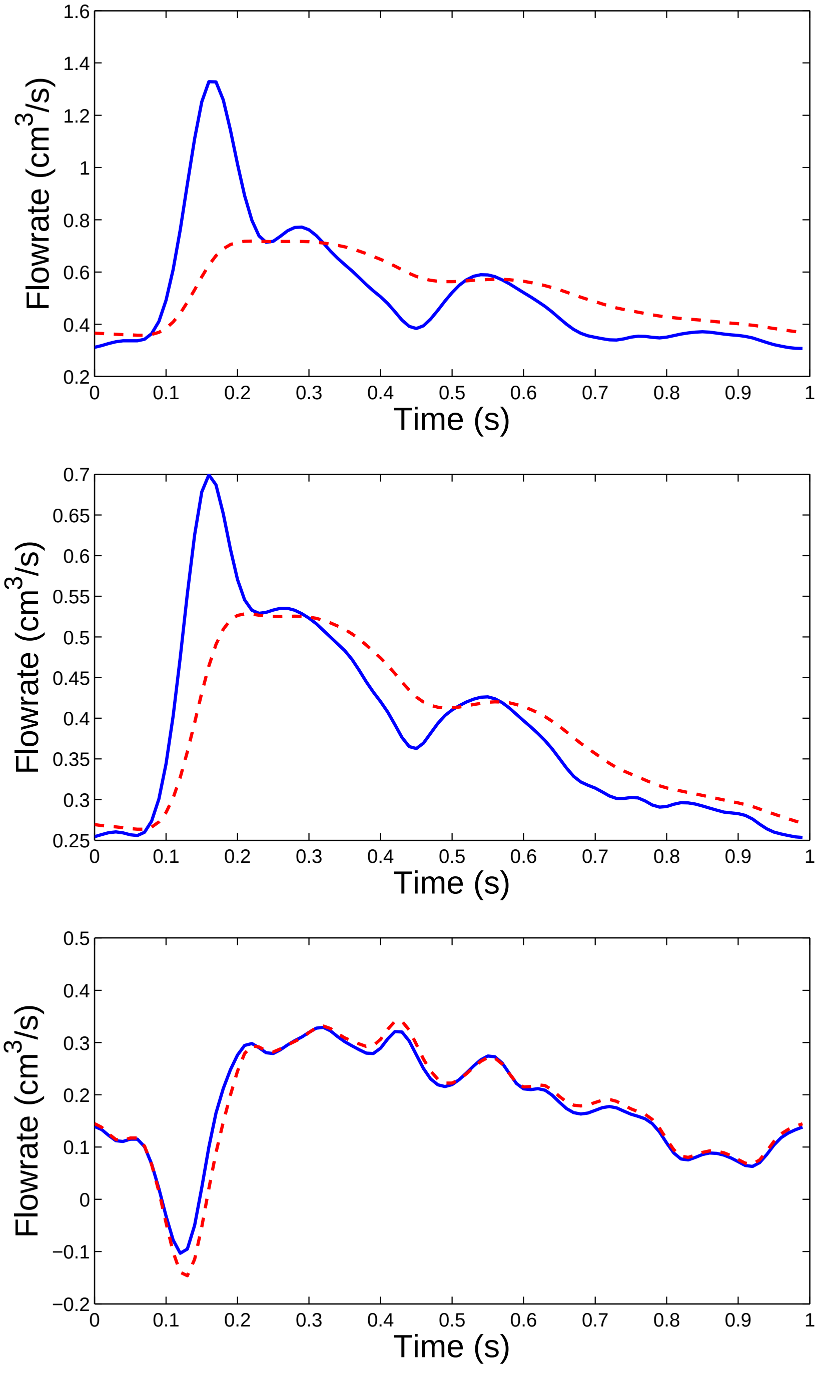

Figure 5.5: Comparison between the structured tree (blue, solid curve) and pure resistor (red, dashed curve) for simulations of the Circle of Willis with randomly generated tree parameters. The top plot displays the largest difference between the two, the middle plot displays the median difference, and the bottom plot is the smallest difference.

fits is *only* the cost of the numerical PDE solve and no additional impedance computation for 3-tiered trees is required. For each outlet vessel, the user may simply plug the root radius into the fits in Figure 5.6 to obtain values of R_1, R_2, and C that correspond to the structured tree with the tiered structure and radius dependent viscosity described in Section 5.1. The nonzero terminal pressure is not incorporated in these fits, but is included the implementation of the Windkessel condition:

$$CR_1R_2\partial_t Q + (R_1 + R_2)Q = CR_2\partial_t P + P - P_{term}.$$

The power law fits in Figure 5.6 provide a way around the computational cost of the tiered structured tree. A user may simply use these power law fits to determine a set of Windkessel parameters that most closely fit the structured tree with the tiered parameter structure described in Section 5.1. The results for the systemic arterial tree simulation (Figures 5.7 and 5.8) and the Circle of Willis simulation show that the Windkessel with these power law fits generates very similar results to the tiered structured tree.

5.4 Conclusion

We have attempted to determine a parameter set for the structured tree that gives reasonable simulation results *without* requiring calibration while still using the same set of branching parameters for each outlet. In order to determine such a parameter set, we examined various structural and mechanical aspects of the structured tree and found that some aspects of the structured tree were physiologically incorrect. After incorporating these changes, we were able to provide reasonably accurate simulation results for the systemic arterial tree without any calibration with a single parameter set used across all outlet vessels. Unfortunately, this parameter set yielded poor results for simulations of the Circle of Willis.

One possible way to improve our parameterization would be to use different branching parameters for trees in different organs of the body. Although this approach would be more complicated than a single set of branching parameters, organ specific branching parameters may be more physiologically correct [62, 81]. Examining the organ-specific differences of these branching parameters may provide a way to prescribe outflow boundary condition parameters that give reasonable simulation results without calibration. Such a parameterization would make it drastically easier to impose outflow boundary conditions, as a user would need to provide only the radius of the outlet vessel to uniquely determine a set of outflow boundary condition parameters.

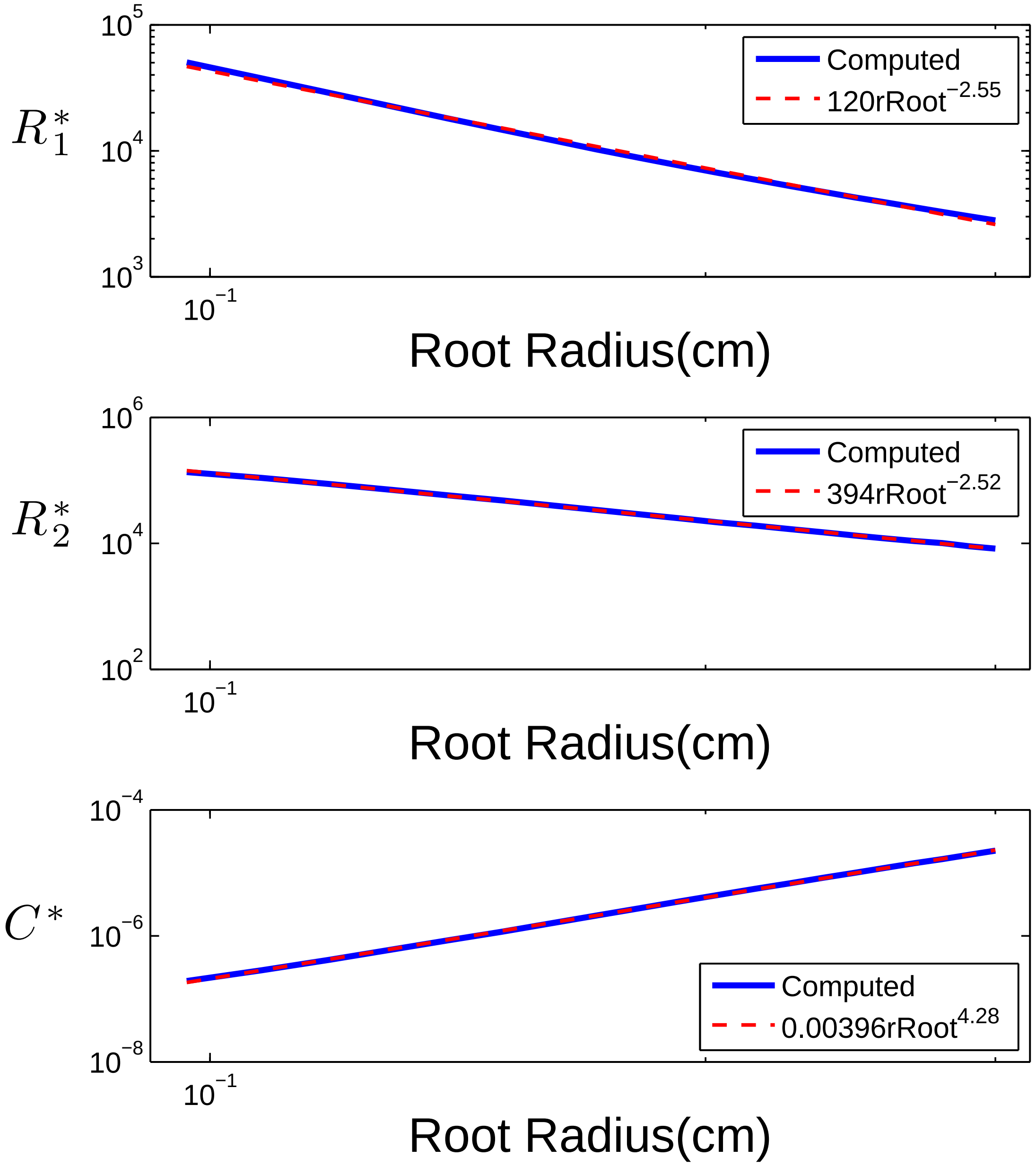

Figure 5.6: Fits of the Windkessel parameters to the structured tree using the tiered structure described in Section 5.1. The blue, solid curve represents the computed Windkessel parameters that match the structured tree impedance most closely, and the red, dashed curve is a power law fit to these fitted values.

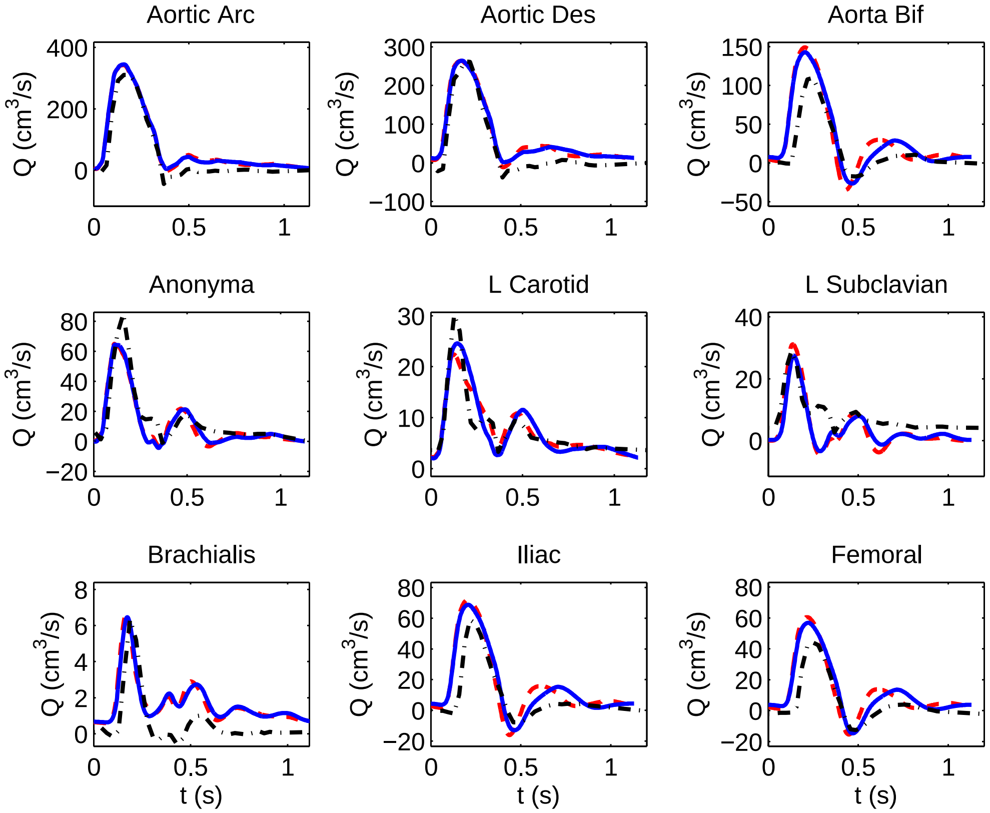

Figure 5.7: Computed structured tree (blue, solid curve), Windkessel with fitted parameters (red, dashed curve), and measured (black, dot-dashed curve) flowrate values in various locations in the systemic arterial tree. The computed values were obtained using the structured tree boundary condition with parameters from Section 5.1.

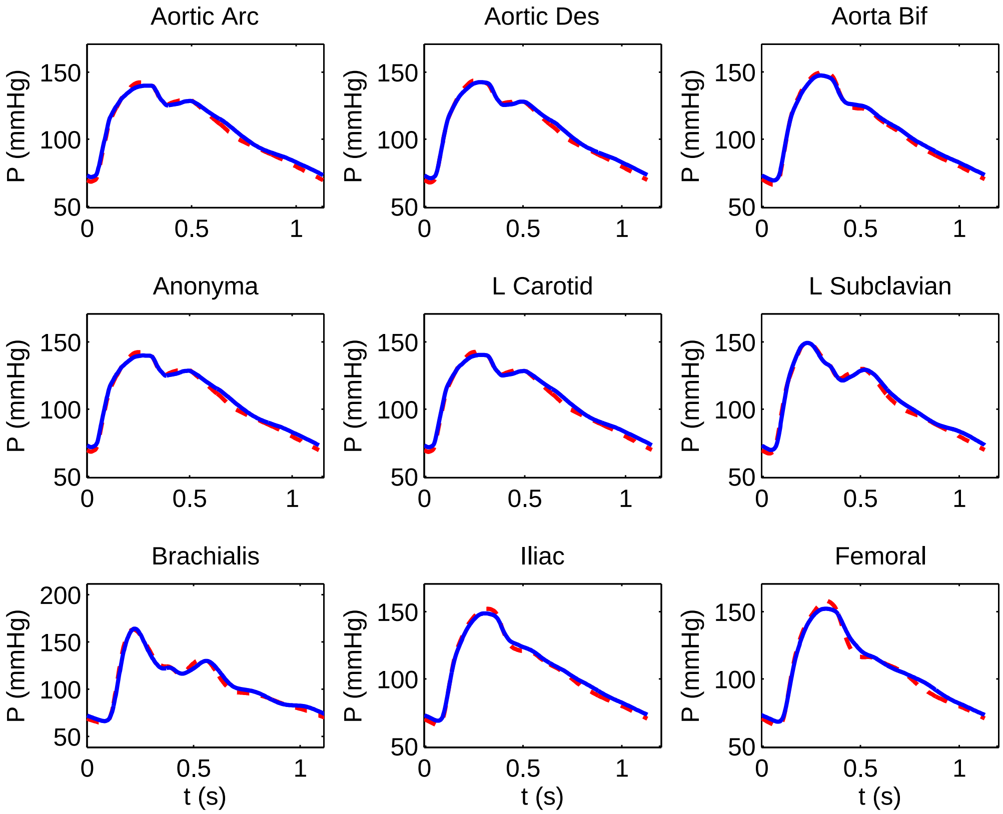

Figure 5.8: Computed pressure values at various locations in the systemic arterial tree using the structured tree condition using the structured tree (blue, solid curve) and the associated Windkessel fit (red-dashed curve).

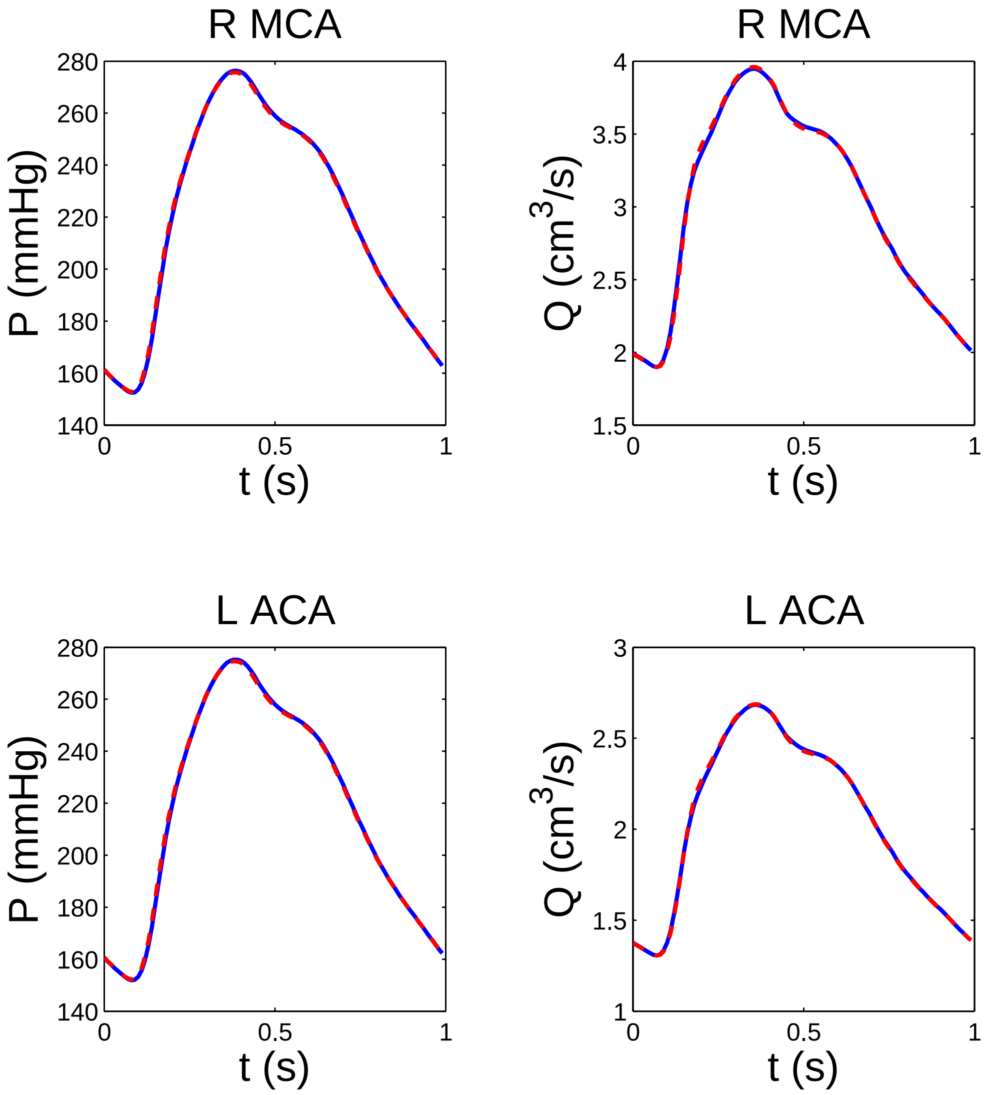

Figure 5.9: Computed pressure and flowrate values in the Circle of Willis using the structured tree (blue, solid curve) with parameters from Section 5.1 and the associated Windkessel fits (red, dashed curve).

Chapter 6

Uncertainty Quantification

In order to perform the blood flow simulations used in the prior chapters of this dissertation, we have used data and assumptions which contain some degree of uncertainty. For example, we used measured inflow velocity and anatomical data for the Circle of Willis, both of which contain measurement error. In order to derive a 1D model, we made a number of simplifying assumptions about the nature of the flow. The structured tree assumes a self-similar branching structure for the small arteries which, although reasonable, is an imperfect idealization. The uncertainty accompanying each of these model components implies that the simulation results themselves also contain uncertainty.

Quantifying the effects that these types of uncertainties have on simulation results gives insights on the reliability of model predictions. For example, Chen et. al. [19] quantified the uncertainty in flow and pressure in simulations of the systemic arterial tree introduced by uncertainty in boundary conditions and parameters. They found that uncertainty in the solution was due primarily to uncertainty in the imposed flowrate values at the inlet. They also found that uncertainties in the unstressed radius of the vessel (r_0) and resistance values used at outlets also provided a substantial contribution to the simulation uncertainty. Other authors have also performed uncertainty quantification studies for blood flow, examining the impacts of uncertain radius of abdominal aortic aneurysms [76] and uncertainty in the elastic properties of the arterial wall [105].

The above uncertainty quantification studies for blood flow models quantified simulation uncertainty using polynomial chaos methods. Although polynomial chaos approaches may be the most efficient choice in many settings, these methods suffer from scalability issues when the dimensionality of the uncertain input space is sufficiently high dimensional. [102]. PDF/CDF methods are recently proposed alternatives to polynomial chaos and involve deriving a deterministic differential equation for the evolution of the probability density function or cumulative distribution function for the uncertain model solution [85, 97, 98, 93, 45, 94]. Although PDF/CDF methods have a number of desirable properties, their currently can only be used for first order scalar equations. We investigate the extension of these methods to first order hyperbolic systems, which would provide a powerful new tool for uncertainty quantification for blood flow and other phenomena described by such equations. Unfortunately, we find that there are roadblocks which make such an extension difficult. We also find that similar issues make it difficult to obtain PDF equations for non-smooth solutions to scalar conservation laws.

6.1 PDF Equations

A common paradigm used to quantify the uncertainty in the simulation caused from uncertainty in model parameters and boundary conditions is to treat these uncertain inputs as random variables/fields. This implies that the associated model solution is also a random field. One then computes a probabilistic description of this model output. To frame our discussion of PDF methods, we briefly discuss two of the most prominent methods for uncertainty quantification: Monte Carlo sampling and polynomial chaos.

Monte Carlo sampling computes a probabilistic description of the model solution by generating many realizations of the random inputs and then compute the solution corresponding to each realization. The statistics of these realizations are then used to approximate those of the uncertain model solution. This process, termed Monte Carlo sampling, is broadly applicable but converges at a rate of $1/\sqrt{N}$, where N is the number of realizations [16].

Polynomial chaos methods represent an alternative approach [103]. Although the uncertain model inputs are random, the *map* from these inputs to the model solution is deterministic. Polynomial chaos methods approximate this map by polynomials, which means polynomial chaos is *extremely* efficient if this map is smooth and there are a small-to-moderate number of random inputs [103, 106, 107, 102, 104]. One may then approximate quantities such as the mean and variance of the model solution by computing the mean and variance of this polynomial approximation. Unfortunately, the computational cost of this approach grows exponentially with respect to the number of random inputs rendering it unusable when the number of random inputs is large, even when techniques such as sparse grid collocation are used [102].

Any random variable X possesses a cumulative distribution function (CDF), $F_X(a)$, where $F_X(a) \triangleq \mathcal{P}(X \leq a)$. In certain cases, a random variable X will also possess a probability density function (PDF), denoted $p_X(a)$, where $p_X(a) = \frac{\partial}{\partial a}F_X(a)$. In the context of a differential equation with random inputs, one seeks to characterize the stochastic properties of a random field $u(x, t, \omega)$, leading one to consider the PDF and CDF of this random field, denoted $p_u(U, x, t)$ and $F_u(U, x, t)$ respectively. A recently introduced method for uncertainty quantification method is to determine a single closed partial differential equation determining the evolution $p_X(a)$ or $F_X(a)$ [85, 97, 98, 93, 45, 94]. These PDF and CDF equations have a number of advantages over competing methods such as Monte Carlo simulation and polynomial chaos:

1. One obtains a complete probabilistic description of the model solution.
2. It does not suffer from the "curse of dimensionality" inherent in polynomial chaos expansions and is thus suitable even for problems with a large number of random inputs.
3. These equations can yield theoretical insights into the qualities of the random model solution. For instance, for some nonlinear models the associated equations can be linear and may be solved analytically. An example of this phenomena is given in Section 6.1.1.

We now investigate the possibility of deriving PDF equations for 1st order systems of hyperbolic balance laws. This approach would allow us to perform novel and computationally efficient uncertainty quantification studies for blood flow problems. We begin by considering the scalar balance law case in Section 6.1.1 before moving on to systems in Section 6.1.2. Although we are able to derive useful equations for some special cases, we find that the task of deriving closed PDF equations for systems suffers from some fundamental difficulties not present in the scalar case. The character of these difficulties does, however, suggest some possible changes in approach that could make it possible to derive useful PDF equations.

6.1.1 Scalar Balance Laws

To begin, we outline the derivation of a deterministic equation for the PDF of a solution to a scalar balance law subject to random initial data. The following derivation of the PDF equation for this scalar problem is not new and may be found in [85, 97]. To begin, consider the following scalar equation with random initial data:

$$\frac{\partial u}{\partial t} + \frac{\partial f(u)}{\partial x} = g(u), \qquad x \in \mathbb{R}, t > 0 \tag{6.1}$$

$$u(x, 0, \omega) = u_0(x, \omega) \tag{6.2}$$

$\omega \in \Omega$, where $(\Omega, \mathcal{F}, \mathcal{P})$ is a probability space. To derive an equation for the PDF of the above stochastic problem, the authors of [85] consider the following representation for the PDF of u, denoted $p(U, x, t)$:

$$p(U, x, t) = \mathbb{E}\left[\Pi(U - u(x, t, \omega)\right]$$

where $\Pi(U, x, t, \omega) \triangleq \delta(U - u(x, t, \omega))$, where δ denotes the Dirac delta function. The advantage of this representation of the PDF is that it exhibits nice properties when differentiated. For example, the time derivative of the PDF p satisfies

$$\frac{\partial p}{\partial t} = \mathbb{E}\left[\frac{\partial}{\partial t}\Pi\right] = \mathbb{E}\left[\frac{\partial \Pi}{\partial u}\frac{\partial u}{\partial t}\right] = \mathbb{E}\left[-\frac{\partial \Pi}{\partial U}\frac{\partial u}{\partial t}\right].$$

Since $\Pi = \delta(U - u)$

$$-\frac{\partial}{\partial U}(pg(U)) = -\frac{\partial}{\partial U}\left(\mathbb{E}[\Pi]g(U)\right) = -\mathbb{E}\left[\frac{\partial}{\partial U}\Pi g(U)\right] = -\mathbb{E}\left[\frac{\partial \Pi}{\partial U}g(u)\right].$$

The x derivative of p satisfies

$$\frac{\partial p}{\partial x} = \mathbb{E}\left[\frac{\partial}{\partial x}\Pi\right] = \mathbb{E}\left[\frac{\partial \Pi}{\partial u}\frac{\partial u}{\partial x}\right] = \mathbb{E}\left[-\frac{\partial \Pi}{\partial U}\frac{\partial u}{\partial x}\right].$$

Combining this with the fact that $\Pi = \delta(U - u)$ gives

$$\mathbb{E}\left[-\frac{\partial \Pi}{\partial U}f'(u)\frac{\partial u}{\partial x}\right] = -\frac{\partial}{\partial U}\mathbb{E}\left[\Pi f'(U)\frac{\partial u}{\partial x}\right] = f'(U)\frac{\partial p}{\partial x} + f''(U)\int_{-\infty}^{U}\frac{\partial p}{\partial x}(U', x, t)\,dU'.$$

The legitimacy of some of the above steps, such as the using the chain rule to the only weakly differentiable function Π, may be justified rigorously [45]. To use the above relationships to derive an equation for the PDF of u, multiply (6.3) by $-\partial\Pi/\partial U$ and take the expectation of both sides of the resulting equations. The above derivative identities give the following:

$$\frac{\partial \rho}{\partial t} + f'(U)\frac{\partial p}{\partial x} + f''(U)\int_{-\infty}^{U}\frac{\partial p}{\partial x}(U', x, t)\,dU' + \frac{\partial}{\partial U}(pg(U)) = 0 \tag{6.3}$$

The initial data for this equation is the PDF of u_0 in (6.2):

$$p(U, x, 0) = p_{u_0}(U, x)$$

This simple example illustrates the advantages of the PDF equation approach. Equation (6.3) is a linear, scalar, first order partial differential equation in 2 space dimensions (x and U). Solving this equation gives the PDF of the stochastic solution up to controllable numerical discretization error. While a method such as polynomial chaos would struggle if the initial data were a random field with high dimensionality, complicated initial data does not increase the complexity of the PDF equation approach since one only need prescribe the initial PDF.

6.1.2 Systems of Hyperbolic Balance Laws

Prior studies have considered scalar equations, and deterministic equations for the PDF of stochastic solutions to first order systems has not been developed [85, 97, 98, 93, 45, 94]. We now attempt to extend these PDF methods to first order hyperbolic systems of balance laws. PDF equations for such systems would provide a useful uncertainty quantification tool for blood flow, as well as other phenomena modeled with such first order systems. The derivation of a PDF equation for scalar equations required the solutions to be smooth–we maintain this smoothness assumption here as this appears to be the case for solutions to our blood flow model.

A system of first order balance laws may be written in the following form:

$$\frac{\partial u}{\partial t} + \frac{\partial f(u)}{\partial x} = g(u), \qquad x \in [a,b], t > 0 \tag{6.4}$$

where $u(x,t,\omega) = [u_1(x,t,\omega), ..., u_N(x,t,\omega)]^T$, $f : \mathbb{R}^N \to \mathbb{R}^N$, and $g : \mathbb{R}^N \to \mathbb{R}^N$ and the Jacobian of f is diagonalizable with real eigenvalues for all u. For now, we assume u, f, and g are smooth functions. $\omega \in \Omega$, where $(\Omega, \mathcal{F}, \mathcal{P})$ is a probability space. We consider randomness in the solution u introduced by random initial and boundary conditions.

$$\begin{aligned} u(a,t,\omega) &= u_L(t,\omega) \\ u(b,t,\omega) &= u_R(t,\omega) \\ u(x,0,\omega) &= u_0(x,\omega) \end{aligned}$$

To develop equations for the probability density function of u subject to random inputs, we consider the generalized function Π:

$$\Pi(x,t,U_1,...,U_N) \triangleq \prod_{i=1}^{N} \delta(U_i - u_i).$$

The significance of Π is that $\mathbb{E}[\Pi] = \rho(x,t,U_1,...U_N)$, where ρ is the joint PDF of $u_1,...u_N$. Differentiating Π with respect to t gives, weakly,

$$\frac{\partial \Pi}{\partial t} = \sum_{i=1}^{N} \frac{\partial \Pi}{\partial u_i}\frac{\partial u_i}{\partial t} = -\sum_{i=1}^{N} \frac{\partial \Pi}{\partial U_i}\frac{\partial u_i}{\partial t}.$$

Multiplying the ith equation of (6.4) by $-\partial\Pi/\partial U_i$ and summing the resulting N equations gives

$$\frac{\partial \Pi}{\partial t} - \sum_{i=1}^{N} \frac{\partial \Pi}{\partial U_i}\frac{\partial f(u_i)}{\partial x} = -\sum_{i=1}^{N} \frac{\partial}{\partial U_i}\left(\Pi g_i(U)\right),$$

where $U = [U_1, ..., U_N]^T$. Taking expectations of this scalar equation gives

$$\frac{\partial \rho}{\partial t} - \sum_{i=1}^{N} \mathbb{E}\left[\frac{\partial \Pi}{\partial U_i}\frac{\partial f_i(u)}{\partial x}\right] = -\sum_{i=1}^{N} \frac{\partial}{\partial U_i}\left(g_i(U)\rho\right),$$

where ρ is the joint probability density function of $u_1, ..., .u_n$. We may write this equation more compactly as

$$\frac{\partial \rho}{\partial t} - \mathbb{E}\left[\nabla_U \Pi \cdot \partial_x f(u)\right] = -\nabla_U \cdot (\rho g), \tag{6.5}$$

where $\nabla_U = \left(\frac{\partial}{\partial U_1}, ..., \frac{\partial}{\partial U_N}\right)$.

Equation (6.5) is not in a computationally useful form since it is not closed due to the $\mathbb{E}[\nabla_U \Pi \cdot \partial_x f(u)]$ term. A simple closure model is to take the expectation of this product to be the product of the expectations. This gives the following closed, but now inexact, equation for ρ:

$$\frac{\partial \rho}{\partial t} - \partial_x \mathbb{E}[f(u)] \cdot \nabla_U \rho = -\nabla_U \cdot (\rho g). \tag{6.6}$$

This equation is closed since we may compute the expectation of $f(u)$ directly from ρ. This closure is *exact* if $\partial_{U_i}\Pi$ and $\partial_x f_i(u)$ are independent. To examine the accuracy of this closure model we use (6.6) to model the evolution of ρ for constant coefficient systems with a variety of different random initial data.

Consider equation (6.4) with $f(u) = Au$, $g(u) = 0$, where A is an $N \times N$ matrix with constant entries and is diagonalizable with real eigenvalues. In this case, (6.4) reduces to

$$\frac{\partial u}{\partial t} + A\frac{\partial u}{\partial x} = 0 \tag{6.7}$$

let u_d be a deterministic solution to this equation with periodic boundary conditions in space and the following deterministic initial data:

$$u_d(x, 0) = u_d^0(x)$$

Let $\xi = [\xi_1, ..., \xi_N]^T$ be a vector of independent random variables. Then the solution to (6.7) with random in initial data $u_d^0(x) + \xi$ is $u(x,t) = u_d(x,t) + \xi$. We may use this fact to write the distribution of $u(x,t)$ in terms of the distribution of ξ.

$$\rho = \prod_{i=1}^{N} \rho_{\xi_i}(U_i - u_{d_i}) \tag{6.8}$$

where ρ_{ξ_i} is the probability density function of ξ_i. The derivation of the above formula for ρ is straightforward and makes use of the fact that the ξ_i are independent. The significance of this result is that the *true* PDF satisfies the closed equation (6.6) *exactly*:

$$\frac{\partial \rho}{\partial t} = \sum_{i=1}^{N} \frac{\partial \rho}{\partial U_i} \frac{\partial u_i}{\partial t} = -\nabla_U \rho \cdot \frac{\partial u}{\partial t} = \nabla_U \rho \cdot A \frac{\partial u}{\partial x} = \frac{\partial (A u_d)}{\partial x} \cdot \nabla_U \rho$$

As additional validation of this result, we solve the following 1st-order system subjected to additive initial noise with independent components:

$$\frac{\partial}{\partial t} \begin{bmatrix} v \\ w \end{bmatrix} + \begin{bmatrix} 0 & -c^2 \\ -1 & 0 \end{bmatrix} \frac{\partial}{\partial x} \begin{bmatrix} v \\ w \end{bmatrix} = 0 \tag{6.9}$$

the random initial data is:

$$v(x,0) = \sin(x) + \xi_v$$
$$w(x,0) = \cos(x) + \xi_w$$

where ξ_v and ξ_w are $\mathcal{N}(0,1)$ and independent. We use a value of $c = 1.5$. This system corresponds to the scalar second order wave equation, $u_{tt} = c^2 u_{xx}$, with $v = u_t$ and $w = u_x$. We numerically solve (6.6) for the above system via a 1st order upwind scheme in V and W. We compute expectations with a composite 2D trapezoidal rule and use centered difference scheme in x. The results, displayed in Figure 6.1, differ minimally from the true probability density function due to numerical discretization error (see Figure 6.2 for values of this error). We stress that the computational domain is larger than the plotting domain used in Figure 6.1. Equation (6.6) was solved for $-6 \leq V, W \leq 6$.

We now consider (6.9) with the following multiplicative initial noise

$$v(x,0) = \xi_v v_d^0(x) = \xi_v(\sin(x) + 2)$$
$$w(x,0) = \xi_w w_d^0(x) = \xi_w(\cos(x) + 2)$$

where ξ_v and ξ_w are independent standard normally distributed random variables. Analytically

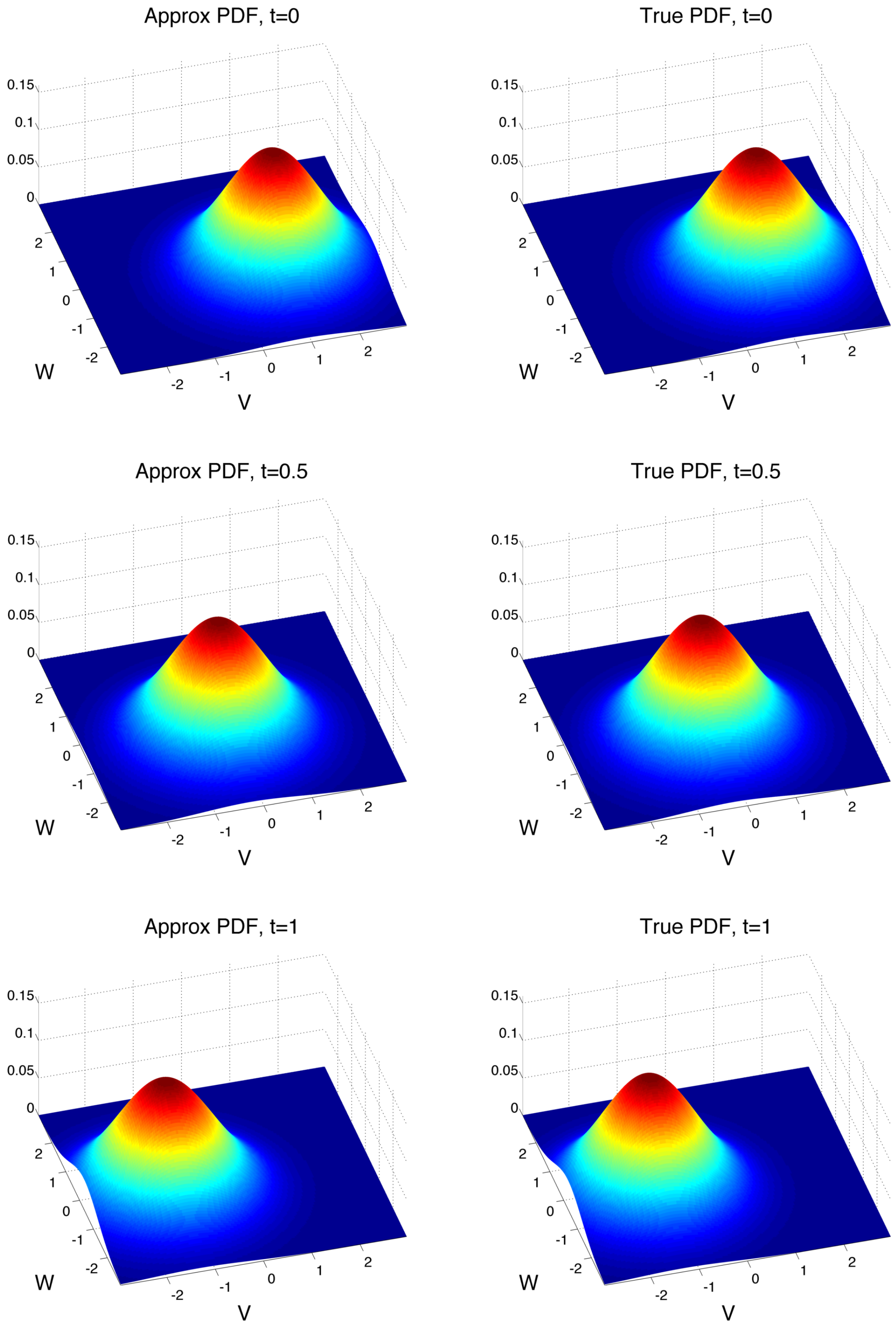

Figure 6.1: The numerical solution of (6.6) and the true PDF for (6.9) with additive initial noise at $x = 2$ for times $t = 0, 0.5$, and 1.

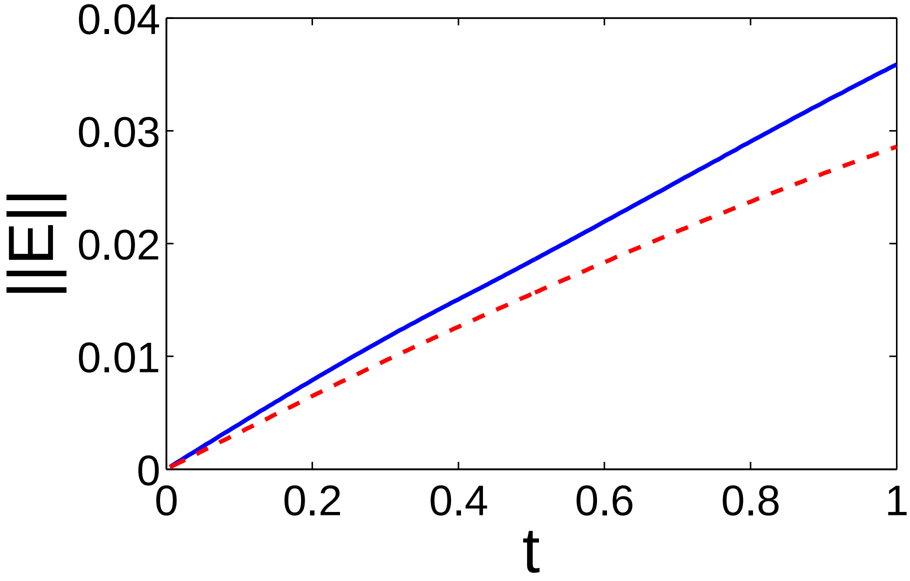

Figure 6.2: The L_2 (red, dashed line) and L_∞ (blue, solid line) norms (in V and W) of the error in the approximation of the PDF for the wave equation first order system with additive initial noise at $x = 2$ for various times.

solving for v and w gives:

$$\begin{bmatrix} v(x,t) \\ w(x,t) \end{bmatrix} = \begin{bmatrix} \frac{\xi_v}{2}(v_d^0(x+ct)+v_d^0(x-ct)) + \frac{c\xi_w}{2}(w_d^0(x+ct)-w_d^0(x-ct)) \\ \frac{\xi_v}{2c}(v_d^0(x+ct)-v_d^0(x-ct)) + \frac{\xi_w}{2}(w_d^0(x+ct)+w_d^0(x-ct)) \end{bmatrix} = B(x,t)\begin{bmatrix} \xi_v \\ \xi_w \end{bmatrix}$$

thus v and w are time and space dependent linear combinations of ξ_v and ξ_w, meaning that the joint PDF of v and w may be expressed analytically as follows:

$$\rho(x,t,V,W) = \frac{\rho_{\xi_v\xi_w}\left(B^{-1}(x,t)\begin{bmatrix} V \\ W \end{bmatrix}\right)}{|B(x,t)|} \tag{6.10}$$

where $\rho_{\xi_v\xi_w}$ is the joint PDF of ξ_v and ξ_w. $|B(x,t)|$ denotes the determinant of $B(x,t)$. In this case, $\rho_{\xi_v\xi_w}(V,W) = \rho_{\xi_v}(V)\rho_{\xi_w}(W)$ since ξ_v and ξ_w are independent. Unfortunately, as shown in Figure 6.3, the solution to the closed probability density function equation (6.6) differs considerably from the true PDF given by (6.10). Specifically, the solution to (6.6) is stationary in time since the spatial derivatives of the initial expectations of v and w are 0, since

$$\frac{\partial}{\partial x}\mathbb{E}\left[w(x,0)\right] = \frac{\partial}{\partial x}\mathbb{E}[w_d^0(x)\xi_w] = \mathbb{E}[\xi_w]\frac{\partial}{\partial x}w_d^0(x) = 0$$

$$\frac{\partial}{\partial x}\mathbb{E}\left[v(x,0)\right] = \frac{\partial}{\partial x}\mathbb{E}[v_d^0(x)\xi_v] = \mathbb{E}[\xi_v]\frac{\partial}{\partial x}v_d^0(x) = 0$$

where in the above we used $\mathbb{E}[\xi_v] = \mathbb{E}[\xi_w] = 0$. Therefore the solution to (6.6) satisfies $\frac{\partial}{\partial t}\rho = 0$. As displayed in Figure 6.3 and Figure 6.4, the true probability density function in (6.10) is *not* stationary in time. We again stress that the computational domain is larger than the plotting domain in Figure 6.3. Equation 6.6 is solved for $-15 \leq V, W \leq 15$ to ensure that it is appropriate to impose 0 boundary conditions in V and W. Although the closed probability density function equation (6.6) does a poor job of approximating the true probability density function for this problem, the means corresponding to the approximate and true probability density functions appear to be rather close (see Figure 6.3. We now show that this is not a coincidence.

Although the closed PDF equation (6.6) inaccurately propagates the joint density function of the solution, the mean corresponding to the approximate distribution appears to be correct. We show that, for any system of the form (6.4), the closed PDF equation (6.6) treats the means of the individual solution components consistently with the true PDF. To begin, multiply the closed PDF equation by U_i and integrate with respect to $U_1, ..., U_N$ over $\mathbb{R}^N$.

$$\frac{\partial \mathbb{E}[u_i]}{\partial t} - \sum_{j=1}^{N}\frac{\partial}{\partial x}\mathbb{E}[f_j(u)]\int_{\mathbb{R}^N} U_i \frac{\partial \rho}{\partial U_j} dU = -\sum_{j=1}^{N}\int_{\mathbb{R}^N} U_i \frac{\partial(\rho g_j(U))}{\partial U_j} dU$$

assuming ρ decays sufficiently fast to 0 as $|U_i| \to \infty$ for all i, integrating by parts shows that the above equation reduces to

$$\frac{\partial \mathbb{E}[u_i]}{\partial t} + \frac{\partial \mathbb{E}[f_i(u)]}{\partial x} = \mathbb{E}[g_i(u)]$$

this is precisely the equation one obtains by taking the expectation of the original balance law (6.4). Thus, although the probability density function equation with the simple closure, (6.6), does not provide a good pointwise approximation of the probability density function, it may evolve the means of the random solution *exactly* for general nonlinear 1st order systems with smooth solutions (to formally prove this fact would require a well-posedness result for the closed equation, which we have not established). We mention that this analysis only applies to deterministic f and g. Systems of balance laws with random fluxes and right hand sides may not have this property.

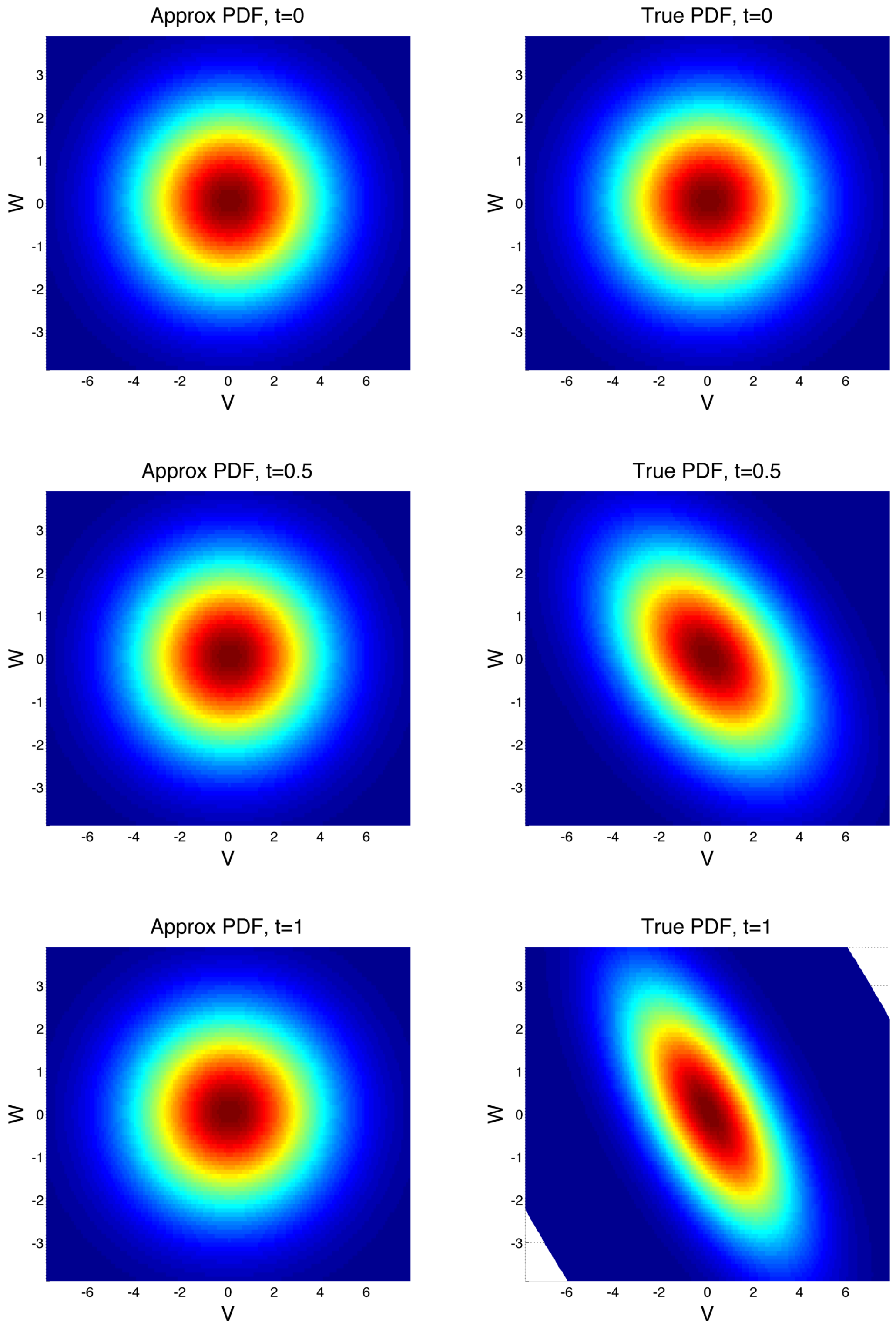

Figure 6.3: The numerical solution of (6.6) and the true PDF for (6.9) with multiplicative initial noise at $x = 2$ for $t = 0, 0.5, 1$.

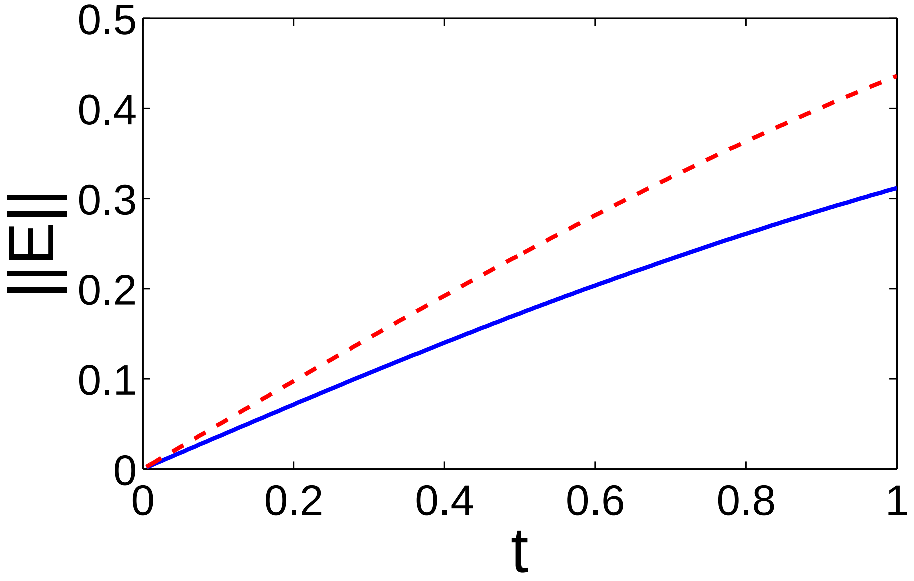

Figure 6.4: The L_2 (red, dashed line) and L_∞ (blue, solid line) norms (in V and W) of the error in the approximation of the PDF for the wave equation first order system with multiplicative initial noise at $x = 2$ for various times.

Higher order moments are not treated properly by this closed PDF equation. Values of $\mathbb{E}[u_i^2]$ predicted by the closed PDF equation evolve according to

$$\frac{\partial \mathbb{E}[u_i^2]}{\partial t} - \sum_{j=1}^{N} \frac{\partial}{\partial x}\mathbb{E}[f_j(u)] \int_{\mathbb{R}^N} U_i^2 \frac{\partial \rho}{\partial U_j} dU = -\sum_{j=1}^{N} \int_{\mathbb{R}^N} U_i^2 \frac{\partial \rho g_j(U)}{\partial U_j} dU$$

we obtained the above equation by multiplying (6.6) by U_i^2 and integrating with respect to $U_1, ..., U_N$ over $\mathbb{R}^N$. Assuming ρ decays to 0 sufficiently fast as $|U_i| \to \infty$ for all i, integrating the above equation by parts gives

$$\frac{\partial \mathbb{E}[u_i^2]}{\partial t} + 2\mathbb{E}[u_i] \frac{\partial}{\partial x} \mathbb{E}[f_i(u)] = 2\mathbb{E}[u_i g_i(u)] \tag{6.11}$$

However, multiplying the ith equation of the original system (6.4) by $2u_i$ and taking the expectation gives

$$\frac{\partial \mathbb{E}[u_i^2]}{\partial t} + 2\mathbb{E}[u_i \frac{\partial}{\partial x} f_i(u)] = 2\mathbb{E}[u_i g_i(u)]$$

equivalently,

$$\frac{\partial \mathbb{E}[u_i^2]}{\partial t} + 2\mathbb{E}[u_i]\frac{\partial}{\partial x}\mathbb{E}[f_i(u)] + 2\mathrm{Cov}\left(u_i, \frac{\partial}{\partial x}f_i(u)\right) = 2\mathbb{E}[u_i g_i(u)] \tag{6.12}$$

where $\mathrm{Cov}(X, Y)$ denotes the covariance of X and Y. An examination of the equation governing the true evolution of $\mathbb{E}[u_i^2]$, (6.12), and the associated moment evolution equation (6.11) derived from the closed PDF equation (6.6) reveals that the closed PDF equation inaccurately evolves these higher order moments. Equations (6.11) and (6.12) provide insight as to why the closed PDF equation is exact for additive, spatially constant noise, since $\frac{\partial}{\partial x}f(u)$ is deterministic and thus the covariance term in (6.12) is 0, meaning (6.12) and (6.11) agree exactly.

Unfortunately, this inaccuracy in the evolution of the second order moments is unlikely to be fixed by simply improving the quality of the closure approximation. The reason is that a single closed evolution equation for $\rho(x, t, V, W)$ cannot exist. To show this, we consider the 1st order constant coefficient system corresponding to the wave equation (6.9) with general random initial data:

$$v(x, 0, \omega) = v_0(x, \omega)$$
$$w(x, 0, \omega) = w_0(x, \omega)$$

the solution can be written down analytically in terms of v_0 and w_0:

$$v(x, t, \omega) = \frac{1}{2}(v_0(x + ct, \omega) + v_0(x - ct, \omega)) + \frac{c}{2}(w_0(x + ct, \omega) - w_0(x - ct, \omega)) \tag{6.13}$$

$$w(x, t, \omega) = \frac{1}{2c}(v_0(x + ct, \omega) - v_0(x - ct, \omega)) + \frac{1}{2}(w_0(x + ct, \omega) + w_0(x - ct, \omega)) \tag{6.14}$$

The distribution of v and w is *not* determined uniquely by the initial pointwise distributions of v_0 and w_0. For example, determining the distribution of $v(x, t)$ would require, among other things, the *joint* distribution of $v_0(x + ct, \omega)$ and $v_0(x - ct, \omega)$. This spatial correlation information is entirely unaccounted for by the pointwise probability density function of v_0, meaning that a closed equation for the time evolution of the joint probability density function of v and w does not exist.

The following two examples illuminate the concern highlighted in the previous paragraph. First, we consider the following random initial data for v and w:

$$v(x, 0) = \begin{cases} \xi & x > 0 \\ -\xi & x < 0 \end{cases}, \qquad w(x, 0) = \begin{cases} \eta & x > 0 \\ -\eta & x < 0 \end{cases}$$

where $\xi, \eta \sim \mathcal{N}(0,1)$ and ξ and η are independent. We consider solutions to (6.9) with this initial data at for $t = 1, -2 < x < 2$ with $c = 2$. For such values of x and $t, x - ct < 0$ and $x + ct > 0$, so $v(x,1) = 2\eta \sim \mathcal{N}(0,4)$ and $w(x,1) = \xi/2 \sim \mathcal{N}(0, \frac{1}{4})$.

If we prescribed $v(x,0) = \xi$, $w(x,0) = \eta$, with ξ and η still $\mathcal{N}(0,1)$, the initial joint PDF of the solution would be identical to the above example. However, the joint PDF in this example remains constant with respect to time, in stark contrast to the above example. Therefore, there is *no single closed evolution equation* for the joint PDF of v and w in this first order system. These arguments suggest that the only hope for deriving closed PDF equations for first order systems is to include spatial correlation information in the PDF evolution criteria.

6.1.3 Hyperbolic Conservation Laws

A system of conservation laws in one space dimension refers to a system of first order partial differential equations of the following form [47]:

$$\begin{aligned} \partial_t u + \partial_x f(u) &= 0, \qquad\qquad x \in \mathbb{R}, t > 0 \\ u(x,t) &= u_0(x) \end{aligned} \tag{6.15}$$

where $f : \mathcal{U} \subset \mathbb{R}^d \to \mathbb{R}^d$, u_0 denotes the initial data prescribed at $t = 0$. The system (6.15) is termed *hyperbolic* if the Jacobian matrix of f has d real eigenvalues and a basis of eigenvectors for any u. Hyperbolic conservation laws are mathematically noteworthy in that that globally smooth solutions usually do not exist, even for smooth initial data. However, a rigorous existence-uniqueness theory exists for weak (non-smooth and often discontinuous) solutions to (6.15) for the scalar case ($d = 1$) and for certain types of systems [47]. These equations arise in a variety of areas, such as gas dynamics [20], magneto-hydrodynamics [25], nonlinear elasticity [25], and traffic flow [41].

The peculiar nature of this family of equations complicates the task of uncertainty quantification for conservation laws with random inputs. For instance, polynomial chaos methods typically use a globally defined set of orthogonal polynomials to approximate the solution u. When u is discontinuous, this method of approximation converges slowly and suffers from well-known Gibbs' oscillations. These oscillations can have catastrophic consequences for conservation laws. For instance, a component of u could be a physical quantity such as density and the form of f may have components that require this density to be positive (such as a square root), and Gibbs' oscillations could inadvertently cause this density to be negative. This issue spurred the development of the Intrusive Polynomial Moment Method [68], which is a Polynomial Chaos-like method which utilizes a nonlinear projection of u to bound the components of u within certain ranges. Although it does achieve this goal, it requires repeated costly optimizations that limit its usefulness. Alternative methods for uncertainty quantification for conservation laws include Multi-Level Monte Carlo Methods [54], Multi-Element Polynomial Chaos [96], and iterative stochastic spectral representations [69].

We now investigate the possibility of developing a closed equation for the evolution of the random solution to a scalar conservation law in one space dimension with random initial data:

$$\partial_t u(x,t,\omega) + \partial_x f(u(x,t,\omega)) = 0, \qquad x \in \mathbb{R}, t > 0 \tag{6.16}$$

$$u(x,t,\omega) = u_0(x,\omega) \tag{6.17}$$

where $\omega \in \Omega$ with Ω being the sample space of some probability space $(\Omega, \mathcal{F}, P)$. If the solutions u are smooth, then the probability density function $\rho_u(U,x,t)$ satisfies the following simplified form of (6.3).

$$\frac{\partial \rho_u}{\partial t} + f'(U)\frac{\partial \rho_u}{\partial x} + f''(U)\frac{\partial}{\partial x}\int_{-\infty}^{U} \rho_u(U',x,t)\,dU' = 0$$

in this case, we may integrate the above equation with respect to U to obtain an equation for the cumulative distribution function of $u(x,t,\omega)$, which we denote $F_u(U,x,t)$:

$$\frac{\partial F_u}{\partial t} + f'(U)\frac{\partial F_u}{\partial x} = 0 \tag{6.18}$$

$$F_u(U,x,0) = \mathcal{P}(u_0(x,\omega) \le U) \tag{6.19}$$

Equation (6.18) implies that the CDF for a smooth solution to a *nonlinear* scalar conservation law with random initial data obeys a family of *linear* advection equations parameterized by a, which may be solved analytically. To further illustrate the advantages that this CDF approach enjoys over alternative methods for uncertainty quantification, we consider Burgers' equation with random sinusoidal initial data (6.20), (6.21) whose solutions are smooth for $t < 1$:

$$\partial_t u + \partial_x\left(\frac{1}{2}u^2\right) = 0, \qquad x \in \mathbb{R}, t \ge 0 \tag{6.20}$$

$$u(x,t=0,\xi) = u_0(x,\xi) = \sin(x) + \xi \qquad \xi \sim \mathcal{U}(0,1) \tag{6.21}$$

Methods such as Polynomial Chaos and Monte Carlo sampling require one to solve Burgers' equation multiple times with varying values of ξ to generate a probabilistic description of u. Unfortunately, unlike the CDF equation, (6.20), (6.21) only admits an implicitly defined

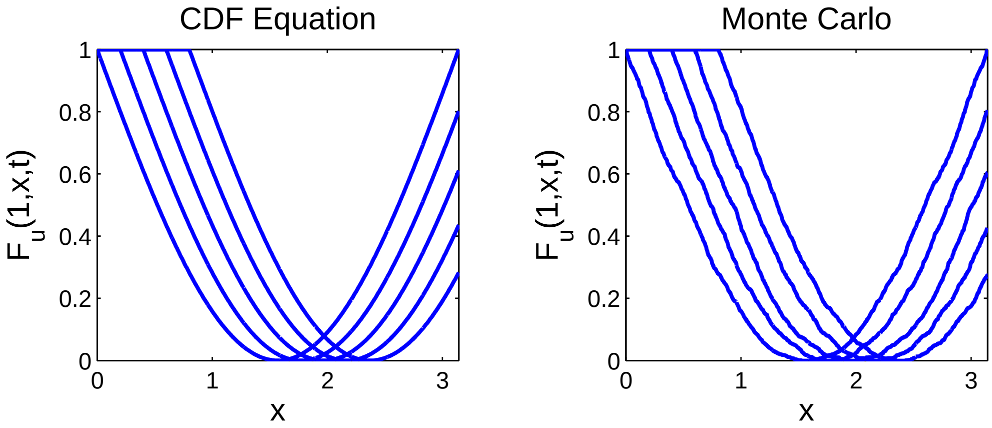

Figure 6.5: Time evolution of the CDF of the solution (6.20), (6.21) at $t = 0, 0.2, 0.4, 0.6$, and 0.8 as computed from (6.18), left, and Monte Carlo simulation with 1000 realizations of ξ, right. Solutions for Monte Carlo are obtained by solving (6.22)

solution:

$$u = \sin(x - tu) + \xi \tag{6.22}$$

Therefore, to solve Burgers' equation once, one must solve the nonlinear equation (6.22), which would likely be done numerically. Furthermore, for Polynomial Chaos and Monte Carlo sampling, one must solve this nonlinear equation *many* times and then use this ensemble of solutions to obtain an *approximate* probabilistic description of u. Alternatively, when using the CDF equation, one need only solve (6.18) *once* to obtain an *exact* value of the probability that $u(x, t, \omega) \leq U$. This benefit is apparent in Figure 6.5, which displays snapshots of the evolution of $F_u(1, x, t)$ computed from the CDF equation, as well as Monte Carlo sampling with 1000 realizations. Due to the linearity of the CDF equation, it may be solved analytically with ease. Furthermore, this solution of the CDF equation provides an analytic description of the CDF, which yields insights into the time-evolution of the CDF that are not possible from Polynomial Chaos or Monte Carlo methods.

Unfortunately, this CDF equation is incorrect for non-smooth solutions, which is not surprising as the smoothness of u was used in the derivation of this equation. Due to the ubiquity of non-smooth solutions to nonlinear scalar conservation laws, the usefulness of the CDF equation (6.18) is limited. For an example of the failure of this CDF equation for non-smooth solutions, we consider Burgers' equation with the following random Riemann initial data

$$u(x,0,\xi) = \begin{cases} \xi \sim \mathcal{U}(0,1) & x < 0 \\ 0 & x > 0 \end{cases}$$

The associated stochastic solution for $t > 0$ is a shock traveling with random speed $s = \xi/2$.

$$u(x,t,\xi) = \begin{cases} \xi \sim \mathcal{U}(0,1) & x < s(\xi)t \\ 0 & x > s(\xi)t \end{cases}$$

The CDF of this random solution, which does not satisfy the CDF equation (6.18), is (for $0 \leq U \leq 1$)

$$F_u(U,x,t) = \begin{cases} U & x < Ut/2 \\ 2x/t & Ut/2 < x < t/2 \\ 1 & t/2 < x \end{cases}$$

The above formula for F_u was derived by considering the regions $x \leq 0$, $0 < x < Ut/2$, $Ut/2 < x < t/2$, and $t/2 < x$ individually.

We now consider two examples that suggest that the closed evolution equations for the evolution of the pointwise CDF of *any* kind do not exist for non-smooth solutions to scalar conservation laws in general. First we consider Burgers' equation with the following random

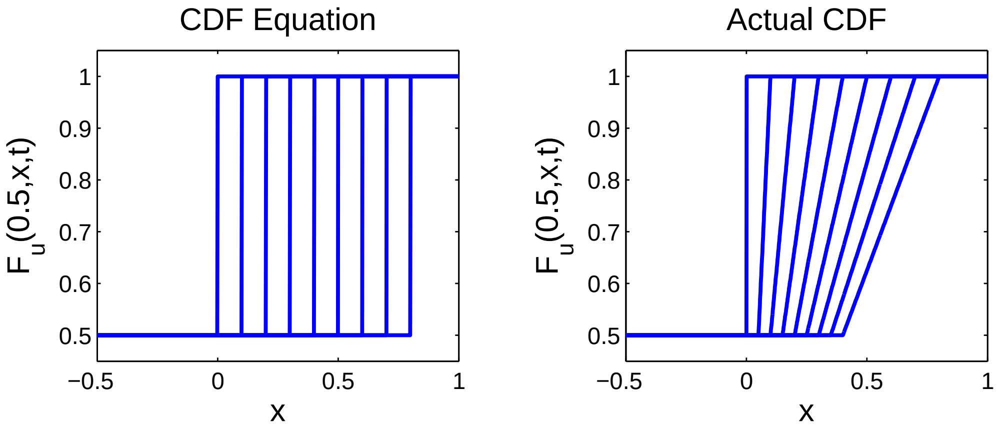

Figure 6.6: Time evolution of the CDF, right, and the solution to (6.18), left, for Burgers' equation with a random shock at $t = 0, 0.2, ..., 1.6$

Riemann initial data:

$$u(x,0,\xi) = \begin{cases} \xi & x < 0 \\ -\xi & x > 0 \end{cases}$$

where ξ is uniformly distributed between 0 and 1. The solution corresponding to this initial data is a shock moving with speed 0, which implies that the CDF of u is constant in time:

$$F_u(U,x,t) = \begin{cases} \mathbb{1}_{[0,1]}(U) & x < 0 \\ \mathbb{1}_{[-1,0]}(U) & x > 0 \end{cases}$$

where $\mathbb{1}$ denotes the indicator function. We now consider Burgers' equation with the following initial data:

$$u(x,0,\eta,\gamma) = \begin{cases} \eta & x < 0 \\ \gamma & x > 0 \end{cases}$$

where η is uniformly distributed between 0 and 1, γ is uniformly distributed between -1 and 0, and η and γ are independent. Notice that the initial CDF of u is identical to the above example. The associated stochastic solution is:

$$u(x,t,\eta,\gamma) = \begin{cases} \eta & x < s(\eta,\gamma)t \\ \gamma & x > s(\eta,\gamma)t \end{cases}$$

The solution is a shock since $\eta > \gamma$ for all possible realizations of these variables, and the shock speed $s = (\eta+\gamma)/2$ by the Rankine-Hugoniot condition. Unlike the first example, the CDF for this problem is *not* constant in time. For instance, for first example $F_u(0,1,4) = 1$ since $u(1,4,\omega) = -\xi < 0$ for all realizations of ξ. However, for the current example we have that $u(x,t,\omega) \leq 0$ if and only if $u(x,t,\omega) = \gamma$, so

$$F_u(0,1,4) = \mathcal{P}\left(1 > 4s(\eta,\gamma)\right) = \mathcal{P}\left(\eta + \gamma \leq \frac{1}{2}\right) = 1 - \int_{1/2}^{1}\int_{1/2-\eta}^{0} d\gamma d\eta = 7/8.$$

These two examples show that the initial CDF alone is inadequate to determine the stochastic properties of the solution for future times. Therefore, unlike the smooth case, there does not exist a single closed evolution equation for the CDF of non-smooth solutions to scalar conservation laws in general.

6.2 Conclusions

PDF equations are a powerful tool for understanding the propagation of uncertainty for scalar first order equations subject to random inputs. Unfortunately, our arguments in this section show that it is impossible to derive a single closed equation for the evolution of the PDF of stochastic solutions to systems of hyperbolic balance laws. Additionally, we showed that such an equation does not exist for non-smooth solutions to scalar conservation laws.

The reason for this difficulty is that the evolution of PDFs for such problems is dependent on more than the simple pointwise PDF of the stochastic solution. Specifically, the evolution of the uncertainty in the solution depends on spatial correlation information that is not accounted for by the pointwise PDF. This cause of failure provides motivation for an alternative approach, which is to alter the definition of Π to include such correlation information. For example, we could define Π as

$$\Pi(U, x, t, U', x', t') \triangleq \delta(U - u(x,t))\delta(U' - u(x', t')).$$

A similar form of Π was considered in [93] to treat second order scalar equations. The expectation of Π defined above would now be the joint PDF of $u(x,t)$ and $u(x',t')$. It may be possible to derive evolution equations for this distribution. Such evolution equations would provide richer statistical information than the simple pointwise PDF, and would also provide a new method for uncertainty quantification for blood flow models and other phenomena governed by first order hyperbolic systems. As discussed in Section 6.1, this method would be particularly efficient to handle the large number of uncertainties associated with these blood flow models.

Chapter 7

Conclusions

The structured tree boundary condition provides a physiologically based, yet computationally cheap, alternative to outflow boundary conditions such as the Windkessel and pure resistor. Our derivation of the generalized structured tree in Chapter 4 removes the temporal periodicity restriction present in the original structured tree, meaning that the structured tree can now be used to model all flow regimes. This generalized condition also exhibits better numerical convergence properties, even for simulations that are periodic in time. Additionally, we showed that the original structured tree is an approximation of this generalized condition, which means that it may be justified to apply the original structured tree, unaltered, to non-periodic simulations.

Another advantage of the structured tree is that its parameters may be directly measured due to their physiological nature. The structured tree thus has the potential to allow for reasonable simulation results *without* parameter calibration procedures. In order to avoid such calibration procedures, we closely examined the geometry of trees of small arteries and the mechanical properties of blood flow in these trees to determine a physiologically appropriate set of structured tree parameters. We then proposed a single set of parameters that incorporated tiered branching structures, non-continuum effects of blood flow in the arterioles and capillaries, and a nonzero terminal impedance. We found that using this single set of parameters for all outlets yielded physiologically reasonable results in a simulation of the full systemic arterial tree. However, these parameters yielded non-physiological results in simulations of the Circle of Willis.

One possible explanation for our inability to avoid calibration altogether is that our study of branching properties of arterial trees was not detailed enough. It may be possible to avoid calibration by incorporating organ specific properties of arterial trees. These trees are constrained by the particular shape of the organ that they inhabit, and different organ shapes may induce different tree branching properties. In addition to measured data, it may be possible to determine these organ specific properties by performing a constrained constructive optimization procedure to grow “optimal” trees within various organ geometries. Such a procedure has already been performed by Karch et. al [44] to study the structure of the arterial tree between the epi- and endocardial layers of the human heart.

REFERENCES

[1] D J Acheson. *Elementary Fluid Dynamics.* Oxford University Press, 1990.

[2] J. Alastruey, A. W. Khir, K. S. Matthys, P. Segers, S.J. Sherwin, P.R. Verdonck, K.H. Parker, and J. Peiro. Pulse wave propagation in a model human arterial network: Assessment of 1-d visco-elastic simulations against in vitro measurements. *Journal of Biomechanics*, 44:2250–2258, 2011.

[3] J. Alastruey, K.H. Parker, J. Peiró, S.M. Byrd, and S.J. Sherwin. Modeling the circle of willis to assess the effects of anatomical variations and occlusions on cerebral flows. *J. Biomech.*, 40:1794–1805, 2007.

[4] J. Alastruey, K.H. Parker, J. Peiro, and S.J. Sherwin. Lumped parameter outflow models for 1-d blood flow simulations: effect on pulse waves and parameter estimation. *Common. Comput. Phys.*, 4(2):317–336, 2008.

[5] J. Alastruey, T. Passerini, L. Formaggia, and J. Perio. Physical determining factors of the arterial pulse waveform: theoretical analysis and calculation using the 1-d formulation. *J. Eng. Math*, 2012.

[6] B. Alpers, J. Berry, and R. Paddison. Anatomical studies of the circle of willis in the normal brain. *AMA Arch Neurol Psychiatry*, 81:409–418, 1959.

[7] T. Arts, P.H.M. Bovendeerd, F.W. Prinzen, and R.S. Reneman. Relation between left ventricular cavity pressure and volume and systolic fiber stress and strain in the wall. *Biophys J.*, 59:93–102.

[8] T. Arts, R.T.I. Kruger, W. van Gerven, J.A.C. Lambregts, and R.S. Reneman. Propagation velocity and reflection of pressure wave in the canine coronary artery. *Am J Physiol Heart Circ Physiol*, 237:H469–H474, 1979.

[9] K. Azer and C.S. Peskin. A one-dimensional model of blood flow in arteries with friction and convection based on the womersley velocity profile. *Cardiovascular Eng*, 7:51–73, 2007.

[10] J.H. Barbee and G.R. Cokelet. Prediction of blood flow in tubes with diameters as small as 29 microns. *Microvasc. Res.*, 3:17–21, 1971.

[11] R. Bhatia. *Fourier Series.* The Mathematical Association of America, 2005.

[12] P.H. Bovendeerd, P. Borsje, T. Arts, and F.N. van de Vosse. Dependence of intramyocardial pressure and coronary flow on ventricular loading and contractility: a model study. *Ann. Biomed. Eng*, 34:1833–1845.

[13] J. P. Boyd. *Chebyshev and Fourier Spectral Methods.* Dover, Mineola, NY, 2 edition, 2001.

[14] W. L. Briggs. *The DFT: An Owner's Manual for the Discrete Fourier Transform.* SIAM, Philadelphia, 1995.

[15] J. Broderick, T. Brott, R. Kothari, R. Miller, J. Khoury, and A. Pancioli. The greater cincinnati/northern kentucky stroke study: preliminary first-ever and total incidence rates of stroke among blacks. *Stroke*, 29:415–421, 1998.

[16] R.E. Caflisch. Monte carlo and quasi-monte carlo methods. *Acta Numerica*, pages 1–49, 1998.

[17] C. Canuto, M. Y. Hussaini, A. Quarteroni, and T. A. Zang. *Spectral Methods in Fluid Dynamics.* Springer-Verlag, 1988.

[18] C.G. Caro, T.J. Pedley, R.C. Schroter, and W.A. Seed. *The Mechanics of the Circulation.* Cambridge University Press, New York, 2012.

[19] P. Chen, A. Quarteroni, and G. Rozza. Uncertainty quantification of human arterial network. *MATHICSE Technical Report*, Nr. 42.2012, 2012.

[20] A.J. Chorin and J.E. Marsden. *A Mathematical Introduction to Fluid Mechanics.* Springer, 3 edition, 1993.

[21] R.B. Clipp and B.N. Steele. Impedance boundary conditions for the pulmonary vasculature including the effects of geometry, compliance, and respiration. *IEEE Trans. Biomed. Eng.*, 56:862–870, 2009.

[22] W. Cousins and P.A. Gremaud. Boundary conditions for hemodynamics: The structured tree revisited. *Journal of Computational Physics*, 231:6086–6096, 2012.

[23] W. Cousins, P.A. Gremaud, and D. M. Tartakovsky. A new physiological boundary condition for hemodynamics. *Accepted–SIAM Journal on Applied Mathematics*, 2013.

[24] L.G.E. Cox, S. Loerakker, M.C.M Rutten, B.A.J.M de Mol, and F.N. van de Vosse. A mathematical model to evaluate control strategies for mechanical circulatory support. *Artif. Organs*, 33:593–603.

[25] C.M. Dafermos. *Hyperbolic Conservation Laws in Continuum Physics.* Springer, 2009.

[26] K. DeVault, P.A. Gremaud, V. Novak, M.S. Olufsen, G. Vernieres, and P. Zhao. Blood flow in the circle of willis: Modeling and calibration. *Multiscale Modeling and Simulation: a SIAM Interdisciplinary Journal*, pages 888–909, 2008.

[27] K.J. DeVault. Numerical study of two problems in fluid flow: Cavitation and cerebral circulation. *Ph.D. Thesis, North Carolina State University*, 2008.

[28] R. Fahraeus and T. Lindqvist. The viscosity of blood in narrow capillary tubes. *Am J Physiol - Legacy Content*, 96, Issue 3:562–568, 1931.

[29] D.A. Fedosov, B. Caswell, A.S. Popel, and G.E. Karniadakis. Blood flow and cell-free layer in micro vessels. *Microcirculation*, 17(8):615–628, 2010.

[30] L. Formaggia, D. Lamponi, and A. Quarteroni. One-dimensional models for blood flow in arteries. *Journal of Engineering Mathematics*, 47:251–276, 2003.

[31] L. Formaggia, D. Lamponi, M. Tuveri, and A. Veneziani. Numerical modeling of 1d arterial networks coupled with a lumped parameter description of the heart. *Comput. Methods Biomech. Biomed. Eng.*, 9(5):273–288, 2006.

[32] V. E. Franke, K.H. Parker, L. Y. Wee, N. M. Fisk, and S.J. Sherwin. Time domain computational modelling of 1d arterial networks in monochrionionic placentas. *ESAIM: Mathematical Modelling and Numerical Analysis*, 37(4):557–580, 2003.

[33] P Gahtgens, C Duhrssen, and K.H. Albrecht. Motion, deformation, and interaction of blood cells and plasma during flow through narrow capillary tubes. *Blood Cells*, 6:799–812, 1980.

[34] Walter Gautschi. *Numerical Analysis: An Introduction.* Birkhauser, Boston, 1997.

[35] L. Grinberg, T. Anor, E. Cheever, J.R. Madsen, and G.E. Karniadakis. Simulation of the human intracranial arterial tree. *Phil. Trans. R. Soc.*, 367:2371–2386, 2009.

[36] L. Grinberg and G.E. Karniadakis. Outflow boundary conditions for arterial networks with multiple outlets. *Annals of Biomedical Engineering*, 36, No. 9:1496–1514, 2008.

[37] B.B. Gupta and V. Seshadri. Flow of red blood cell suspensions through narrow tubes. *Biorheology*, 14:133–143, 1977.

[38] G. Halikas and C.W. Sheppard. The viscosity of water and of blood in small diameter capillary tubes. anomalous viscosity of blood. *Biorheology*, 6:137–142, 1969.

[39] J. S. Hesthaven, S. Gottlieb, and D. Gottlieb. *Spectral Methods for TIme Dependent Problems.* Cambridge University Press, Cambridge, 2007.

[40] A.W.J. Hoksbergen, C.B.L. Majoie, F.J.H. Hulsmans, and D.A. Legemate. Assessment of collateral function of the circle of willis: three-dimensional time-of-flight mr angiography compared with transcranial color-coded duplex sonography. *American Journal of Neuroradiology*, 24:456–462, 2003.

[41] H. Holden and N.H. Risebro. A mathematical model of traffic flow on a network of unidirectional roads. *SIAM J. Math. Anal*, 26(4):997–1017, 1995.

[42] Y Huo and G.S. Kassab. Intraspecific scaling laws of vascular trees. *Journal of the Royal Society Interface*, 9:190–200, 2012.

[43] G. Kalsho and G.S. Kassab. Bifurcation asymmetry of the porcine coronary vasulature and its implications on coronary flow heterogeneity. *Am J Physiol Heart Circ Physiol*, 287:H2493–H2500, 2004.

[44] R. Karch, F. Neumann, M. Neumann, and W. Schreiner. Staged growth of optimized arterial model trees. *Annals of biomedical engineering*, 28:495–511, 2000.

[45] G.E. Karniadakis and D. Venturi. New evolution equations for the joint response-excitation probability density function of stochastic solutions to first order nonlinear pdes. *Journal of Computational Physics*, 231:7450–7474, 2012.

[46] C.T. Kelley. *Iterative Methods for Linear and Nonlinear Equations.* SIAM, Philadelphia, 1995.

[47] P. LeFloch. *Hyperbolic systems of conservation laws : the theory of classical and nonclassical shock waves.* Birkhuser Verlag, Basel Boston, 2002.

[48] C. Lubich. Convolution quadrature and discretized operational calculus. I. *Numer. Math.*, 52(2):129–145, 1988.

[49] C. Lubich. Convolution quadrature and discretized operational calculus. II. *Numer. Math.*, 52(4):413–425, 1988.

[50] Ch. Lubich. On the multistep time discretization of linear initial-boundary value problems and their boundary integral equations. *Numer. Math.*, 67(3):365–389, April 1994.

[51] M. Malve, A. Perez del Palomar, S. Chandra, J.L. Lopez-Villalobos, A. Mena, E. A. Finol, A. Ginel, and M.Doblare. Fsi analysis of a healthy and a stenotic human trachea under impedance-based boundary conditions. *Journal of Biomechanical Engineering*, 133, 2011.

[52] A.L. Marsden, I.E. Vignon-Clementel, F.P. Chan, J.A. Feinstein, and C.A. Taylor. Effects of exercise and respiration on hemodynamic efficiency in cfd simulations of the total cavopulmonary connection. *Annals of Biomedical Engineering*, 35(2):250–263, 2007.

[53] K.S. Matthys, J. Alastruey, J Perio, A.W. Khir, P. Segers, P. R. Verdonck, K.H. Parker, and S.J. Sherwin. Pulse wave propagation in a model human arterial network: Assessment of 1-d numerical simulations against in vitro measurements. *Journal of Biomechanics*, 40:3476–3486, 2007.

[54] S. Mishra, Ch. Schwab, and J. Sukys. Multi-level monte carlo finite volume methods for nonlinear systems of conservation laws in multi-dimensions. *Journal of Computational Physics*, 231(8):3365–3388, 2012.

[55] S. Moore, T. David, J.G. Chase, J. Arnold, and J. Fink. 3d models of blood flow in the cerebral vasculature. *Journal of Biomechanics*, 39:1454–1463, 2006.

[56] S.M. Moore, K.T. Moorhead, J.G. Chase, T. David, and J. Fink. One-dimensional and three-dimensional models of cerebrovascular flow. *Journal of Biomechanical Engineering*, 127(3):440–449, 2005.

[57] C.D. Murray. The physiological principle of minimum work applied to the angle of branching of arteries. *Journal of General Physiology*, 9(6):835–841, 1926.

[58] C.D. Murray. The physiological principle of minimum work I: The vascular system and the cost of blood volume. *Proceedings of the National Academy of Sciences of the United States of America*, 12, No. 3:207–214, 1926.

[59] J.P. Mynard and P. Nithiarasu. A 1d arterial blood flow model incorporating ventricular pressure, aortic valve and regional coronary flow using the locally conservative galerkin (lcg) method. *Communications in Numerical Methods in Engineering*, 24:367–417, 2008.

[60] N. Stergiopulos and B.E. Westerhof and N. Westerhof. Total arterial inertance as the fourth element of the windkessel model. *Am J Physiol Heart Circ Physiol*, 276:H81–H88, 1999.

[61] D. A. Nordsletten, S. Blackett, M. D. Bentley, E.L. Ritman, and N.P. Smith. Structural morphology of renal vasculature. *Am J Physiol Heart Circ Physiol*, 291:H296–H309, 2006.

[62] M.S. Olufsen. Modeling the arterial system with reference to an anesthesia simulator. *Ph.D. Thesis. Roskilde University, Denmark*, 1998.

[63] M.S. Olufsen. Structured tree outflow condition for blood in the larger systemic arteries. *Am. J. Physiol.*, 276 (Heart Circ. Physiol. 45):H257–H268, 1999.

[64] M.S. Olufsen, C.S. Peskin, W.Y. Kim, E.M. Pederson, A. Nadim, and J. Larsen. Numerical simulation and experimental validation of blood flow in arteries with structured-tree outflow conditions. *Annals of Biomedical Engineering*, 28:1281–1299, 2000.

[65] F. Perren P. Reymond, F. Lazeyras, and N. Stergiopolus. Patient-specfic mean pressure drop in the systemic arterial tree, a comparison between 1-d and 3-d models. *Journal of Biomechanics*, 45:2499–2505, 2012.

[66] T.J. Pedley. *The Fluid Mechanics of Large Blood Vessels.* Cambridge University Press, 1980.

[67] J.V. Moloney P.O. Kano, M Brio. Application of weeks method for the numerical inversion of the laplace transform to the matrix exponential. *Comm Math Sci*, 3 (3):335–372, 2005.

[68] G Poette, B Despres, and D. Lucor. Uncertainty quantification for systems of conservation laws. *Journal of Computational Physics*, 228:2443–2467, 2009.

[69] G Poette and D. Lucor. Non-intrustive iterative stochastic spectral representation with application to compressible gas dynamics. *Journal of Computational Physics*, 231:3587–3609, 2012.

[70] A. R. Pries, D. Neuhaus, and P. Gaehtgens. Blood viscosity in tube flow: dependence on diamter and hematocrit. *Am. J. Physiol*, 263 (Heart Circ. Physiol. 32):H1770–H1778, 1992.

[71] A. R. Pries, T. W. Secomb, T Gessner, M. B. Sperandio, J. F. Gross, and P Gaehtgens. Resistance to blood flow in microvessels in vivo. *Circulation Research*, 75:904–915, 1994.

[72] W. Reinke, P.C. Johnson, and P. Gaehtgens. Blood viscosity in small tubes: effect of shear rate, aggregation, and sedimentation. *Am. J. Physiol.*, 1987.

[73] P. Reymond, F. Merenda, F. Perren, D. Rufenacht, and N. Stergiopulos. Validation of a one-dimensional model of the systemic arterial tree. *Am J Physiol Heart Circ Physiol*, 297:H208–H222, 2009.

[74] S. Rossitti and J. Lofgren. Vascular dimensions of the cerebral arteries follow the principle of minimum work. *Stroke*, 34:371–377, 1992.

[75] K. Sagawa, M. Maughan, H Suga, and K Sunagawa. *Cardiac contraction and the pressure-volume relationship.* Oxford Univ Press, New York, 1988.

[76] S. Sankaran and A.L. Marsden. A stochastic collocation method for uncertainty quantification and propagation in cardiovascular simulations. *Journal of Biomedical Engineering*, 133, 2011.

[77] H Senzaki, C.H. Chen, and D.A. Kass. Valvular heart disease/heart failure/hypertension:single beat estimation of end-systolic pressure-volume relation in unmans: a new method with the potential for noninvasive application. *Circulation*, 94:2497–2506.

[78] S. J. Sherwin, V. Franke, J. Peiró, and K. Parker. One-dimensional modelling of a vascular network in space-time variables. *J. Engrg. Math.*, 47(3-4):217–250, 2003.

[79] S.J. Sherwin, L. Formaggia, J. Peiró, and V. Franke. Computational modeling of 1d blood flow with variable mechanical properties and its application to simulation of wave propagation in the human arterial system. *Int. J. for Num. Meth. in Fluids*, 43:673–700, 2003.

[80] J.H. Spurk. *Fluid Mechanics.* Springer, Berlin, 1997.

[81] B. N. Steele, M.S. Olufsen, and C. A. Taylor. Fractal network model for simulating abdominal and lower extremity blood flow during resting and exercise conditions. *Computer Methods in Biomechanics and Biomedical Engineering*, 10(1):39–51, 2007.

[82] B.N. Steele and C.A. Taylor. Simulation of blood flow in the abdominal aorta at rest and during exercise using a 1-d finite element method with impedance boundary conditions derived from a fractal tree. In *Proceedings of the 2003 ASME Summer Bioengineering Meeting, Key Biscayne, FL*, 2003.

[83] A. Strahler. Hypsometric (area altitude) analysis of erosional topology. *Bull Geol Soc Amer*, 63.

[84] N. Suwa, T. Niwa, H. Fukasawa, and Y. Sasaki. Estimation of intravascular blood pressure gradient by mathematical analysis of arterial casts. *Tohoku J. Exper. Med.*, 79:168–198, 1963.

[85] D. M. Tartakovsky and S. Broyda. Pdf equations for advective–reactive transport in heterogeneous porous media with uncertain properties. *Journal of Contaminant Hydrology*, 120-121:129–140, 2011.

[86] M.G. Taylor. The input impedance of an assembly of randomly branching elastic tubes. *Biophysical Journal*, 6, 1966.

[87] M.G. Taylor. Wave transmission through an assembly of randomly branching elastic tubes. *Biophys. J*, 6:697–716, 1966.

[88] R. Torii, M. Oshima, T. Kobayashi, K. Takagi, and T.E. Tezduyar. Coupling 3d fluid-structure interaction modeling of cerebral aneurysm with 0d arterial network model as boundary conditions. *Trans. Japan Soc. Simul. Tech.*, 1:81–90, 2009.

[89] L. N. Trefethen. *Spectral Methods in MATLAB.* SIAM, Philadelphia, 2000.

[90] H. B. M. Uylings. Optimization of diameters and bifurcation angles in lung and vascular tree structures. *Bulletin of Mathematical Biology*, 39, 1977.

[91] F. N. van de Vosse and N. Stergioulos. Pulse wave propagation in the arterial tree. *Annu. Rev. Fluid Mech.*, 43:467–499, 2011.

[92] E VanBavel and J.A.E. Spaan. Branching patterns in the porcine coronary arterial tree: Estimation of flow heterogeneity. *Circ Res*, 71:1200–1212, 1992.

[93] D. Venturi and G. Karniadakis. Differential constraints for the probability density function of stochastic solutions to the wave equation. *International Journal for Uncertainty Quantification*, 2011.

[94] D. Venturi, T.P. Sapsis, H. Cho, and G.E. Karniadakis. A computable evolution equation for the joint response-excitation probability density function of stochastic dynamical systems. *Proceedings of the Royal Society A*, 2011.

[95] I.E. Vignon-Clementel, C.A. Figueroa, K.E. Jansen, and C.A. Taylor. Outflow boundary conditions for three-dimensional finite element modeling of blood flow and pressure in arteries. *Comp. Meth. Appl. Mech. Eng.*, 195:29–32, 2006.

[96] X. Wan and G.E. Karniadakis. Multi-element generalized polynomial chaos for arbitrary probability measures. *SIAM J. Sci. Comput.*, 28(3):901–928, 2006.

[97] P. Wang and D.M. Tartakovsky. Uncertainty quantification in kinematic-wave models. *Journal of Computational Physics*, 231(23):7868–7880, 2012.

[98] P. Wang, D.M. Tartakovsky, Jr. K.D. Jarman, and A.M. Tartakovsky. Cdf solutions of buckley-leverett equation with uncertain parameters. *Multiscale Model. Simul.*, 1(1):118–133, 2013.

[99] P.A. Weiringa, H.G. Stassen, J.D. Laird, and J.A. Spaan. Quantification of arteriolar density and embolization by microspheres in rat myocardium. *Am J Physiol Heart Circ Physiol*, 254:H636–H650, 1988.

[100] N. Westerhof, J.W. Lankhaar, and B. E. Westerhof. The arterial windkessel. *Med Biol Eng Comput*, 47:131–141, 2009.

[101] J. R. Womersley. *An Elastic Tube Theory of Pulse Transmission and Oscillatory Flow in Mammalian Arteries*. Wright Air Development Center, Wright-Patterson Air Force Base, Ohio, 1957.

[102] D. Xiu. Fast numerical methods for stochastic computations: A review. *Communications in Computational Physics*, 5:242–272, 2009.

[103] D. Xiu and G.E. Karniadakis. The weiner-askey polynomial chaos for stochastic differential equations. *SIAM J. Sci. Comput.*, pages 619–644, 2002.

[104] D. Xiu and G.E. Karniadakis. Supersensitivity due to uncertain boundary conditions. *Int. J. Numer. Meth.*, 61:2114–2138, 2004.

[105] D. Xiu and S.J. Sherwin. Parameteric uncertainty analysis of pulse wave propagation in a model of a human arterial network. *Journal of Computational Physics*, 226:1385–1407, 2007.

[106] D. Xiu and D.M. Tartakovsky. Numerical methods for differential equations in random domains. *SIAM J. Sci. Comput*, 28(3):1167–1185, 2006.

[107] D. Xiu and D.M. Tartakovsky. Stochastic analysis of transport in tubes with rough walls. *Journal of Computational Physics*, 217(1):248–259, 2006.

[108] M. Zamir. On fractal properties of arterial trees. *J. Theor. Biol.*, 197:517–526, 1999.

[109] A.H. Zemanian. *Generalized Integral Transforms*. Interscience, 1968.

APPENDIX

Appendix A

Simulation Details

In this section, we describe the numerical approaches used to discretize the system of partial differential equations (1.4,1.5) along with the boundary conditions. We combine a backward Euler time integration scheme along with a Chebyshev collocation method in space. In Section A.0.6, we show convergence of this scheme by numerical experiment. Also, in Section A.0.6 we present a boundary condition validation experiment showing that the structured tree condition is satisfied, a fact that is not obvious due to its convoluted implementation (see Section 3.2.1). All computations were performed using MATLAB® (2011a, The MathWorks, Natick, Massachusetts, U.S.A.). All computations were performed on a MacBook Pro laptop with a 3.06 GHz Intel Core 2 Duo processor.

A.0.1 Spatial Discretization

We use a Chebyshev collocation method to approximate the spatial derivatives of the system of partial differential equations governing A and P. The idea of a collocation method is to construct an interpolant approximation of the solution that satisfies the partial differential equation exactly at the interpolation points. Chebyshev collocation methods use a global polynomial interpolant with the Chebyshev nodes $x_j = \cos(j\pi/N), j = 0, ..., N$ serving as the interpolation nodes for a degree N interpolant. These nodes correspond to the interval $[-1, 1]$; arbitrary intervals can be handled by a trivial linear map of $[-1, 1]$ to the desired interval. For instance, we work in the region $x \in [0, L]$, where L is the length of a particular vessel.

When the underlying function is smooth, Chebyshev collocation is computational efficient and has low storage requirements since it delivers high accuracy with a small number of spatial nodes[13, 17, 39, 89]. This fact is also clear from our numerical convergence study in Appendix A.0.6. We illustrate this method by deriving a Chebyshev collocation semidiscretization of the following advection equation:

$$\begin{aligned}
\partial_t u(t,x) + \partial_x u(t,x) &= 0, && x \in [-1,1], t > 0 \\
u(0,x) &= f(x), && x \in [-1,1] \\
u(t,-1) &= g(t) && t > 0
\end{aligned}$$

The formula for this interpolant approximation is

$$u(x,t) \approx U_N(x,t) = \sum_{i=0}^{N} u_i(t)\ell_i(x)$$

where x_j is the jth Chebyshev node. $u_i(t)$ is an approximation of $u_i(x_j)$ and $\ell_i(x_j) = \delta_{ij}$ are the Lagrange interpolating polynomials, which are given by the following formula

$$\ell_i(x) = \prod_{j=0, j\neq i}^{N} \frac{x - x_j}{x_i - x_j}$$

The x derivative of $U_N(x,t)$ at any of the Chebyshev nodes may be computed explicitly as follows

$$\partial_x U_N(x_i,t) = \sum_{j=0}^{N} u_j(t)\ell_j'(x_i)$$

The above may be written compactly in terms of a matrix vector product:

$$\partial_x \vec{u_N} = D_N \vec{u_N}$$

where $\vec{u_N}_i = u_i(t)$ and D is the Chebyshev differentiation matrix whose entries are $(D_N)_{ij} = \ell_j'(x_i)$. Formulas for the entries of D_N are given in [89]. Although the above spectral differentiation procedure can be implemented via fast transform methods for $\mathcal{O}(N\log(N))$ floating point operations [89], we perform this step by direct matrix multiplication. The difference in computational cost is insignificant in our simulations since the high accuracy of the Chebyshev collocation method allows us to use a small number of nodes (in all simulations in this work, N is no more than 10).

Requiring that U_N satisfy the advection equation exactly at the Chebyshev nodes gives the following system of $N+1$ ordinary differential equations

$$\begin{aligned} \partial_t \vec{u_N} + D_N \vec{u_N} &= 0, && t > 0 \\ \vec{u}_i(0) &= f(x_i), && i = 1, ..., N \\ \vec{u}_0(t) &= g(t), && t > 0 \end{aligned}$$

the above system may then be solved by a variety of methods for ordinary differential equations, but care must be taken to ensure that the eigenvalues of D_N lie within the region of absolute stability of the chosen time integration method to ensure stability.

We obtain the semidiscrete Chebyshev collocation system corresponding to the blood flow equations (1.4) and (1.5) through the approach outlined above. Without incorporating boundary conditions, this semidiscretized system is

$$\partial_t \vec{A}_N = -D_N \vec{Q}_N \tag{A.1}$$

$$\partial_t \vec{Q}_N = -\frac{\gamma+2}{\gamma+1} D_N \left[(\vec{Q}_N .* \vec{Q}_N) ./ \vec{A}_N \right] - \frac{1}{\rho} \vec{A}_N .* D_N P(\vec{A}_N) - 2\pi(\gamma+2)\frac{\mu}{\rho} \left(\vec{Q}_N ./ \vec{A}_N \right) \tag{A.2}$$

$\vec{A}_N = [A_0(t), ..., A_N(t)]^T$ and $\vec{Q}_N = [Q_0(t), ..., Q_N(t)]^T$, where $Q_i(t) \approx Q(t, x_i)$ and $A_i(t) \approx A(t, x_i)$. In the above semidiscrete system, $\vec{x}.*\vec{y}$ and $\vec{x}./\vec{y}$ denote component-wise multiplication and division of vectors. $P(\vec{A}_N)$ is evaluated in a component-wise sense as well.

A.0.2 Time Discretization

To solve the semidiscrete system (A.1) and (A.2), we use the backward Euler method. Specifically, for the system $y = f(t, y)$, the backward Euler approximation of $y(t_{n+1})$, denoted y_{n+1}, satisfies the following system of equations [34]:

$$y_{n+1} = y_n + \Delta t f(t_{n+1}, y_{n+1})$$

where Δt is the time step size and $t_n = n\Delta t$. The backward Euler method is termed an implicit method because in order to determine y_{n+1}, one must solve the above system of equations, rather than evaluate an explicit formula of y_n and t_n. Let $\vec{A}_N^n$ and $\vec{Q}_N^n$ denote approximations to $\vec{A}_N(n\Delta t)$ and $\vec{Q}_N(n\Delta t)$, respectively. The backward Euler system for $\vec{A}_N^{n+1}$ and $\vec{Q}_N^{n+1}$ is

$$\left[\frac{\vec{A}_N^{n+1}}{\vec{Q}_N^{n+1}} \right] = \left[\frac{\vec{A}_N^{n}}{\vec{Q}_N^{n}} \right] + \Delta t F \left(\left[\frac{\vec{A}_N^{n+1}}{\vec{Q}_N^{n+1}} \right] \right) \tag{A.3}$$

where F denotes the right hand side of (A.1), (A.2). This system still requires modification to account for boundary conditions. We describe how we take boundary conditions into account in Appendix A.0.3. This resulting system is then solved with Newton's method with a direct linear solve. The Jacobian is computed analytically, and Newton iteration is performed until the ∞-norm of the residual is less than 10^{-7}.

Although the backward Euler method is only first order, it has excellent stability properties and, for this problem, it gives reasonably accurate results without requiring an excessively small time step size. More specific error information, along with the results of a numerical convergence study, are given in Appendix A.0.6. The implicit nature of backward Euler is not a computational hindrance due to the fact that the computational cost of the Jacobian is minimal since we have determined this Jacobian analytically. Furthermore, with backward Euler we are able to enforce the boundary conditions without the use of more sophisticated techniques such as penalty methods, which are often required to ensure stability for hyperbolic problems [39].

A.0.3 Numerical Implementation of Boundary Conditions

In each vessel, one boundary condition is imposed at the beginning of that vessel ($x = 0$) and one condition is imposed at the end. The particular form of the condition depends on a vessel's location within the arterial network (see Section 2). All types of boundary conditions are enforced numerically by replacing 2 of the equations in the backward Euler system (A.3) with boundary condition equations. This system is then solved by Newton's method with a direct linear solve with an analytically computed Jacobian.

The equations corresponding to the velocity inflow condition, the junction conditions, and the pure resistor outflow condition are trivial to implement since these are merely algebraic relations between the state variables. The implementation of the Windkessel requires a time discretization of the time derivatives of the states. We enforce the following discrete condition:

$$CR_1R_2\frac{Q_N^{n+1}-Q_N^n}{\Delta t}+(R_1+R_2)Q_N^{n+1}=CR_2\frac{P\left(A_N^{n+1}\right)-P\left(A_N^n\right)}{\Delta t}+P\left(A_N^{n+1}\right).$$

The implementation of the structured tree condition is considerably more complicated since it is not formulated in the time domain. For the periodic structured tree described in Chapter 3, we impose the following at each outflow boundary when computing the numerical solution at time t_{n+1}:

$$P(A_N^{n+1}) = \Delta t \sum_{k=0}^{N_T-1} Z^{(k)} Q_N^{n+1-k} \tag{A.4}$$

N_T is the number of time steps per period. N is the number of spatial points in the vessel. The values of $Z^{(k)}$ are computed by an inverse discrete Fourier transform of values of $\hat{Z}_k$. The values of $\hat{Z}_k$ are computed as described in Algorithm 1. This procedure is performed for each of the outflow vessels in the network being modeled. For additional details, consult Section 3.1.3. We note that although the parameters $\alpha, \beta, \lambda, r_{min}, \mu, \rho, \gamma, C$ are required for the functions IMPEDANCEPERIODIC and IMPEDANCEWEIGHTSPERIODIC, they are not explicitly listed as such to simplify the pseudocode. Condition (A.4) requires one to store the most recent $N_T - 1$ values of Q at each boundary. One must thus specify an initial history of $Q_N^{-N_T+2}, ..., Q_N^{-1}$ at each outflow boundary. As discussed in Section 3.2.2, this choice is largely irrelevant for one-dimensional simulations and these flowrate history values may merely be set to 0.

The value of $\hat{Z}_k$ in a particular vessel is determined uniquely by the radius of that vessel due to the tree structure described in Section 3.1.1. In the ith generation of a tree, there are only $i+1$ possible vessel radii: $r_{root}\alpha^{i+1}, r_{root}\alpha^{i}\beta, ..., r_{root}\beta^{i+1}$. Therefore, even though in a tree with N generations there are 2^N actual vessels, there are only $\mathcal{O}(N^2)$ different vessel radii values. Algorithm 1 takes advantage of this fact to ensure that the impedance is computed with $\mathcal{O}(N^2)$ work, which is achieved at a modest storage cost. The generalized structured tree condition derived in Chapter 4 is free from the periodicity assumption used in the original structured tree. The discretized generalized structured tree condition is:

$$P(A_N^{n+1}) = \sum_{j=0}^{n+1} z^{(j)} Q_N^{n+1-j} \tag{A.5}$$

When computing the numerical solution at time t_{n+1}, the values of Q_N^{n+1-j} are known for $j \geq 1$, meaning (A.5) forms a nonlinear scalar equation relating A_N^{n+1} and Q_N^{n+1}. The values of z_j are computed prior to running the simulation through a convolution quadrature algorithm. The algorithm used for this preprocessing step is described in Algorithm 2. For additional details on the generalized structured tree condition, see Chapter 4. For additional details on the convolution quadrature method, see Section 4.2.1 and [48, 49, 50].

Algorithm 1 Method to compute $Z^{(k)}$ in A.4

```
Input: $r_{root}, \Delta t, \alpha, \beta, \lambda, r_{min}, \mu, \rho, \gamma, C$.
  function IMPEDANCEWEIGHTSPERIODIC($r_{root}, \Delta t$)
    return $N_T \leftarrow T/\Delta t$                    ▷ $\Delta t$ is chosen so that $N$ is an integer
    for $k = 0 : (N_T - 1)/2$ do
      $\omega_k \leftarrow 2\pi k/T$
      maxGens ← CEIL($\log(r_{min}/r_{root})/\log(\alpha)$) +1
      table ← maxGens × maxGens matrix of NaN's
      $\hat{Z}_k$ ←IMPEDANCEPERIODIC($\omega_k, r_{root}$, 1, 1,table)
      $\hat{Z}_{-k} \leftarrow (\hat{Z}_k)^*$
    end for
    $Z \leftarrow$ IFFT($\hat{Z}$)                    ▷ $\hat{Z}$ is a vector with entries $\hat{Z}_k$
    return $Z$
  end function

  function IMPEDANCEPERIODIC($\omega_k, r_{root}, N_\alpha, N_\beta$,table)
    $r \leftarrow r_{root}\alpha^{N_\alpha - 1}\beta^{N_\beta - 1}$
    if $r < r_{min}$ then
      $ZL \leftarrow Z_{term}$
    else
      if table($N_\alpha + 1, N_\beta$) is NaN then
        [$ZD1$,table] ← IMPEDANCEPERIODIC($\omega_k, r_{root}, N_\alpha + 1, N_\beta$,table)
      else
        $ZD1 \leftarrow$ table($N_\alpha + 1, N_\beta$)
      end if

      if table($N_\alpha, N_\beta + 1$) is NaN then
        [$ZD2$,table] ← IMPEDANCEPERIODIC($\omega_k, r_{root}, N_\alpha, N_\beta + 1$,table)
      else
        $ZD2 \leftarrow$ table($N_\alpha, N_\beta + 1$)
      end if
      $ZL \leftarrow ZD1 \cdot ZD1/(ZD1 + ZD2)$                    ▷ Junction condition (3.8)
    end if

    if $\omega_k = 0$ then
      $Z0 \leftarrow ZL + \frac{2(\gamma+2)\mu\lambda}{\pi r^3}$                    ▷ See (3.17)
    else
      $Z0 \leftarrow \frac{ZL + i(d_k C)^{-1}\tan\left(\frac{\omega_k}{d_k}L\right)}{1 + i d_k C \tan\left(\frac{\omega_k}{d_k}L\right) ZL}$                    ▷ See (3.16)
    end if
    table($N_\alpha, N_\beta$) ← $Z0$
    return $Z0$,table
  end function
```

Algorithm 2 Algorithm to compute $z^{(j)}$ in (A.5)

```
Input:
        $t_f$ = final simulation time
        $\Delta t$ = time step size
        $\epsilon$ = accuracy of computation of $\hat{Z}$ in impedanceGen
        $r_{root}, \Delta t, \alpha, \beta, \lambda, r_{min}, \mu, \rho, \gamma, C$ = parameters determining the tree
function ImpedanceWeights($r_{root}, \Delta t$)
    $N_{t_f} \leftarrow t_f/\Delta t$                              ▷ $\Delta t$ is chosen so $N_{t_f}$ is an integer
    $M \leftarrow 2N_{t_f}$
    $r \leftarrow \epsilon^{1/(2N_{t_f})}$
    maxGens ← ceil($\log(r_{min}/r_{root})/\log(\alpha)$) +1
    table ← maxGens × maxGens matrix of NaN's
    for $m = 0 : M-1$ do
        $\zeta \leftarrow re^{i2\pi m/M}$
        $\Xi \leftarrow \frac{1}{2}\zeta^2 - 2\zeta + \frac{3}{2}$
        $\hat{Z}^{(m)} \leftarrow$ impedanceGen($\Xi/\Delta t, r_{root}$,1,1,table)
    end for

    for $n = 0 : N_{t_f}$ do
        $z_n \leftarrow \frac{r^{-n}}{M} \sum_{m=0}^{M-1} \hat{Z}^{(m)} e^{-i2\pi mn/M}$
    end for
    return $z$                                               ▷ $z$ is vector with entries $z_n$
end function

function impedanceGen($s, r_{root}, N_\alpha, N_\beta$,table)
    $r \leftarrow r_{root}\alpha^{N_\alpha - 1}\beta^{N_\beta - 1}$
    if $r < r_{min}$ then
        $ZL \leftarrow Z_{term}$
    else
        if table($N_\alpha + 1, N_\beta$) is NaN then
            [$ZD1$,table] ← impedanceGen($s, r_{root}, N_\alpha + 1, N_\beta$,table)
        else
            $ZD1 \leftarrow$ table($N_\alpha + 1, N_\beta$)
        end if
```

Algorithm 2 Algorithm to compute $z^{(j)}$ (continued)

```
        if table($N_\alpha, N_\beta + 1$) is NaN then
            [$ZD2$,table] ← IMPEDANCEGEN($s, r_{root}, N_\alpha, N_\beta + 1$,table)
        else
            $ZD2 \leftarrow$ table($N_\alpha, N_\beta + 1$)
        end if
        $ZL \leftarrow ZD1 \cdot ZD1/(ZD1 + ZD2)$                    ▷ Junction condition (4.6)
    end if

    if $s = 0$ then
        $Z0 \leftarrow ZL + \frac{2(\gamma+2)\mu\lambda}{\pi r^3}$                    ▷ See (4.5)
    else
        $Z0 \leftarrow \frac{\hat{Z}(L,s) + \frac{1}{sd_sC}\tanh L/d_s}{sd_sC\,\hat{Z}(L,s)\tanh L/d_s + 1}$                    ▷ See (4.4)
    end if
    table($N_\alpha, N_\beta$) ← $Z0$
    return $Z0$,table
end function
```

A.0.4 Network Descriptions

In this work, we treat individual arteries as 1D domains, and arterial networks are handled by connecting these 1D domains together. The one-dimensional modeling approach means that we only need to prescribe lengths (denoted L) and connectivity information to completely describe a model arterial network. We also need to prescribe values of the unstressed vessel radius, $r_0(x)$, for $x \in [0, L]$ for each vessel in the network, but $r_0(x)$ only enters the model as a parameter (see (1.3)).

To describe the Circle of Willis network, we use data collected by Dr. Vera Novak at Harvard Medical School via magnetic resonance imaging (MRI). Figure A.1 contains a schematic displaying the structure of the Circle of Willis, and Table A.1 contains specific vessel lengths and unstressed radii. For the Circle of Willis, we use a constant value of r_0 within each vessel.

In Chapter 5, we performed simulations of the full systemic arterial tree. Network geometry data for the arterial tree is from Olufsen [62, 63, 64]. A rough diagram of this network is displayed in Figure A.2 and specific radii and length values are given in Table A.2. In this table, r_t refers to the unstressed vessel radius at the inlet of the vessel ($x = 0$), and r_b is the unstressed radius at the outlet of the vessel ($x = L$). For $0 < x < L$, $r_0(x)$ is determined by

Table A.1: Names and measured length/radii data (in cm) for the Circle of Willis (Figure A.1). Data are from [26]. BA–Basilar Artery, PCA–Posterior Cerebral Artery, PCoA–Posterior Communicating Artery, ICA–Internal Carotid Artery, MCA–Middle Cerebral Artery, ACA–Anterior Cerebral Artery, AcoA–Anterior Communicating Artery. An * accompanying a data value indicates that this value was estimated rather than directly measured.

No.	Name	r_0	L
1	BA	0.15	0.825
2	R. PCA 1	0.112*	0.333*
3	L. PCA 1	0.112*	0.333*
4	R. PCA 2	0.110	0.756
5	L. PCA 2	0.110	0.756
6	R. PCoA	0.0986*	1.00
7	L. PCoA	0.0986*	1.00*
8	R. ICA	0.210	4.81
9	L. ICA	0.210	4.81
10	R. MCA	0.134	2.11
11	L. MCA	0.134	2.11
12	R. ACA 1	0.170	1.07
13	L. ACA 1	0.100	1.07
14	ACoA	0.100	0.20
15	R. ACA 2	0.115	2.30
16	L. ACA 2	0.115	2.30

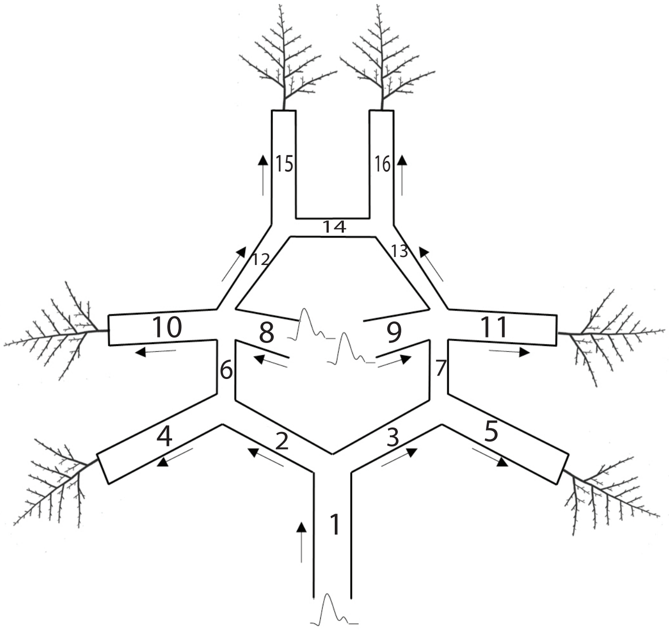

Figure A.1: Schematic of the Circle of Willis.

the formula $r_0 = r_t(r_b/r_t)^{x/L}$.

A.0.5 Parameter Values

The parameter values in Table A.3, from [64], are used for each simulation in this study. The only exception is the systemic arterial tree simulation in Chapter 5, where a radius dependent viscosity was used for the smaller arteries in the structured tree model.

A.0.6 Convergence Study

We now analyze the convergence of the discretization scheme for the system (1.4,1.5,). If the solutions are smooth, Chebyshev collocation methods typically converge rapidly [13, 39, 89]. In Figure A.3, we see precisely this behavior. Using 17 points per spatial vessel, the discretization error is only 10^{-12}. To compute an approximation of the discretization error, the solution for various values of N was compared to a numerical solution using $N = 33$. We used a fixed $\Delta t = 0.001$ for this spatial grid refinement study. The errors listed in Table A.4 and in displayed in Figure A.3 use the L_1-norm. Due to the rapid convergence with respect to N, we

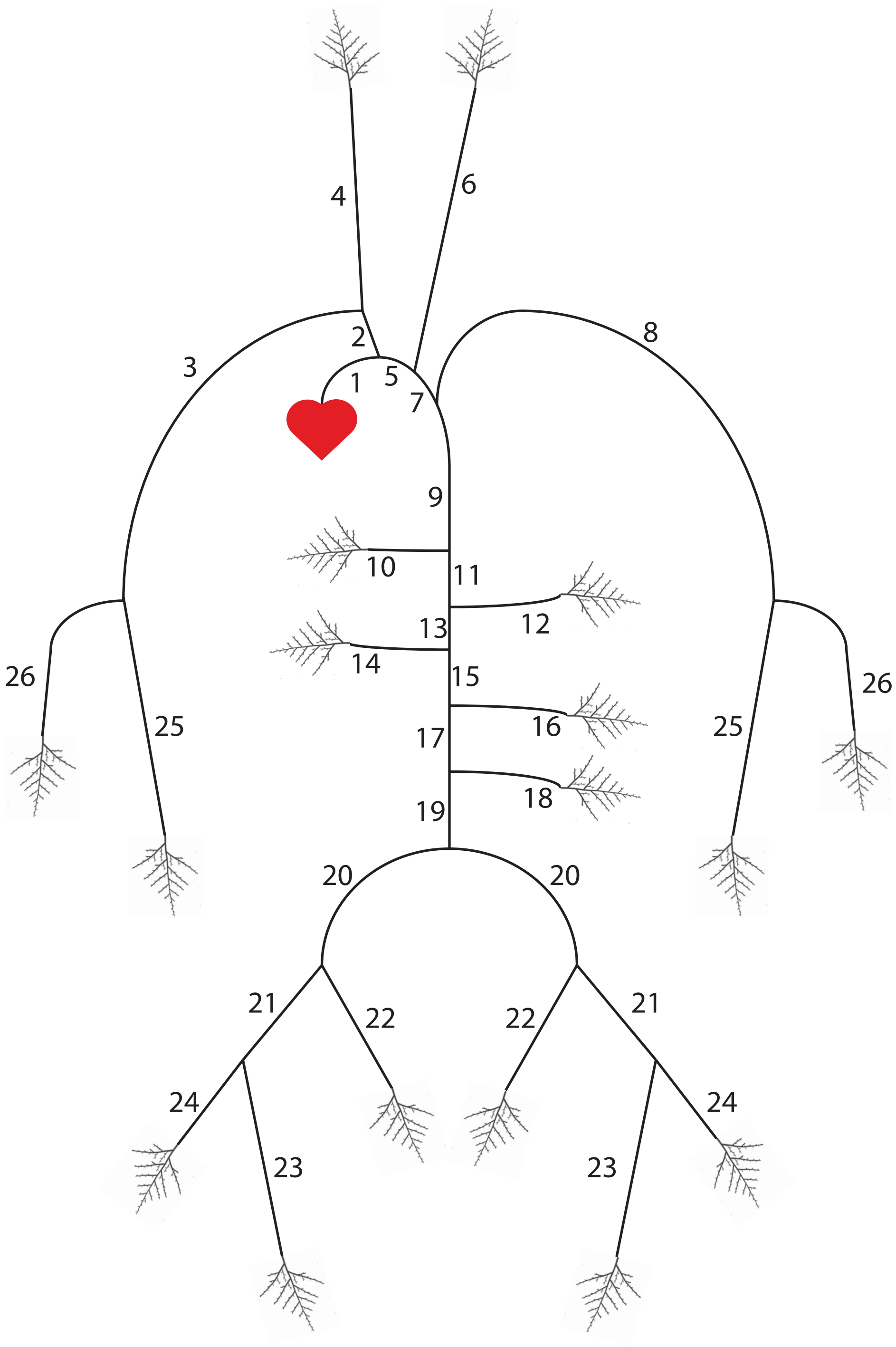
4
6
2
8
3
1
5
7
9
10
11
12
13
14
15
16
26
25
17
25
26
18
19
20
20
21
22
22
21
24
24
23
23

Figure A.2: Schematic of the systemic arterial tree network used in Chapter 5. The trees attached to each outlet vessel symbolizes the use of the structured tree to model the downstream domain.

Table A.2: Names and length/radii data for the systemic arterial tree network used in the simulations in Chapter 5. Data are from Olufsen [62, 64].

No.	Artery	L(cm)	r_t(cm)	r_b(cm)
1	Ascending Aorta	7.0	1.25	1.14
5	Aortic Arch	1.8	1.14	1.11
7	Aortic Arch	1.0	1.11	1.09
9	Thoracic Aorta	18.18	1.09	0.85
11	Abdominal Aorta	2.0	0.85	0.83
13	Abdominal Aorta	2.0	0.83	0.80
15	Abdominal Aorta	1.0	0.80	0.79
17	Abdominal Aorta	6.0	0.79	0.73
19	Abdominal Aorta	3.0	0.73	0.70
20	External Iliac	6.5	0.45	0.43
21	Femoral	13.0	0.43	0.40
24	Femoral	44.0	0.40	0.30
22	Internal Iliac	4.5	0.20	0.20
23	Deep Femoral	11.0	0.20	0.20
2	Anonyma	3.5	0.70	0.70
3, 8	Subcl. and Brach.	43.0	0.44	0.28
4	R. Com. Carotid	17.0	0.29	0.28
6	L. Com. Carotid	19.0	0.29	0.28
10	Celiac Axis	3.0	0.33	0.30
12	Sup. Mesenteric	5.0	0.33	0.33
14,16	Renal	3.0	0.28	0.25
18	Inf. Mesenteric	4.0	0.20	0.18
25	Radial	23.5	0.174	0.142
26	Ulner	6.7	0.215	0.215

Table A.3: Parameter values used for simulations in this dissertation

Parameter	**Value**	**Description**
ρ	1.06 g cm^{-3}	density of blood
γ	2	velocity profile parameter
μ	0.0488 $\text{cm}^{-1}\text{s}^{-1}$	viscosity of blood
C	$3\pi r^3/2Eh$	vessel compliance $\partial A/\partial P$
Eh/r	$k_1 e^{k_2 r} + k_3$	E = vessel wall elastic modulus, h = vessel wall thickness
k_1	$2.00 \times 10^7 \text{gs}^{-2}\text{cm}^{-1}$	
k_2	-22.53 cm^{-1}	
k_3	$8.65 \times 10^5 \text{gs}^{-2}\text{cm}^{-1}$	

Table A.4: Convergence of numerical solutions to the Circle of Willis with respect to the number of spatial points per vessel.

Windkessel		Structured Tree	
N	E	N	E
2	1.02e-06	2	9.52e-07
4	9.43e-08	4	9.39e-08
8	6.70e-11	8	6.63e-11
16	1.48e-12	16	1.41e-12

use $N = 8$ for all simulations of the Circle of Willis since this value appears to be more than sufficient to ensure reasonable accuracy.

We also investigate the convergence of this discretization scheme with respect to time step size, Δt. The numerical approximations converge with order 1 with respect to Δt, which is expected for backward Euler [34]. Based on the specific error values in Table A.5 and Table A.6, we use a value of $\Delta t = 0.025$ seconds since this appears to be sufficient to ensure 1% accuracy of the numerical solutions. To approximate the error of a particular numerical solution, we compare that solution with another numerical approximation computed with a value of Δt five times smaller than the smallest time step size in Table A.5 and Table A.6. All simulations in the temporal grid refinement used a fixed value of 9 spatial points per vessel.

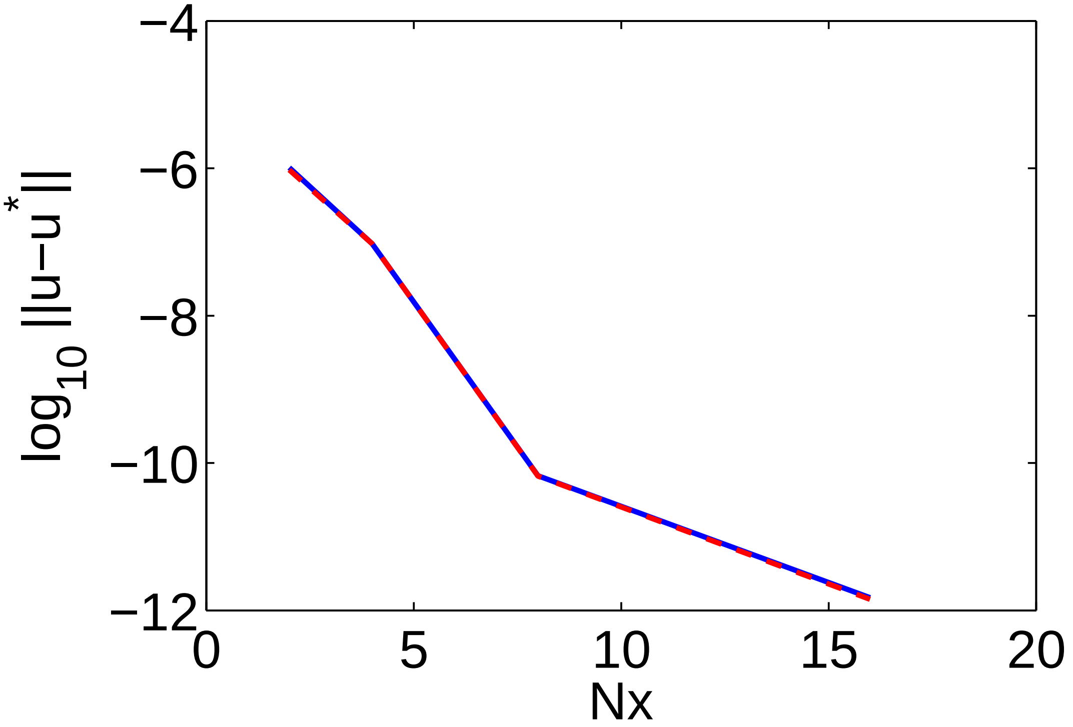

Figure A.3: Convergence of numerical simulations of the Circle of Willis with respect to the number of spatial points per vessel for a fixed time step size of $\Delta t = 0.001$. The blue curve was generated for the Windkessel boundary condition, and the red curve uses the periodic structured tree. In the vertical axis label, u^* denotes a numerical solution computed with 33 spatial points per vessel ($N = 32$).

Table A.5: Convergence of numerical solutions to the Circle of Willis with respect to time step size using the Windkessel boundary condition.

Δt	E	$E(2\Delta t)/E(\Delta t)$
0.100000	3.75e-02	NaN
0.050000	2.13e-02	1.760122
0.025000	1.13e-02	1.877645
0.012500	5.93e-03	1.912231
0.006250	2.95e-03	2.009360
0.003125	1.36e-03	2.164632

Table A.6: Convergence of numerical solutions to the Circle of Willis with respect to time step size using the structured tree boundary condition.

Δt	E	$E(2\Delta t)/E(\Delta t)$
0.100000	3.21e-02	NaN
0.050000	1.63e-02	1.967751
0.025000	8.74e-03	1.865431
0.012500	4.58e-03	1.909398
0.006250	2.29e-03	1.995762
0.003125	1.07e-03	2.137076

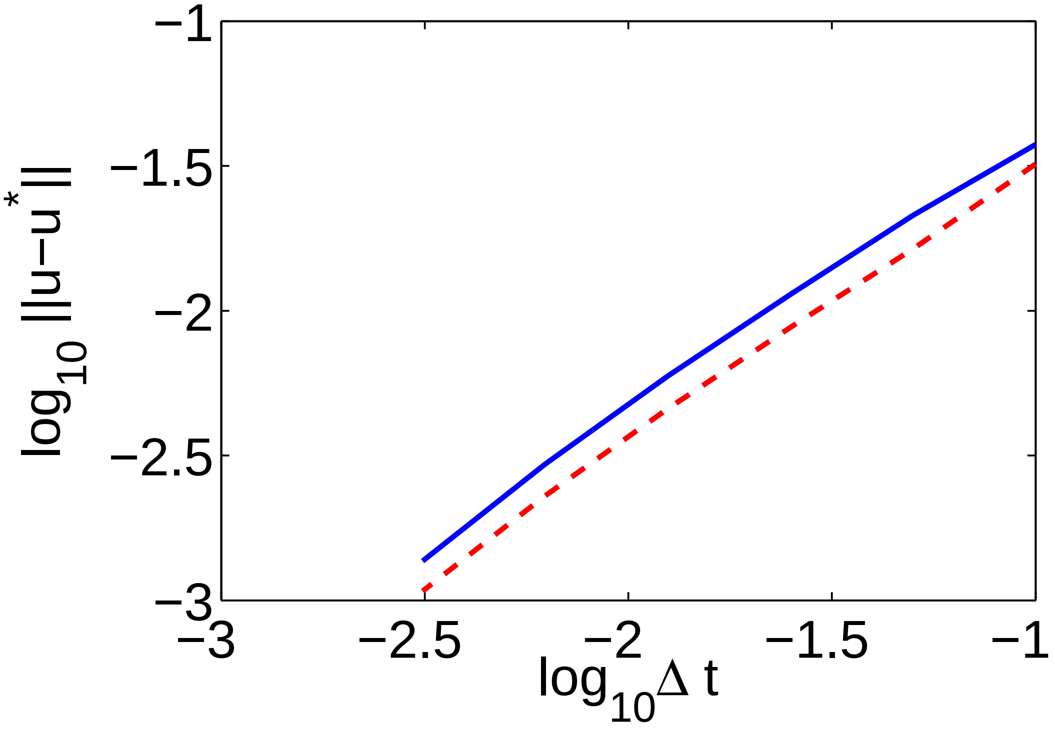

Figure A.4: Convergence of numerical simulations of the Circle of Willis with respect to Δt for a fixed number of spatial points per vessel ($N = 8$). The blue curve was generated using the Windkessel boundary condition, and the red curve uses the periodic structured tree. In the vertical axis label, u^* denotes a numerical solution computed with a value of Δt five times smaller than the smallest value of Δt listed in Table A.5.